

# Nanomaterials for Medical and Dental Applications

Guest Editors: Tae-Yub Kwon, Daniel S. Oh, and Ramaswamy Narayanan



---



# **Nanomaterials for Medical and Dental Applications**

Journal of Nanomaterials

---

## **Nanomaterials for Medical and Dental Applications**

Guest Editors: Tae-Yub Kwon, Daniel S. Oh,  
and Ramaswamy Narayanan



---

Copyright © 2015 Hindawi Publishing Corporation. All rights reserved.

This is a special issue published in "Journal of Nanomaterials." All articles are open access articles distributed under the Creative Commons Attribution License, which permits unrestricted use, distribution, and reproduction in any medium, provided the original work is properly cited.

## Editorial Board

Domenico Acierno, Italy	Jeffrey Elam, USA	Wei Lin, USA
Katerina Aifantis, USA	Samy El-Shall, USA	N. C. Lindquist, USA
Nageh K. Allam, USA	Ovidiu Ersen, France	Jun Liu, USA
Margarida Amaral, Portugal	Claude Estournès, France	Zainovia Lockman, Malaysia
Martin Andersson, Sweden	Andrea Falqui, KSA	Nico Lovergine, Italy
Raul Arenal, Spain	Matteo Ferroni, Italy	Jim Low, Australia
Ilaria Armentano, Italy	Elena J. Foster, USA	Jue Lu, USA
Vincenzo Baglio, Italy	Ilaria Fratoddi, Italy	Songwei Lu, USA
Lavinia Balan, France	Alan Fuchs, USA	Ed Ma, USA
Thierry Baron, France	Miguel A. Garcia, Spain	Laura M. Maestro, Spain
Andrew R. Barron, USA	Siddhartha Ghosh, Singapore	Gaurav Mago, USA
Reza Bayati, USA	P. K. Giri, India	Muhamamd A. Malik, UK
Hongbin Bei, USA	Russell E. Gorga, USA	Devanesan Mangalaraj, India
Daniel Bellet, France	Jihua Gou, USA	Sanjay R. Mathur, Germany
Stefano Bellucci, Italy	Jean M. Greeneche, France	Tony McNally, UK
Enrico Bergamaschi, Italy	Smrati Gupta, Germany	Yogendra Mishra, Germany
Samuel Bernard, France	K. Hamad-Schifferli, USA	Paulo Cesar Morais, Brazil
D. Bhattacharyya, New Zealand	Simo-Pekka Hannula, Finland	Paul Munroe, Australia
Sergio Bietti, Italy	Michael Harris, USA	Jae-Min Myoung, Republic of Korea
Giovanni Bongiovanni, Italy	Yasuhiko Hayashi, Japan	Rajesh R. Naik, USA
T. Borca-Tasciuc, USA	F. Hernandez-Ramirez, Spain	Albert Nasibulin, Russia
Mohamed Bououdina, Bahrain	Michael Z. Hu, USA	Toshiaki Natsuki, Japan
Torsten Brezesinski, Germany	Nay Ming Huang, Malaysia	Koichi Niihara, Japan
C. Jeffrey Brinker, USA	Shaoming Huang, China	Natalia Noginova, USA
Christian Brosseau, France	David Hui, USA	Sherine Obare, USA
Philippe Caroff, Australia	Zafar Iqbal, USA	Won-Chun Oh, Republic of Korea
V. M. Castaño, Mexico	B. Jeyadevan, Japan	Atsuto Okamoto, Japan
Albano Cavaleiro, Portugal	Xin Jiang, Germany	Abdelwahab Omri, Canada
Bhanu P. S. Chauhan, USA	Rakesh Joshi, Australia	Ungyu Paik, Republic of Korea
Shafiu Chowdhury, USA	Jeong-won Kang, Republic of Korea	Piersandro Pallavicini, Italy
Jin-Ho Choy, Republic of Korea	Hassan Karimi-Maleh, Iran	Edward A. Payzant, USA
Kwang-Leong Choy, UK	Antonios Kelarakis, UK	Alessandro Pegoretti, Italy
Yu-Lun Chueh, Taiwan	Alireza Khataee, Iran	Ton Peijs, UK
Elisabetta Comini, Italy	Ali Khorsand Zak, Iran	O. Perales-Pérez, Puerto Rico
Giuseppe Compagnini, Italy	Philippe Knauth, France	Jorge Pérez-Juste, Spain
David Cornu, France	Ralph Krupke, Germany	Alexey P. Popov, Finland
M. A. Correa-Duarte, Spain	Christian Kübel, Germany	Philip D. Rack, USA
Pantaleo D. Cozzoli, Italy	Prashant Kumar, UK	Peter Reiss, France
Shadi A. Dayeh, USA	Michele Laus, Italy	Orlando Rojas, USA
Luca Deseri, USA	Eric Le Bourhis, France	Marco Rossi, Italy
Yong Ding, USA	Burtrand Lee, USA	Ilker S. Bayer, Italy
Philippe Dubois, Belgium	Jun Li, Singapore	Cengiz S. Ozkan, USA
Zehra Durmus, Turkey	Meiyong Liao, Japan	Sudipta Seal, USA
Joydeep Dutta, Oman	Shijun Liao, China	Shu Seki, Japan
Ali Eftekhari, USA	Silvia Licoccia, Italy	V. Šepelák, Germany

Huaiyu Shao, Japan	Leander Tapfer, Italy	Ruibing Wang, Macau
Prashant Sharma, USA	Valeri P. Tolstoy, Russia	Shiren Wang, USA
Donglu Shi, USA	Muhammet S. Toprak, Sweden	Yong Wang, USA
Bhanu P. Singh, India	Ramon Torrecillas, Spain	Magnus Willander, Sweden
Surinder Singh, USA	Achim Trampert, Germany	Ping Xiao, UK
Vladimir Sivakov, Germany	Takuya Tsuzuki, Australia	Zhi Li Xiao, USA
Ashok Sood, USA	Tamer Uyar, Turkey	Yangchuan Xing, USA
Adolfo Speghini, Italy	Bala Vaidhyanathan, UK	Doron Yadlovker, Israel
Marinella Striccoli, Italy	Luca Valentini, Italy	Yoke K. Yap, USA
Xuping Sun, KSA	Rajender S. Varma, USA	Kui Yu, Canada
A. K. Sundramoorthy, USA	Ester Vazquez, Spain	William Yu, USA
Angelo Taglietti, Italy	Antonio Villaverde, Spain	Michele Zappalorto, Italy
Bo Tan, Canada	Ajayan Vinu, Australia	Renyun Zhang, Sweden

## Contents

**Nanomaterials for Medical and Dental Applications**, Tae-Yub Kwon, Daniel S. Oh, and Ramaswamy Narayanan  
Volume 2015, Article ID 707683, 2 pages

**Evaluation of Synthesized Nanohydroxyapatite-Nanocellulose Composites as Biocompatible Scaffolds for Applications in Bone Tissue Engineering**, Claudia S. Herdicia-Lluberes, Simara Laboy-López, Stefannie Morales, Tania J. Gonzalez-Robles, José A. González-Feliciano, and Eduardo Nicolau  
Volume 2015, Article ID 310935, 9 pages

**Comparison of Fibroblast and Osteoblast Response to Cultivation on Titanium Implants with Different Grain Sizes**, Vaclav Babuska, Jana Dobra, Vlastimil Kulda, Michaela Kripnerova, Amin Moztarzadeh, Lukas Bolek, Jiri Lahoda, and Daniel Hrusak  
Volume 2015, Article ID 920893, 9 pages

**3D Nanoprinting Technologies for Tissue Engineering Applications**, Jin Woo Lee  
Volume 2015, Article ID 213521, 14 pages

**Enhanced Hydrophilicity and Protein Adsorption of Titanium Surface by Sodium Bicarbonate Solution**, Shengnan Jia, Yu Zhang, Ting Ma, Haifeng Chen, and Ye Lin  
Volume 2015, Article ID 536801, 12 pages

**UV Photocatalysis of Bone Marrow-Derived Macrophages on TiO<sub>2</sub> Nanotubes Mediates Intracellular Ca<sup>2+</sup> Influx via Voltage-Gated Ca<sup>2+</sup> Channels**, Seunghan Oh, Eun-Joo Choi, Munkhsoyol Erkhembaatar, and Min Seuk Kim  
Volume 2015, Article ID 583456, 7 pages

**Contact with Fluoride-Releasing Restorative Materials Can Arrest Simulated Approximal Caries Lesion**, Camila de Almeida Brandão Guglielmi, Ana Flávia Bissoto Calvo, Tamara Kerber Tedesco, Fausto Medeiros Mendes, and Daniela Prócida Raggio  
Volume 2015, Article ID 259753, 7 pages

**A Novel Approach of Targeted Immunotherapy against Adenocarcinoma Cells with Nanoparticles Modified by CD16 and MUC1 Aptamers**, Lianyuan Yu, Yan Hu, Jinhong Duan, and Xian-Da Yang  
Volume 2015, Article ID 316968, 10 pages

## Editorial

# Nanomaterials for Medical and Dental Applications

Tae-Yub Kwon,<sup>1</sup> Daniel S. Oh,<sup>2</sup> and Ramaswamy Narayanan<sup>3</sup>

<sup>1</sup>Department of Dental Biomaterials, School of Dentistry, Kyungpook National University, Daegu 41940, Republic of Korea

<sup>2</sup>College of Dental Medicine, Columbia University, New York, NY 10032, USA

<sup>3</sup>School of Mechanical and Building Sciences (SMBS), VIT University, Tamil Nadu 600 127, India

Correspondence should be addressed to Tae-Yub Kwon; [tykwon@knu.ac.kr](mailto:tykwon@knu.ac.kr)

Received 12 December 2015; Accepted 13 December 2015

Copyright © 2015 Tae-Yub Kwon et al. This is an open access article distributed under the Creative Commons Attribution License, which permits unrestricted use, distribution, and reproduction in any medium, provided the original work is properly cited.

Welcome to this special issue. Nanoscience and nanotechnology concepts are applicable across all fields of science and a more widespread application of nanomaterials and nanotechnologies is imminent or already occurring in many areas, including health care. Today's scientists take those cutting-edge technologies and concepts and apply them to medicine and dentistry. They are finding a wide variety of ways to make medical and dental materials at the nanoscale to take advantage of their enhanced physical and biological properties.

The purpose of this special issue is to publish high-quality research papers as well as review articles addressing recent advances in the field of nanomaterials for medical and dental applications. A particular interest is given to papers exploring or discussing nanomaterials and nanotechnologies related to delivery system, bonding substitutes, and surface modification techniques applicable in these areas. For this special issue, several investigators were invited to contribute original research findings that can stimulate continuing efforts to understand the cutting-edge applications of nanomaterials in medicine and dentistry.

The physiological interaction between the titanium (Ti) surface and bone cells, especially osteoclasts, is a crucial factor in determining successful osseointegration. However, the details of such an interaction remain elusive. S. Oh et al. demonstrated that nanotopography on the Ti surface is a crucial factor for modulating intracellular signal transduction in bone marrow-derived macrophages (BMMs). In their study, UV photocatalysis of  $\text{TiO}_2$  immediately elicited  $[\text{Ca}^{2+}]_i$  increase and  $[\text{ROS}]_i$  reduction in cells growing on  $\text{TiO}_2$  nanotubes. UV photocatalysis-mediated  $[\text{Ca}^{2+}]_i$  increase was

dependent on extracellular and intracellular ROS generation. Furthermore, extracellular  $\text{Ca}^{2+}$  influx through VGCCs was critical for UV photocatalysis-mediated  $[\text{Ca}^{2+}]_i$  increase, while PLC activation was not. They concluded that nanotopography on the Ti surface should be considered an important factor that can influence successful dental implantation.

Mucin1 (MUC1) is a potentially important target of cancer therapy, being a glycoprotein that is overexpressed on cell surface of many types of adenocarcinomas. Several MUC1-targeted drug delivery systems have been developed and reported, but mobilizing natural killer cells (NK) to fight against MUC1-positive tumor has not been attempted. L. Yu et al. introduced a novel amphipathic nanoparticle for enhancing the NK cytotoxicity to MUC1-positive cancer cells. In their study, a novel amphipathic nanoparticle was constructed by implanting CD16 and MUC1 aptamers onto its surface. This nanoparticle pulled NK (or other CD16-positive immune cells) and MUC1-positive cancer cells together *in vitro* and significantly enhanced the NK cytotoxicity to MUC1-positive cancer cells. The authors suggested that NK cells might be mobilized to target against MUC1-positive tumor cells.

It has been suggested that the presence of white-spot lesion is very probable when adjacent surface is affected by cavitated lesions. C. A. B. Guglielmi et al. evaluated the potential of different fluoride-releasing restorative materials in arresting enamel white-spot lesions in approximal contact with them, *in vitro* (I) and *in situ* (II). White-spot lesions were formed in 120 primary enamel specimens via pH-cycling and put in contact with cylindrical blocks of six different dental restorative materials. At the end of both studies, specimens

were collected for mineral analysis by cross-sectional micro-hardness. High-viscous glass ionomer cements (HVGICs) were the most efficient in preventing mineral loss, whereas other materials presented an intermediate behavior. The authors concluded that fluoride-releasing materials can moderately reduce white-spot lesions progression, and HVGIC can arrest enamel lesion when in approximal contact.

Conventional scaffold fabrication methods do not control the architecture, pore shape, porosity, or interconnectivity of the scaffold, so it has limited ability to stimulate cell growth and to generate new tissue. In the review article, J. W. Lee suggests that three-dimensional (3D) printing technologies may overcome these disadvantages of traditional fabrication methods. These technologies use computers to assist in design and fabrication, so the 3D scaffolds can be fabricated as designed and standardized. Recent combinations of 3D nanoprinting technologies with methods from molecular biology and cell dynamics have suggested new possibilities for improved tissue regeneration. The author speculated that 3D nanoprinting will become an important tool in tissue engineering in the near future.

S. Jia et al. evaluated a novel, simple, and convenient method to enhance hydrophilicity of Ti surfaces with sodium bicarbonate ( $\text{NaHCO}_3$ ) solution. Sand-blasted and acid-etched (SLA) Ti surfaces and machined Ti surfaces were treated with  $\text{NaHCO}_3$  solution. In their study, super-hydrophilic SLA Ti surfaces were obtained by reversible deprotonation and ion exchange processes. Increased protein adsorption on  $\text{NaHCO}_3$ -treated specimens was also observed. They concluded that this  $\text{NaHCO}_3$  treatment is a reliable method for enhancing the hydrophilicity and protein adsorption of SLA Ti surfaces.

V. Babuska et al. compared the *in vitro* response of human fibroblast cell line HFL1 and human osteoblast cell line hFOB 1.19 on nanostructured Ti with different grain size. In their study, similar cellular behavior was observed on all studied biomaterials. There were significant differences related to the initial phase of attachment, but not in proliferation. Furthermore, the results indicate that osteoblasts grow the best on material with grain size of 160 nm with a longitudinal section in comparison with other examined materials. The authors concluded that this material could be recommended for further evaluation with respect to osseointegration *in vivo*.

Basic calcium phosphate (BCP) crystals have been associated with many diseases due to their activation of signaling pathways that lead to their mineralization and deposition in intra-articular and periarticular locations in the bones. In the study by C. Herdicia-Lluberes et al., hydroxyapatite (HAp) was placed in a polysaccharide network as a strategy to minimize the BCP cell activation. Their research consisted of the evaluation of varying proportions of the polysaccharide network, cellulose nanocrystals (CNCs), and HAp synthesized via a simple sol gel method. After preparation of the biocompatible composite, the products were characterized by various analytical methods. It was found that a  $n\text{HAp} = \text{CNC}$  ratio presented greater homogeneity in the size and distribution of the nanoparticles without compromising the crystalline structure. The osteoblast cell viability assay also demonstrated that all of the composites promoted greater cell

proliferation. The authors suggested that the  $n\text{HAp} > \text{CNC}$  proportion with the inclusion of the bone morphogenetic protein 2 (BMP-2) protein was the best composite.

Tae-Yub Kwon

Daniel S. Oh

Ramaswamy Narayanan

## Research Article

# Evaluation of Synthesized Nanohydroxyapatite-Nanocellulose Composites as Biocompatible Scaffolds for Applications in Bone Tissue Engineering

Claudia S. Herdicia-Lluberes,<sup>1,2</sup> Simara Laboy-López,<sup>2,3</sup> Stefannie Morales,<sup>2</sup> Tania J. Gonzalez-Robles,<sup>2,3</sup> José A. González-Feliciano,<sup>2</sup> and Eduardo Nicolau<sup>2,3</sup>

<sup>1</sup>Department of Biology, University of Puerto Rico, Rio Piedras Campus, P.O. Box 23346, San Juan, PR 00931-3346, USA

<sup>2</sup>Molecular Science Research Center, University of Puerto Rico, Suite 2, 1390 Ponce De Leon Avenue, San Juan, PR 00931-3346, USA

<sup>3</sup>Department of Chemistry, University of Puerto Rico, Rio Piedras Campus, P.O. Box 23346, San Juan, PR 00931-3346, USA

Correspondence should be addressed to Eduardo Nicolau; [eduardo.nicolau@upr.edu](mailto:eduardo.nicolau@upr.edu)

Received 26 September 2015; Accepted 30 November 2015

Academic Editor: Tae-Yub Kwon

Copyright © 2015 Claudia S. Herdicia-Lluberes et al. This is an open access article distributed under the Creative Commons Attribution License, which permits unrestricted use, distribution, and reproduction in any medium, provided the original work is properly cited.

Basic calcium phosphate (BCP) crystals have been associated with many diseases due to their activation of signaling pathways that lead to their mineralization and deposition in intra-articular and periarticular locations in the bones. In this study, hydroxyapatite (HAp) has been placed in a polysaccharide network as a strategy to minimize this deposition. This research consisted of the evaluation of varying proportions of the polysaccharide network, cellulose nanocrystals (CNCs), and HAp synthesized via a simple sol-gel method. The resulting biocompatible composites were extensively characterized by means of thermogravimetric analysis (TGA), powder X-ray diffraction (XRD), Fourier transform infrared spectroscopy (FT-IR), dynamic light scattering (DLS), zeta potential, and scanning electron microscopy (SEM). It was found that an nHAp = CNC ratio presented greater homogeneity in the size and distribution of the nanoparticles without compromising the crystalline structure. Also, incorporation of bone morphogenetic protein 2 (BMP-2) was performed to evaluate the effects that this interaction would have in the constructs. Finally, the osteoblast cell (hFOB 1.19) viability assay was executed and it showed that all of the materials promoted greater cell proliferation while the nHAp > CNC proportion with the inclusion of the BMP-2 protein was the best composite for the purpose of this study.

## 1. Introduction

Advances in Bone Tissue Engineering (BTE) hold promise for the development of new functional coatings for bone regeneration. The integration of novel bionanomaterials that induce bone regeneration can contribute to the field of BTE and help settle the incidence of bone disorders and conditions [1, 2]. BTE has been a field of study of increasing interest over the past few decades and it focuses on alternative treatment options that will ideally eliminate issues of current clinically used treatments with bone implants, such as donor site morbidity, immune rejection, and pathogen transfer. The main goal of this field is to create bone grafts that enhance bone repair and regeneration of damaged tissue, combining

body cells with highly porous scaffold bionanomaterials [2]. Scaffolds are structures that bring support to the bone by promoting biocompatibility that enriches with nutrients the existing natural bone; therefore, it must imitate its composition in the best way possible. Scaffolds must be stress-shielding, biocompatible, and porous structures that resemble the bone [3, 4]. The most studied material to replace and regenerate human hard tissue is hydroxyapatite (HAp), an interesting biomaterial with potential to improve the field of medicine and dentistry. Hydroxyapatite ( $\text{Ca}_{10}(\text{PO}_4)_6(\text{OH})_2$ , HAp) is chemically and structurally similar to the inorganic components of bone, enamel, and dentin; it is also bioactive and supports bone ingrowth and osseointegration. Due to these unique features HAp has gained recognition and

importance in the field of BTE. It has also been successfully used as bone filler, aesthetic restorative, coating of orthopedic implants, filler of inorganic/polymer composites, and cell-culture carrier, among others [5].

Overall, the use of basic calcium phosphate (BCP) crystals, such as HAp, has been associated with many diseases due to their deposition in intra-articular and periarticular locations site [6]. New pathogenic mechanisms for the deposition mechanisms of BCPs suggest that the extracellular inorganic phosphate, inorganic pyrophosphate, and  $\text{Ca}^{2+}$  concentrations are critical determinants of mineralization [7, 8]. It has been found that BCP crystals activate three major signaling pathways: crystal endocytosis and intracellular crystal dissolution with subsequent intracellular calcium increase [9]. Therefore, placing the HAp in a polysaccharide network might prevent this cell activation. Additionally, the use of HAp as a coating agent for metallic implants has been discouraged by many scientists because it is limited to non-load-bearing applications due to the disproportion between the different Young modulus of each. This is an undesired effect because it leads to bone density loss and even fracture or disconnection of bone from the implant. It is of our interest that the polysaccharide network could serve as a hardening intermediate between the bone and the implant [10].

There are many polysaccharides that have been used for tissue engineering applications such as chitosan and gelatin [11, 12]. A similar material, cellulose nanocrystals (CNCs), has been the subject of study in several applications because it is one of the most abundant biopolymers on earth; it is nontoxic and has a Young modulus of 167.5 GPa comparable to the stiffness of titanium, copper, and bronze materials used in bone implants [13]. CNCs are the ordered crystalline regions of cellulose microfibers (cellulose molecule chains connected through hydrogen bonding with approximately 5–50 nm in diameter) which can be obtained from hydrolysis [14, 15].

Due to all of the above, herein we propose to synthesize nanohydroxyapatite (nHAp) – nanocellulose (CNC) composites via the sol-gel route in order to develop uniform molecular-level mixing of the calcium and phosphorus precursors. This strategy might provide several advantages such as improving chemical homogeneity of the resulting HAp, low synthesis temperature, and promotion of controlled growth of spherical nanoparticles [16, 17]. The sol-gel product is recognized by the nanometric dimension of the primary particles that is known to improve the contact reaction and the stability at the artificial/natural bone interface [16, 18]. In the present paper we report the synthesis and characterization of nHAp with the incorporation of CNCs via the sol-gel method and its characterization using different proportions of the bionanomaterials for the creation of scaffolds that will contribute to the field of BTE. Through the evaluation of different proportions of the HAp and CNC it was possible to determine which proportion promoted a better synthesis of nHAp nanoparticles in terms of homogeneity and dispersion. We present the addition of bone morphogenetic protein (BMP-2) to the synthesized composites as it is an important protein involved in the development and regeneration of tissue and cartilage which makes it promising for our purpose [19].

Finally, we present the inclusion of osteoblast cells into the nanoconstructs with BMP-2 in order to determine the biocompatibility of these materials. Nanomaterials have proven to be noncytotoxic in previous studies [20–22].

## 2. Materials and Methods

**2.1. Materials.** Cellulose nanocrystals (CNCs) 11.8% aqueous solution was purchased from the University of Maine Process and Development Center (Orono, USA). Hydroxyapatite (HAp), ethanol, acetic acid, phosphate buffered solution 1x, pH = 7.2 (PBS), and bone morphogenetic protein 2 (BMP-2) were purchased from Sigma-Aldrich. All chemicals and solvents were used as received without further purification. Deionized water (18.3 MW, MilliQ Direct 16) was used at all times.

**2.2. Synthesis of Hydroxyapatite Nanoparticles with Cellulose Nanocrystals (nHAp-CNC) Composites.** In order to compare the effects of polysaccharide to BCD crystals, three composites were prepared with different proportions of HAp and CNC. The three compounds were prepared, following the proportions of Hap > CNC, Hap = CNC, and Hap < CNC. The same ratio of ethanol and acetic acid was used to produce nanohydroxyapatite (nHAp), following a similar procedure to that of Montreal Romero et al. [23]. In brief, 1 mL of 99% chemically pure grade biopolymer  $\beta$ -1,4-D-linked glucose (CNC) at 3.2% wt was placed at 30°C for 30 minutes and added to the solutions of HAp with 5 mL ethanol and 1.25 mL acetic acid for gel formation. The first solution (nHAp > CNC) was prepared using 0.5 g HAp and 9.17  $\mu$ L CNCs (3.2%), the second solution (nHAp = CNC) consisted of 0.5 g HAp and 458  $\mu$ L CNCs (3.2%), and the third solution (nHAp < CNC) consisted of 0.01 g HAp and 458  $\mu$ L CNCs (3.2%); subsequently the solutions were sonicated at 30°C for 15 minutes. After sonication each gel was placed in a 50 mL tube and centrifuged 3 times at 12,500 rpm for 5 minutes at 30°C; in-between the procedure, the concentrated gel was poured off and the precipitate was resuspended twice with deionized water to eliminate any amount of gel residue. The resulting pellet was freeze-dried for 24 hours and stored for further characterization.

**2.3. Inclusion of BMP-2 to nHAp.** For the inclusion of BMP-2 to the composites, 10  $\mu$ g of BMP-2 was diluted in 1000  $\mu$ L of PBS first. Afterwards, two solutions of 0.01 g of nHAp > CNC and nHAp = CNC were prepared in 900  $\mu$ L of PBS and 100  $\mu$ L of the solution containing the BMP-2 was added to each.

**2.4. Cell Proliferation and Viability Assay.** Human osteoblast cell line (hFOB 1.19) was purchased from the American Type Culture Collection (Manassas, VA, USA). Osteoblast cells were cultured in 1:1 mixture of Ham's F12 Medium/Dulbecco's Modified Eagle's Medium (Gibco by Life Technologies) supplemented with 2.5 mM L-glutamine, 10% fetal bovine serum (Gibco by Life Technologies), and 0.3 mg/mL G148 (Gibco by Life Technologies) at 34°C with 5% CO<sub>2</sub>. To assess the cell viability effect of HAp, CNC, Hap >

CNC, Hap = CNC, Hap > CNC + BMP-2, and Hap = CNC + BMP-2 nanoparticles, the MTS CellTiter 96 AQueous Solution Cell proliferation Assay (Promega) was used. In brief, cells were plated at  $7.5 \times 10^4$  cells/mL in 96-well plates (Falcon) in contact with 5 mg/mL of the different nanoconstructs and incubated for 24 hrs. Then, 20  $\mu$ L of MTS reagent was added and cells were incubated for 1 hr. Thereafter, the 96-well plates were centrifuged at 1000 rpm for 10 min to avoid any further light scattering from the nanomaterials. Then, 100  $\mu$ L of the supernatant was transferred to a new 96-well plate and absorbance was measured at 490 nm using a Synergy H1 Hybrid Microplate Reader from BioTek. The results were expressed as percentage (%) of cell viability and the statistical analysis was performed with GraphPad Prism 6.

**2.5. Physical Characterization of nHAp-CNC Composites.** In order to fully characterize the composite material, several physical characterization techniques were employed in this study.

**2.5.1. Thermogravimetric Analysis (TGA).** A Perkin-Elmer STA 6000 simultaneous thermal analyzer was used to measure the changes in weight and heat flow as a function of temperature. Approximately 10 mg of each sample was added to ceramic crucible and heating of 30–750°C at a ramp of 20°C/min in air atmosphere at a flow rate of 20 mL/min.

**2.5.2. X-Ray Diffraction (XRD) Analysis.** Powder X-ray diffraction measurements were conducted over 10 to 90° 2 $\theta$  range using a Rigaku SmartLab diffractometer at 40 kV and 44 mA equipped with monochromatic CuK $\alpha$  (1.54 Å) X-ray radiation. X-ray diffraction patterns of composites were recorded in intervals of 20°C.

**2.5.3. Dynamic Light Scattering (DLS) and Z-Potential Analysis.** Malvern ZetaSizer Nano Series with 4 mW 632.8 nm laser was used to determine the average diameter of composite suspensions. First, suspensions were sufficiently diluted with deionized water to avoid agglomeration; then approximately 1 mL of suspension was added to a disposable plastic cuvette. The backscattering mode was used in triplicate for all the samples and the Z-average (i.e., hydrodynamic radius) and polydispersity index (PDI) were recorded.

**2.5.4. Scanning Electron Microscopy (SEM).** Scanning electron microscopy (SEM) images were recorded using a JEOL 5800LV Scanning Microscope with electron beam energy of 20 kV. The samples were freeze-dried before measurement and, to avoid charge accumulation, a thin film of gold (15 nm) was added to the surface.

**2.5.5. Infrared Spectroscopy (FTIR).** Infrared spectra of freeze-dried samples were recorded on a Bruker tensor 27 Fourier transform infrared using Attenuated Total Reflectance (ATR). Sample was placed in a glass slide and then pressed using a diamond probe. The spectral width

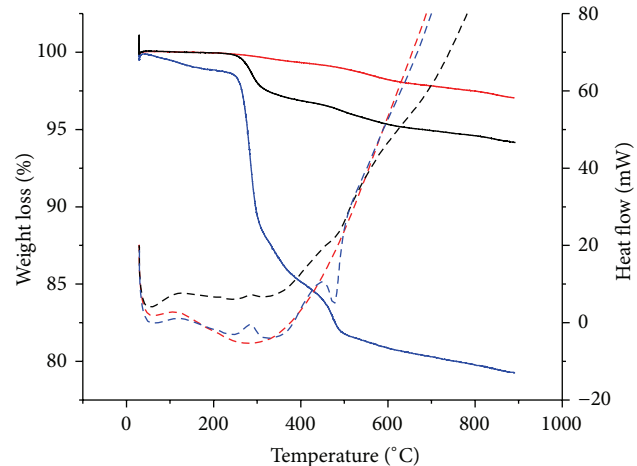


FIGURE 1: TGA and DSC analysis of nHAp > CNC (red), nHAp = CNC (black), and nHAp < CNC (blue), in air atmosphere at 20 mL/min and a ramp of 20°C/min.

ranged from 400 to 4000 cm $^{-1}$ , with 4 cm $^{-1}$  resolution and accumulation of 64 scans.

### 3. Results and Discussion

**3.1. Physical Characterization.** The main objective of this work was to prepare and characterize biocompatible constructs for Bone Tissue Engineering and repair. Nevertheless, it was of interest to extensively characterize the prepared materials to account for any structural or chemical changes in the products. In this sense, thermal stability of the material provides an indication of the interactions between particles and also about the critical transition temperatures in the material. In order to determine this, a dual thermal gravimetric analyzer with differential scanning calorimetry functions was utilized and results are shown in Figure 1. This figure shows the weight loss (straight lines) and heat flow (dotted lines) of the different nHAp-CNC constructs. From these results, a temperature drop at ca. 300°C was consistently observed and is ascribed to the thermal decomposition of the CNC while the nHAp decomposition transition was not observed as it belongs to a region of approximately 1080°C, although some mass loss is present. The decomposition of nHAp occurs in three steps: (1) the appearance of  $\text{Ca}_{10}(\text{PO}_4)_6\text{O}_x(\text{OH})_{2-2x}$  as a transition product for the (2) dehydroxylation producing oxyapatite  $\text{Ca}_{10}(\text{PO}_4)_6\text{O}$  ending with (3) decomposition of this oxyapatite and resulting calcium phosphates [24]. The mass losses belonging to the first two steps can be observed at around 400°C and 600°C, respectively, for each sample. The nHAp > CNC sample (red) is the most stable of all, maybe due to the higher proportion of Hap, followed by the nHAp = CNC (black) with a well-defined transition belonging to the CNC and nHAP. Lastly, the nHAp < CNC sample (blue) shows less thermal stability due to a lower amount of CNC in the sample in comparison to the nHAp with a higher change in mass loss at 300°C belonging to the CNC. Also, in this sample a transition at

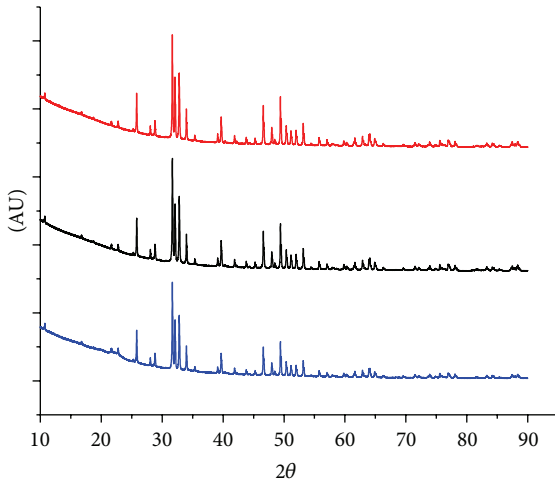


FIGURE 2: Powder XRD analysis of nHAp > CNC (red), nHAp = CNC (black), and nHAp < CNC (blue).

*ca.* 450°C ascribed to the mass loss from the first step of the decomposition of nHAp appears to be more significant. This behavior may be due to the expected stronger interaction between nHAp and CNC that will ultimately cause heat dissipation in order to reach the transition product. The heat flow results also evidence the evaporation of remaining water in the samples. The transitions ascribed to the water removal are not very noticeable in the gravimetric results at *ca.* 130°C. These results suggest a correlation between the ratio of nHAp and the thermal stability. It is noticeable that the samples with higher hydroxyapatite content provide better thermal stability as it was expected due to the degradation temperature of nHAp being much higher than that of CNC.

After observing the variations in thermal stability of the constructs, it was important to determine if any crystallinity loss is observed for the prepared materials. In order to assess this, XRD was carried out and the resulting patterns are shown in Figure 2. The CNC peaks can be observed between 10° and 25° with characteristic phases of (110) at 17° and (200) at 26°; a zoomed version of this area can be observed in Figure 3 [25, 26]. The nHAp characteristic phases are observed at 32°, 39°, and 49° with peaks corresponding to the phases of (311), (410), and (313), respectively (COD ID 2300273) [26]. As a qualitative observation, the intensity of the CNC peaks is much lower than those of the nHAp due to the high crystallinity of nHAp in comparison to CNC, but this does not mean that the CNC loses crystallinity. As can be observed, all diffraction patterns showed the same behavior leading to the conclusion that the crystallinity of the sample was not compromised after sol-gel reaction with polysaccharide network. It is important to note that as the crystallinity of the cellulose decreases, the level of water absorption and biodegradability increases because with decreasing crystallinity cellulose fibers get more disorganized and hence more susceptible to degradation processes [27]. Because of this, the CNC in the synthesized composite will not degrade which sustains the initial purpose of using CNC that can serve as a hardening agent due to its high Young's

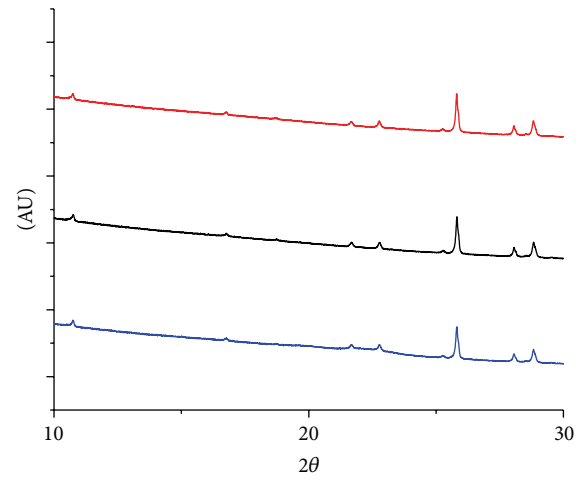


FIGURE 3: Powder XRD analysis of CNC phase in nHAp > CNC (red), nHAp = CNC (black), and nHAp < CNC (blue).

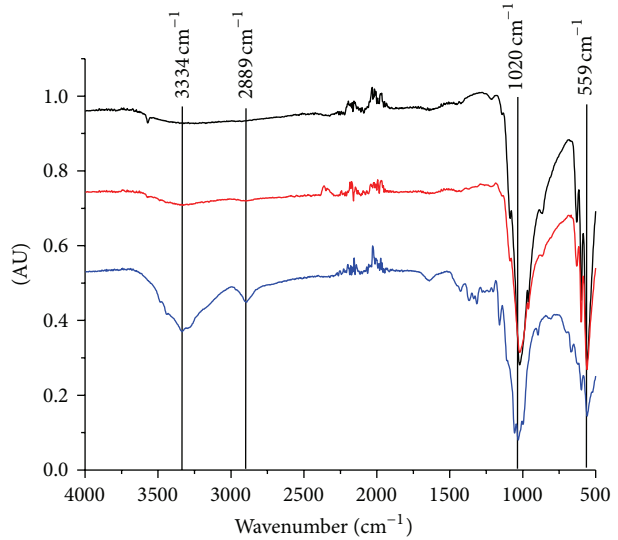


FIGURE 4: FTIR analysis of nHAp > CNC (red), nHAp = CNC (black), and nHAp < CNC (blue).

modulus and reinforcing the strength of the bone. It is also possible that this polymer network formed by cellulose may prevent the mineralization of HAp and deposition in the intra-articular and periarticular locations.

Moreover, even when the crystallinity of the samples was conserved, it was of our interest to determine any chemical changes in the surface of the composites after the synthesis. FTIR was carried out from 400 to 4000 cm⁻¹ (Figure 4) and the presence of CNC is confirmed by the band at around 3400 cm⁻¹ due to OH-stretching, the band at 1640 cm⁻¹ likely due to the OH-bending vibration of adsorbed water, and the band at 2889 cm⁻¹ assigned to C-H aliphatic stretching. Other noticeable bands from C-O-C (ether) at 1200 cm⁻¹ and CH<sub>2</sub> (alkaline) at 692 cm⁻¹ are also worth noting. It is important to observe that even though nHAp is an ionic compound, its anions (PO<sub>4</sub><sup>2-</sup>) are present at 1020 cm⁻¹ and

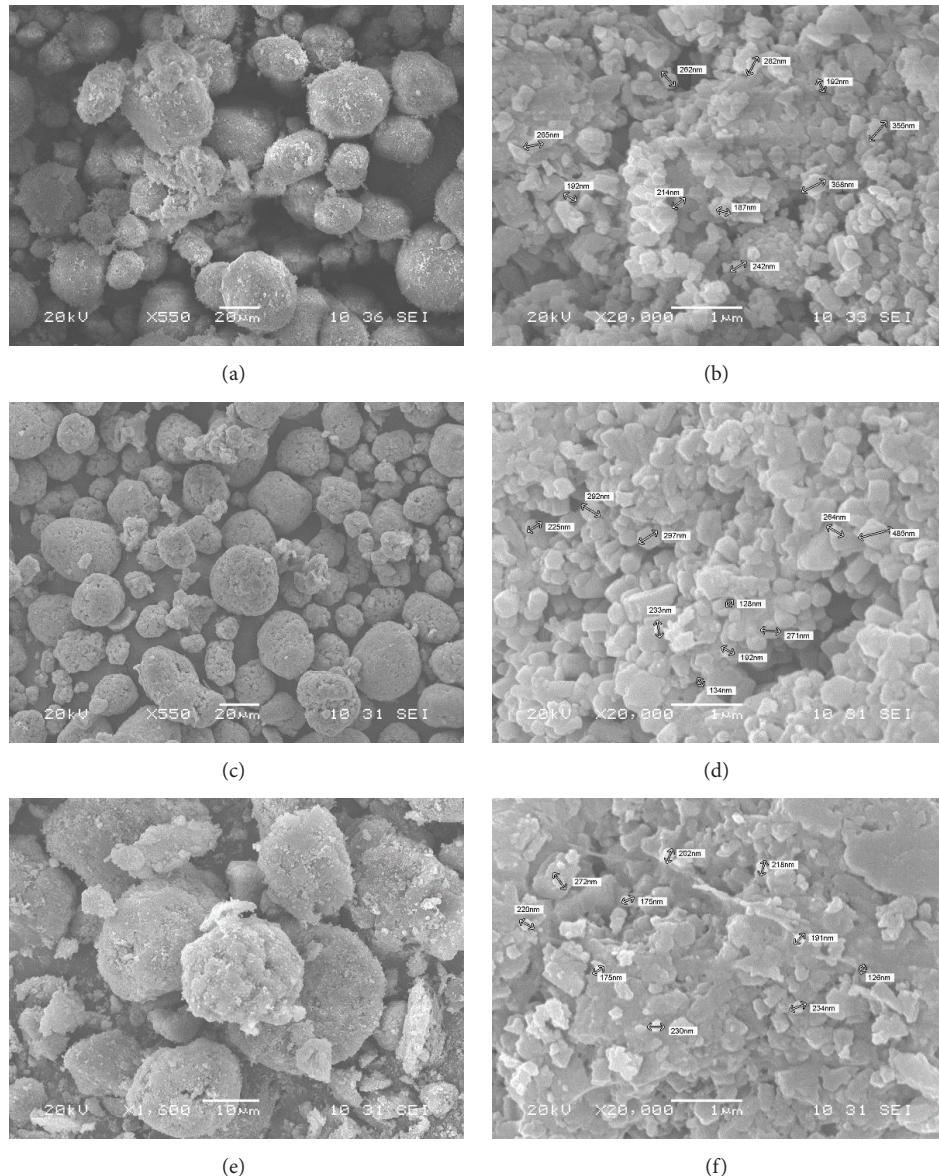
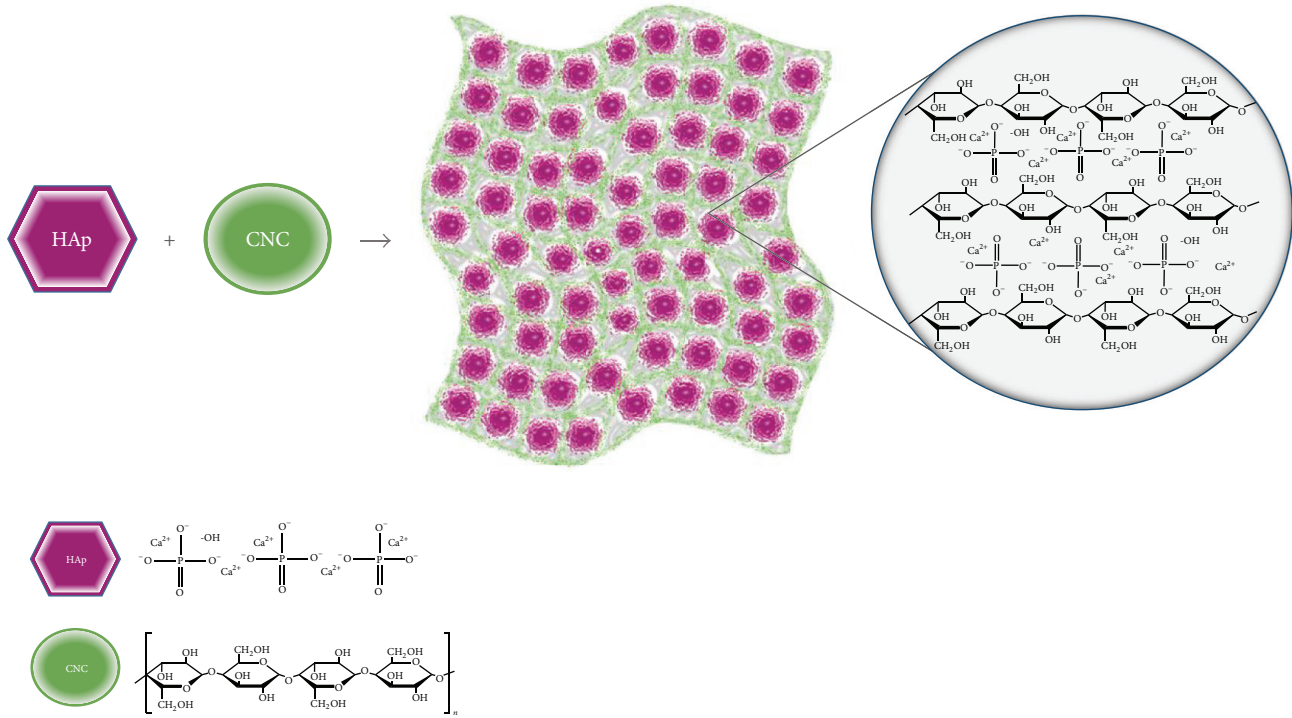


FIGURE 5: SEM analyses of nHAp > CNC (a and b), nHAp = CNC (c and d), and nHAp < CNC (e and f).

559 cm<sup>-1</sup>. The peaks around 2000 cm<sup>-1</sup> are attributed to the presence of CO<sub>2</sub> in the samples, so these were discarded for the analysis of the spectrum. The effect of proportion is clearly visible, especially in nHAp < CNC, in the intensity of the graphs.

It has been noted that the composite size and homogeneity of the particles can influence the adherence of tissue to the host implant. As a strategy to account for the composite size, DLS analyses were conducted and are shown in Table 1. First, the size for natural HAp and CNC was determined and then the analysis of the particle size and distribution for the composites was carried out. As can be observed for the Z-average ( $R_H$ ) results, most particles fluctuated between 289 and 311 nm. The results showed that the sizes for the nanoparticles were 311 nm for the nHAP > CNC, 289 nm for the nHAp = CNC, and 307 nm for the nHAp < CNC composites. The

polydispersive index (PDI) for the nHAP > CNC and nHAp = CNC samples was the lowest with a value of 0.21 which indicates a good size uniformity of the particles, a factor that is notably missing in the nHAp < CNC. The average reduction of particle size from starting natural HAp with an average size of 2061 nm is approximately 85.7%, which proves that the polymer network was a determining factor in this size reduction; a representation of this interaction can be observed in Scheme 1. To further verify this, SEM was carried out to correlate the size and homogeneity of the composites and is presented in Figure 5. From these images it can be observed that the nHAp > CNC sample presents a high porosity while the nHAp = CNC showed a better uniformity in the spherical shape, distribution, and particle size and the nHAp < CNC showed neither of these. Also, in agreement with DLS, the sizes of the particles are between 150 and 300 nm with



SCHEME 1: Representation of the interaction between nanohydroxyapatite (nHAp) and cellulose nanocrystals (CNCs) polymer network.

TABLE 1: DLS analyses for HAp, CNC, and nHAp-CNC at a 1% w/v.

Sample*	Z-average (nm)	PDI
nHAp > CNC (3.2%)	311 ± 7	0.21 ± 0.02
nHAp = CNC (3.2%)	289 ± 3	0.21 ± 0.01
nHAp < CNC (3.2%)	307 ± 5	0.43 ± 0.00
Natural HAp	1965 ± 170	0.29 ± 0.04
CNC	142.3 ± 0.72	0.30 ± .007

\* All samples at H<sub>2</sub>O (10 mg/mL) at pH = 7.07.

few particles whose size is over 300 nm. The presence of submicron particles is attributed to the aggregation factor that occurs when the solution is in suspension; nevertheless the formation of smaller nanoparticles is present. DLS was also carried out for the BMP-2 protein alone and with its incorporation to the composites, a representation of this interaction can be observed in Scheme 2. The BMP-2 size was found to be 59.97 nm and for the nHAp < CNC and nHAp = CNC composites with the protein, it was observed that the size of the nanoparticles remained around 349 nm which is still in the range of our composites without the protein with a PDI of 0.24 (Table 2). These results in fact corroborate that the sol-gel method followed by Montreal Romero et al. is, in fact, effective for these types of materials [23].

After thorough characterization of the composites, Z-potential was performed in order to determine the overall charge of the nHAp > CNC and nHAp = CNC composites with and without the BMP-2 (Table 3). The analyses were run in PBS in order to understand how the composites would behave under physiological conditions. The overall

TABLE 2: DLS analyses for BMP-2, nHAp > CNC, and nHAp = CNC composites with protein at 1% w/v.

Sample*	Z-average (nm)	PDI
nHAp > CNC (3.2%) + BMP-2	333.4 ± 11	0.18 ± 0.01
nHAp = CNC (3.2%) + BMP-2	364.6 ± 2	0.30 ± 0.02
BMP-2	59.97 ± 0.9	0.46 ± 0.04

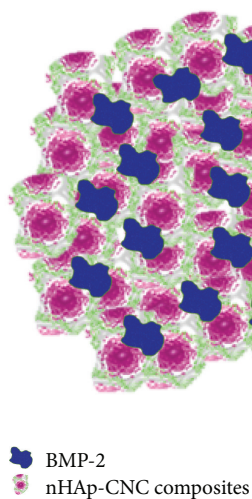
\* All samples in PBS at pH = 7.20.

TABLE 3: Zeta potential measurements of nHAp > CNC and nHAp = CNC with BMP-2.

Sample	Zeta potential (mV)
Natural HAp	-20 ± 2
BMP-2	-11.4 ± 0.7
nHAp > CNC	-18 ± 1
nHAp = CNC	-11.0 ± 0.6
nHAp > CNC & BMP-2	-17.3 ± 0.6
nHAp = CNC & BMP-2	-20 ± 2

\* All samples at 1 mg/mL in PBS solvent at pH = 7.2.

charge of the HAp alone was found to have an average charge of -19.36 mV. The isoelectric point of the BMP-2 is 8.5 and therefore below this value the BMP-2 will be positively charged [28]. When the Z-potential measurement was performed with the protein alone, the charge was -12.8 mV, which indicates that there is in fact an interaction occurring between the protein and composite. A recent study about thermodynamics studies on the BMP-2 adsorption onto different hydroxyapatite surfaces conducted by Lu and



BMP-2  
nHAp-CNC composites

SCHEME 2: Representation of the interaction between the nHAp/CNC nanocomposites with the BMP-2.

team has reported that the process of adsorption is by physisorption where the initial driving force is governed by an electrostatic interaction between HAp (negatively charged at pH = 7.2) and BMP-2 (positively charged at pH = 7.2). They report that this process has a positive  $\Delta H$  corresponding to an endothermic process and negative  $\Delta G$  corresponding to a spontaneous and energetically favored process [29]. The composites alone had an average charge of -11.4 and -18.1 mV for the nHAp > CNC and nHAp = CNC, respectively, and the charges with the BMP-2 were lowered to -11.0 and -17.3 mV, respectively. Several studies have already shown that the incorporation of BMP-2 results in an initial burst release followed by a stable sustained release of the protein [30]. This slight decrease in the overall charge suggests that there is in fact an interaction between the composites and the protein although this does not provide any inquiry over the stability of the construct.

**3.2. Biocompatibility of Nanocomposites with Osteoblast Cells.** In recent years, a great interest has been dedicated to the development of biocompatible and nontoxic nanoparticles that can be used in bone implants and biomedical devices. For instance, studies with carbon nanotubes have been shown to support the osteoblastic cells grow. However, the hydrophobic nature of carbon nanotubes requires extensive functionalization with hydrophilic conjugates in order to afford its biocompatibility [31]. Here in this study we used biocompatible nanohydroxyapatite/nanocellulose composites. To examine the effect in cell viability of such nanoconstructs, osteoblasts cells were exposed to 5 mg/mL of nHAp, CNC, nHAp > CNC, nHAp = CNC, nHAp > CNC + BMP-2, and nHAp = CNC + BMP-2 nanoparticles for 24 hrs. Then, cell viability was measured by MTS assay. The results for these experiments are shown in Figure 6 and it demonstrates that neither of the compounds compromised the osteoblast cell viability. As can be noted, the nHAp > CNC + BMP-2 composite had the highest growth of osteoblast in comparison to the others.

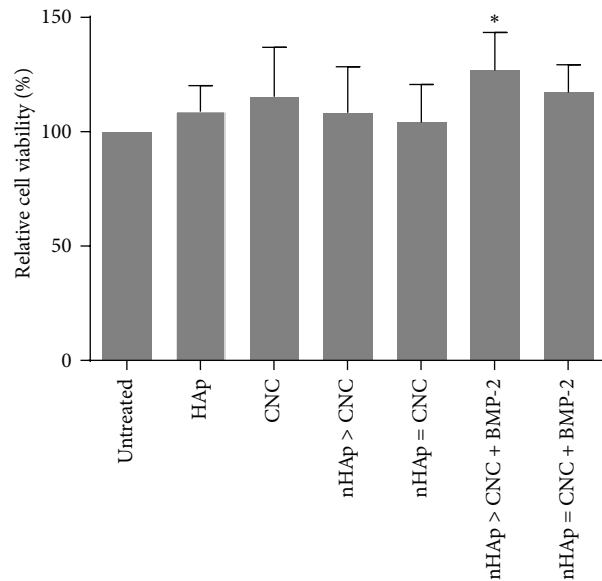


FIGURE 6: Cell viability in human osteoblasts exposed to the different nanoconstructs. The cells were exposed to 1 mg/mL of HAp, CNC, HAp > CNC, HAp = CNC, HAp > CNC + BMP-2, and HAp = CNC + BMP-2 nanoconstructs for 24 h and cell viability was determined with the MTS reduction assay. Values represent mean  $\pm$  standard error of the mean (SEM) from three replicates. An asterisk indicates statistical significance in comparison with the untreated samples ( $p < 0.05$ ).

This result was expected given the fact that one of the reasons HAp was chosen is because of its high porosity in which the pore size of these scaffolds as long as it is equal to or bigger than 20  $\mu\text{m}$  will permit the growth of cells [32].

Recent studies have shown that the use of hydroxyapatite-(HA)-2,2,6,6-tetramethylpiperidine-1-oxyl- (TEMPO-) oxidized bacterial cellulose- (TOBC-) GEL composites in calvarial osteoblasts from Sprague-Dawley rats did not compromise the cell viability and promote cell proliferation [33]. Furthermore, other studies have demonstrated that poly-L-lactide acid (PLLA)/HA/cellulose composites did not affect the cell viability of rat osteosarcoma cells (URM-106) [34]. In this study we showed that the use of nHAp > CNC with BMP-2, which is an important protein that regulates osteoblast differentiation, promotes the growth of human fetal osteoblast cells (Figure 6). Taken together, these results might suggest that cellulose nanocomposites with the addition of proteins that are important for osteoblast growth and differentiation such as BMP-2 are suitable for biomedical applications in the field of Bone Tissue Engineering.

#### 4. Conclusion

The proportion of the nHAp = CNC ratio appeared to be the most suitable ratio for this methodology as it provides homogeneity of the particle's size and distribution that was shown by the DLS and SEM analyses. We conclude that the CNC did work as expected by the sol-gel method to include HAp in its network without affecting its degree of

crystallinity, as shown by the XRD analyses, or the thermal stability as shown by the TGA. Neither of the properties of either CNC or HAp changed due to the chemical interaction between them. The inclusion of BMP-2 does not appear to have a negative effect on the particle size and the charge reduction indicates that there is an interaction between the protein and the composite. The cell proliferation and viability assays demonstrated that all of our composites promoted an increased cell growth, but the nHAp > CNC ratio with BMP-2 had a higher growth percentage than the other composites. Therefore it appears to be the best nanocomposite for the fabrication of scaffolds or bioactive layers that can be used in the Bone Tissue Engineering field.

## Conflict of Interests

The authors declare no competing financial interests.

## Authors' Contribution

The paper was written through contributions of all authors. All authors have given approval to the final version of the paper. Claudia S. Herdicia-Lluberes and Simara Laboy-López contributed equally to this work.

## Acknowledgments

Claudia S. Herdicia-Lluberes is grateful for the support of the UPR-RP Honors Program. The authors acknowledge the UPR Materials Characterization Center (MCC) for the provided support during the attainment of this work. Also, Carlos García and Karlene Vega are acknowledged for their help with all osteoblast cells related experiments. Institutional resources as seed funds were received during the attainment of this work. This work was also supported in part by the NASA Experimental Program to Stimulate Competitive Research (EPSCoR) under Grant no. NNX14AN18A.

## References

- [1] H. Liu, H. Peng, Y. Wu et al., "The promotion of bone regeneration by nanofibrous hydroxyapatite/chitosan scaffolds by effects on integrin-BMP/Smad signaling pathway in BMSCs," *Biomaterials*, vol. 34, no. 18, pp. 4404–4417, 2013.
- [2] A. R. Amini, C. T. Laurencin, and S. P. Nukavarapu, "Bone tissue engineering: recent advances and challenges," *Critical Reviews in Biomedical Engineering*, vol. 40, no. 5, pp. 363–408, 2012.
- [3] S. Laib, B. H. Fellah, A. Fatimi et al., "The in vivo degradation of a ruthenium labelled polysaccharide-based hydrogel for bone tissue engineering," *Biomaterials*, vol. 30, no. 8, pp. 1568–1577, 2009.
- [4] S. Bose, M. Roy, and A. Bandyopadhyay, "Recent advances in bone tissue engineering scaffolds," *Trends in Biotechnology*, vol. 30, no. 10, pp. 546–554, 2012.
- [5] N. Pramanik, D. Mishra, I. Banerjee, T. K. Maiti, P. Bhargava, and P. Pramanik, "Chemical synthesis, characterization, and biocompatibility study of hydroxyapatite/chitosan phosphate nanocomposite for bone tissue engineering applications," *International Journal of Biomaterials*, vol. 2009, Article ID 512417, 8 pages, 2009.
- [6] C. W. Hayes and W. F. Conway, "Calcium hydroxyapatite deposition disease," *Radiographics*, vol. 10, no. 6, pp. 1031–1048, 1990.
- [7] H.-K. Ea and F. Lioté, "Advances in understanding calcium-containing crystal disease," *Current Opinion in Rheumatology*, vol. 21, no. 2, pp. 150–157, 2009.
- [8] G. M. Garcia, G. C. McCord, and R. Kumar, "Hydroxyapatite crystal deposition disease," *Seminars in Musculoskeletal Radiology*, vol. 7, no. 3, pp. 187–193, 2003.
- [9] C. Nguyen, M. Lieberherr, C. Bordat et al., "Intracellular calcium oscillations in articular chondrocytes induced by basic calcium phosphate crystals lead to cartilage degradation," *Osteoarthritis and Cartilage*, vol. 20, no. 11, pp. 1399–1408, 2012.
- [10] S. Facca, D. Lahiri, F. Fioretti et al., "In vivo osseointegration of nano-designed composite coatings on titanium implants," *ACS Nano*, vol. 5, no. 6, pp. 4790–4799, 2011.
- [11] L. L. Hyland, M. B. Taraban, B. Hammouda, and Y. B. Yu, "Mutually reinforced multicomponent polysaccharide networks," *Biopolymers*, vol. 95, no. 12, pp. 840–851, 2011.
- [12] S. C. Chao, M. J. Wang, N. S. Pai, and S. K. Yen, "Preparation and characterization of gelatin-hydroxyapatite composite microspheres for hard tissue repair," *Materials Science & Engineering C: Materials for Biological Applications*, vol. 57, pp. 113–122, 2015.
- [13] A. Dufresne, "Nanocellulose: a new ageless bionanomaterial," *Materials Today*, vol. 16, no. 6, pp. 220–227, 2013.
- [14] R. M. A. Domingues, M. E. Gomes, and R. L. Reis, "The potential of cellulose nanocrystals in tissue engineering strategies," *Biomacromolecules*, vol. 15, no. 7, pp. 2327–2346, 2014.
- [15] A. Salam, L. A. Lucia, and H. Jameel, "A novel cellulose nanocrystals-based approach to improve the mechanical properties of recycled paper," *ACS Sustainable Chemistry and Engineering*, vol. 1, no. 12, pp. 1584–1592, 2013.
- [16] T. A. Kuriakose, S. N. Kalkura, M. Palanichamy et al., "Synthesis of stoichiometric nano crystalline hydroxyapatite by ethanol-based sol-gel technique at low temperature," *Journal of Crystal Growth*, vol. 263, no. 1–4, pp. 517–523, 2004.
- [17] J. Klinkaewnarong and E. Swatsitang, "Synthesis of nanocrystalline hydroxyapatite by natural biopolymers based Sol-Gel technique," in *II. Bio-Materials and Biomimetic Materials*, vol. 747 of *Advanced Materials Research*, pp. 83–86, 2013.
- [18] A. K. Nayak, "Hydroxyapatite synthesis methodologies: an overview," *International Journal of ChemTech Research*, vol. 2, no. 2, pp. 903–907, 2010.
- [19] S. S. Lee, B. J. Huang, S. R. Kaltz et al., "Bone regeneration with low dose BMP-2 amplified by biomimetic supramolecular nanofibers within collagen scaffolds," *Biomaterials*, vol. 34, no. 2, pp. 452–459, 2013.
- [20] J. Chłopek, B. Czajkowska, B. Szaraniec, E. Frackowiak, K. Szostak, and F. Béguin, "In vitro studies of carbon nanotubes biocompatibility," *Carbon*, vol. 44, no. 6, pp. 1106–1111, 2006.
- [21] L. P. Zanello, B. Zhao, H. Hu, and R. C. Haddon, "Bone cell proliferation on carbon nanotubes," *Nano Letters*, vol. 6, no. 3, pp. 562–567, 2006.
- [22] S. Baradarani, E. Moghaddam, B. Nasiri-Tabrizi et al., "Characterization of nickel-doped biphasic calcium phosphate/graphene nanoplatelet composites for biomedical application," *Materials Science and Engineering C*, vol. 49, pp. 656–668, 2015.

- [23] H. A. Monreal Romero, J. Mora Ruacho, C. A. Martínez Pérez, and P. E. García Casillas, "Synthesis of hydroxyapatite nanoparticles in presence of a linear polysaccharide," *Journal of Materials*, vol. 2013, Article ID 683268, 5 pages, 2013.
- [24] T. Wang, A. Dorner-Reisel, and E. Müller, "Thermogravimetric and thermokinetic investigation of the dehydroxylation of a hydroxyapatite powder," *Journal of the European Ceramic Society*, vol. 24, no. 4, pp. 693–698, 2004.
- [25] C. Echeverria, P. L. Almeida, G. Feio, J. L. Figueirinhas, and M. H. Godinho, "A cellulosic liquid crystal pool for cellulose nanocrystals: structure and molecular dynamics at high shear rates," *European Polymer Journal*, vol. 72, pp. 72–81, 2015.
- [26] Y. Tang, X. Shen, J. Zhang, D. Guo, F. Kong, and N. Zhang, "Extraction of cellulose nano-crystals from old corrugated container fiber using phosphoric acid and enzymatic hydrolysis followed by sonication," *Carbohydrate Polymers*, vol. 125, pp. 360–366, 2015.
- [27] A. M. de Araujo Junior, G. Braido, S. Saska et al., "Regenerated cellulose scaffolds: preparation, characterization and toxicological evaluation," *Carbohydrate Polymers*, vol. 136, pp. 892–898, 2016.
- [28] M. L. Macdonald, R. E. Samuel, N. J. Shah, R. F. Padera, Y. M. Beben, and P. T. Hammond, "Tissue integration of growth factor-eluting layer-by-layer polyelectrolyte multilayer coated implants," *Biomaterials*, vol. 32, no. 5, pp. 1446–1453, 2011.
- [29] Z. Lu, C. Huangfu, Y. Wang et al., "Kinetics and thermodynamics studies on the BMP-2 adsorption onto hydroxyapatite surface with different multi-morphological features," *Materials Science & Engineering C: Materials for Biological Applications*, vol. 52, pp. 251–258, 2015.
- [30] M. Ventura, O. C. Boerman, G. M. Franssen, E. Bronkhorst, J. A. Jansen, and X. F. Walboomers, "Monitoring the biological effect of BMP-2 release on bone healing by PET/CT," *Journal of Controlled Release*, vol. 183, pp. 138–144, 2014.
- [31] X. Li, H. Gao, M. Uo et al., "Maturation of osteoblast-like Saos2 induced by carbon nanotubes," *Biomedical Materials*, vol. 4, no. 1, Article ID 015005, 2009.
- [32] L. Kong, Y. Gao, W. Cao, Y. Gong, N. Zhao, and X. Zhang, "Preparation and characterization of nano-hydroxyapatite/chitosan composite scaffolds," *Journal of Biomedical Materials Research Part A*, vol. 75, no. 2, pp. 275–282, 2005.
- [33] M. Park, D. Lee, S. Shin, and J. Hyun, "Effect of negatively charged cellulose nanofibers on the dispersion of hydroxyapatite nanoparticles for scaffolds in bone tissue engineering," *Colloids and Surfaces B: Biointerfaces*, vol. 130, pp. 222–228, 2015.
- [34] S. Eftekhari, I. El Sawi, Z. S. Bagheri, G. Turcotte, and H. Bougheara, "Fabrication and characterization of novel biomimetic PLLA/cellulose/hydroxyapatite nanocomposite for bone repair applications," *Materials Science and Engineering C*, vol. 39, no. 1, pp. 120–125, 2014.

## Research Article

# Comparison of Fibroblast and Osteoblast Response to Cultivation on Titanium Implants with Different Grain Sizes

Vaclav Babuska,<sup>1</sup> Jana Dobra,<sup>1</sup> Vlastimil Kulda,<sup>1</sup> Michaela Kripnerova,<sup>2</sup> Amin Moztarzadeh,<sup>1</sup> Lukas Bolek,<sup>3</sup> Jiri Lahoda,<sup>4</sup> and Daniel Hrusak<sup>5</sup>

<sup>1</sup>Department of Medical Chemistry and Biochemistry, Faculty of Medicine in Pilsen, Charles University in Prague, Karlovarská 48, 301 66 Pilsen, Czech Republic

<sup>2</sup>Department of Biology, Faculty of Medicine in Pilsen, Charles University in Prague, Alej Svobody 76, 323 00 Plzen, Czech Republic

<sup>3</sup>Biomedical Center, Faculty of Medicine in Pilsen, Charles University in Prague, Alej Svobody 76, 323 00 Pilsen, Czech Republic

<sup>4</sup>Department of Applied Electronics and Telecommunications, Faculty of Electrical Engineering, University of West Bohemia, Univerzitní 26, 306 14 Pilsen, Czech Republic

<sup>5</sup>Department of Stomatology, Faculty of Medicine in Pilsen, University Hospital and Charles University, Alej Svobody 80, 301 00 Pilsen, Czech Republic

Correspondence should be addressed to Vaclav Babuska; [vaclav.babuska@lfp.cuni.cz](mailto:vaclav.babuska@lfp.cuni.cz)

Received 24 September 2015; Revised 23 November 2015; Accepted 26 November 2015

Academic Editor: Daniel S. Oh

Copyright © 2015 Vaclav Babuska et al. This is an open access article distributed under the Creative Commons Attribution License, which permits unrestricted use, distribution, and reproduction in any medium, provided the original work is properly cited.

The *in vitro* response of human fibroblast cell line HFL1 and human osteoblast cell line hFOB 1.19 on nanostructured titanium with different grain sizes has been compared in the present study. Used samples of titanium produced by equal channel angular (ECA) pressing have grain sizes of 160 nm, 280 nm, and 2400 nm with cross- and longitudinal sections. Similar cellular behaviour was observed on all studied biomaterials. There were significant differences related to the initial phase of attachment, but not in proliferation. Furthermore, the results indicate that osteoblasts grow best on material with grain size of 160 nm with a longitudinal section in comparison with other examined materials. Therefore, this material could be recommended for further evaluation with respect to osseointegration *in vivo*.

## 1. Introduction

Titanium is commonly used for dental as well as orthopaedic implants due to its properties such as biocompatibility, nontoxicity, and corrosion resistance. [1–10]. However, commercially pure titanium (cpTi) has excellent biocompatibility but relatively poor strength, and titanium alloys have superior strength but they contain potentially toxic or allergic ingredients [11, 12]. Long-term stability of the titanium implants is related to their wear resistant properties. Loosening or failure of the implant can be caused by inflammation and bone resorption induced by the wear debris in the form of titanium particles derived from the implants entering into the surrounding tissues [13]. Therefore, it is essential to improve the biocompatibility and wear resistance of a titanium implant for its successful long-term survival [14].

An important direction intensively developed in recent years is the investigation of mechanical properties of nanostructured materials. The formation of nanostructures in metals leads to higher strength. There is great interest in the processing of bulk, fully dense nanostructured metals and alloys. The fabrication of such materials based on severe plastic deformation (SPD) methods seems very interesting and useful. The first developments and investigation of nanostructured materials processed using SPD methods were carried out by Valiev and colleagues more than two decades ago [15–17]. The method for large plastic deformations and formation of nanostructures in our study was equal channel angular (ECA) pressing. The ECA pressing method was carried out by deformation of massive billets via pure shear. Its goal is to introduce an intense plastic strain into materials without changing the cross-section area of billets. Due to

that, their repeat deformation is possible. The method was further developed and applied as an SPD method for processing structures with submicron and nanometric grain sizes. Nanostructured titanium produced by SPD processing binds together the advantages of aforementioned materials, that is, excellent biocompatibility and extraordinary mechanical properties [11, 18]. There are not many companies producing bulk nanotitanium and the cost of this material is very high, approximately 10 times higher than conventional titanium [19].

It is known that nanostructuring of material changes its biological properties compared with material of the same chemical composition, but the mechanism of this phenomenon has not yet been clarified [20]. The first evidence of such an effect was provided by Webster et al. in 1999, who found that osteoblast adhesion and bone formation significantly increased on nanostructured titanium surface compared with conventional titanium [21]. Since that time many *in vitro* as well as *in vivo* studies have investigated the impact of the nanostructured surface on the behaviour of cells and provide evidence that key biological processes, such as proliferation, gene expression, and initial protein adsorption that control such events, can be easily manipulated by modifying the nanotopography of implants [22–24]. It has also been proven that cells sense and react to nanotopography, by exhibiting changes in cell morphology, orientation, and cytoskeletal organisation [25–27].

An important issue is to improve osseointegration of an implant to its surrounding natural bone tissue [14, 28]. The long-term success of a dental implant depends not only on the integrity of osseointegration but also on the contact with surrounding soft tissue [29–31]. It is well known that cellular behaviour, such as adhesion, morphologic change, migration, functional alteration, and proliferation, is determined by surface properties such as composition, surface energy, topography, and roughness [32–35]. Nanotopography of an implant improves and accelerates osseointegration [19, 36]. Cell lines have been widely investigated as model systems to explore the influence of nanoscale surface topography on cellular response [37].

The aim of the present study was to compare nanostructured titanium with different grain size with respect to biocompatibility using human fibroblast cell line HFL1 as well as human osteoblast cell line hFOB 1.19.

## 2. Material and Methods

**2.1. Materials.** All the samples were obtained from commercially pure titanium (cpTi) by the ECA pressing method from cpTi grade 2. They have a cylinder shape with a diameter of 4.98–5.05 mm and height of 2.93–3.01 mm (Figure 1(a)). Used samples of titanium have grain sizes of 160 nm, 280 nm, and 2400 nm. For each grain size there were two types of sample: cross-section (–) and longitudinal section (+) (Figures 1(c) and 1(d), resp.).

Each implant was cleaned and sterilised before usage. The procedure contains incubation in a trypsin solution (0.25% (w/v) Trypsin-0.53 nM EDTA solution, PAA Laboratories GmbH, Austria) (30 minutes, 37°C), followed by incubation

in an ultrasonic bath (20 minutes, 25°C) incubation in acetone (20 minutes, 25°C), and at the end rinse in 70% ethanol and deionised water. Finally the implants were sterilised by autoclaving.

**2.2. Characterization of Surfaces.** All the sample types with different grain sizes and sections were analysed by scanning electron microscopy (SEM; JSM 6380, JEOL, Japan). Secondary electron channel was used for the observation.

The surface roughness of each sample was measured three times using a mechanical contact profilometer Surtronic 25 (Taylor Hobson, UK). Surface roughness of samples was quantified by arithmetical mean roughness  $R_a$  (defined as arithmetic average of the absolute values of the profile height deviations from the mean line) and ten-point mean roughness  $R_z$  (defined as the sum of the average value of absolute values of the heights of five highest profile peaks and the depths of five deepest profile valleys measured in the vertical magnification direction from the mean line). The surface roughness was measured at a traverse speed of 1 mm/s with a diamond-tipped stylus with 5 μm radius. The average of the three measurements was recorded as the mean surface roughness for each specimen.

**2.3. Cell Cultures.** Both used cell lines were obtained from ATCC (American type culture collection, Rockville, MD, USA) and cultured in accordance with ATCC recommendations. Culture media were refreshed as needed.

Human fetal lung fibroblasts (HFL1, ATCC, and CCL153) were cultivated in F12K Medium (PAA Laboratories GmbH, Austria) supplemented with 10% (v/v) fetal bovine serum (FBS, PAA Laboratories GmbH, Austria), 100 U/mL penicillin and 100 mg/mL streptomycin (PAA Laboratories GmbH, Austria), and 2.5 mM L-glutamine (Gibco, Life Technologies, Paisley, UK) at 37°C under 5% CO<sub>2</sub> in a humidified incubator.

A human fetal osteoblast cell line, hFOB 1.19 (ATCC, CRL11372), established by Harris et al. [38], was grown in a 1:1 mixture of Ham's F12 Medium and Dulbecco's Modified Eagle's Medium with 2.5 mM L-glutamine (without phenol red) (Gibco, Life Technologies, Paisley, UK) supplemented with 10% (v/v) FBS and 0.3 mg/mL geneticin (G418, Serva Electrophoresis GmbH, Heidelberg, Deutschland). Cells were maintained at 34°C under 5% CO<sub>2</sub> in a humidified incubator.

**2.4. Cell Viability and Proliferation.** Cell proliferation after 48 hours from plating was assessed by MTT viability and proliferation assay (ScienCellTM Research Laboratories, Carlsbad, CA, USA) according to the manufacturer's instruction. This assay is based on the conversion of pale yellow tetrazolium MTT [3-(4,5-dimethylthiazol-2-yl)-2,5-diphenyltetrazolium bromide] to purple formazan crystals, which can be solubilised and then spectrophotometrically quantified.

The samples of implants were placed into a 96-well plate (TPP, St. Louis, MO, USA). Cells harvested with trypsin solution from Petri dishes were resuspended in culture medium and seeded at a density of approximately 500,000 cells/mL onto the top of the discs of nanostructured titanium

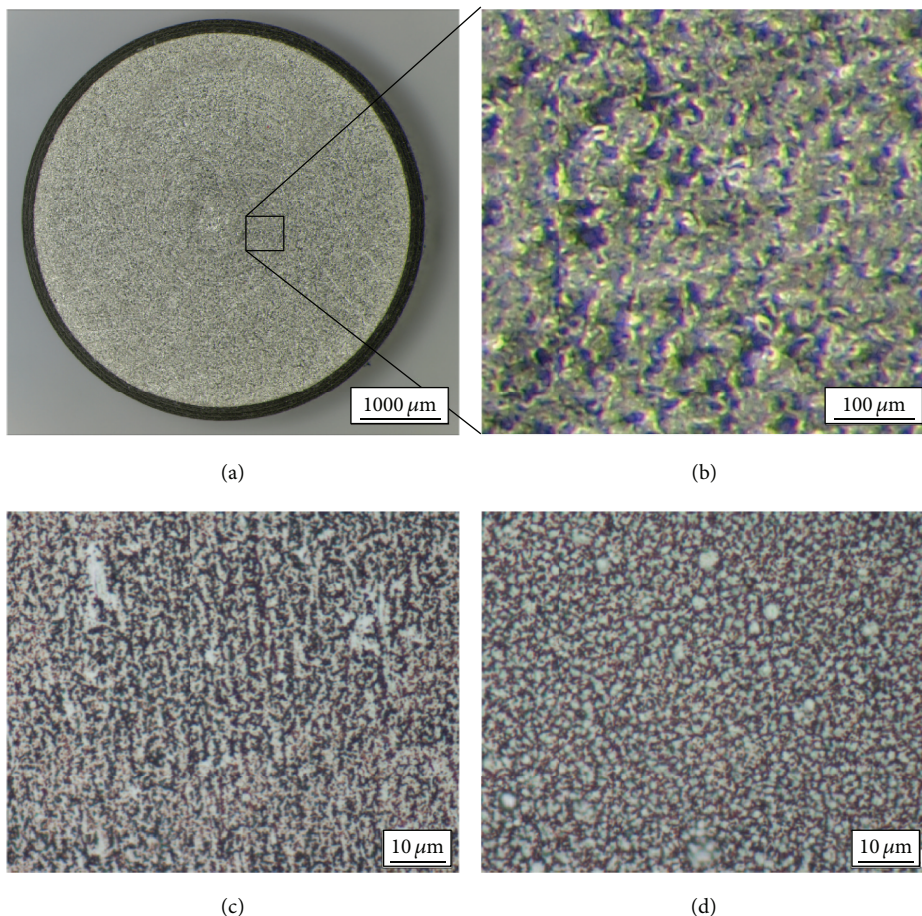


FIGURE 1: Photographs illustrating nanostructured titanium samples. (a) Macroscopic image; (b) details of the surface; (c) SEM images of longitudinal section; (d) SEM images of transversal cross-section.

in 20  $\mu\text{L}$  volume. As positive control, cells grown directly on the 96-well tissue culture plate were used.

After 48-hour incubation, cells were washed with phosphate-buffered saline (PBS) and incubated with 10  $\mu\text{L}$  MTT (25 mg/mL) solution at 37°C. After 4 hours, 100  $\mu\text{L}$  of MTT solubilisation buffer (equal to the volume of original culture medium) was added to each well and the insoluble formazan formed was dissolved by pipetting up and down. The absorbance was measured at 570 nm (spectrophotometer Nano Drop 1000, Thermo Fisher Scientific, Waltham, MA, USA), subtracting the background absorbance determined at 690 nm.

### 2.5. Fluorescent Microscopy

**2.5.1. Cells Staining.** Cultured cells were stained with CellTracker Green 5-chloromethylfluorescein diacetate (CMFDA) (Molecular Probes, Inc., Eugene, Oregon, USA) according to the manufacturer's instruction. Briefly, cells were properly washed with PBS and incubated with 4  $\mu\text{M}$  CMFDA working solution for 30 min at 37°C. Then, the dye working solution was replaced with fresh, prewarmed medium and the cells were incubated for another 30 minutes at 37°C. Stained cells were analysed using an Olympus IX 70

fluorescent microscope equipped with Cell R system at 40x, 100x, and 400x magnification.

The initial cell attachment and the spreading of the cells on the substrate with different grain size were examined after 6 h and 24 h, respectively. The area occupied by the cells was assessed by analysis of gained images by the programme ImageJ (W. S. Rasband, U. S. National Institutes of Health, Bethesda, Maryland, USA).

**2.5.2. Immunocytochemistry.** The samples of implants were placed into a 24-well plate. Five hundred cells were seeded onto the top of the discs of nanostructured titanium cells and incubated for 2 or 48 hours. Fixation was performed by 3% formaldehyde in PBS for 15 min at 37°C followed by three rinses with PBS. Permeabilisation was carried out by incubation with 0.1% triton X-100 solution in PBS for 10 min at room temperature. Blocking with 2% normal goat serum (Milipore, Billerica, MA, USA) followed for 1 h at 4°C. Each sample was double stained. Indirect immunofluorescence staining was done with a mouse monoclonal antivinculin antibody HVIN-1 diluted in PBS (1:100) and goat  $\alpha$ -mouse Atto488 conjugated secondary antibody. For actin staining, Phalloidin-Tetramethylrhodamine B isothiocyanate (TRITC) was added into the solution of secondary antibody in

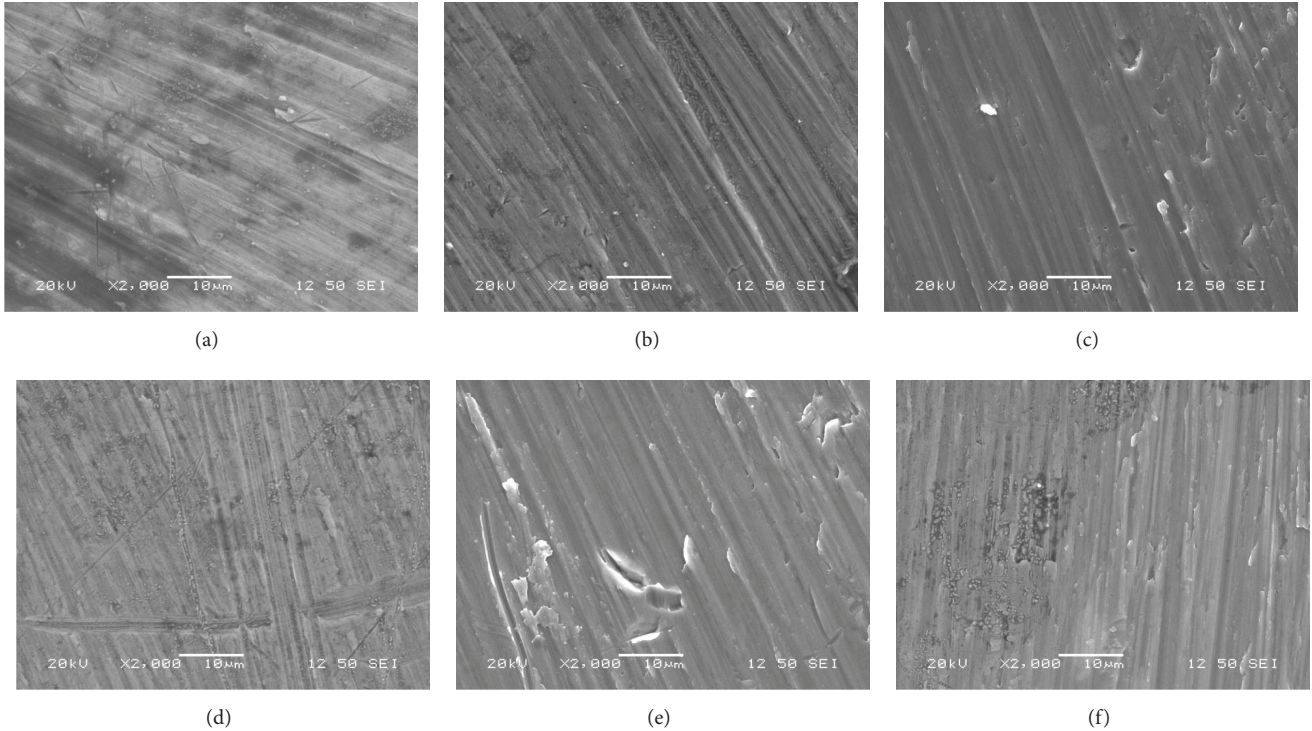


FIGURE 2: SEM photographs of the sample surfaces with different grain sizes and sections. (a, b, c) SEM images of longitudinal section with grain sizes of 160, 280, and 2400 nm, respectively; (d, e, f) SEM images of transversal cross-section with grain sizes 160, 280, and 2400 nm, respectively.

PBS (0.75 Atto488 : 1.5 TRITC : 100 PBS) (Sigma-Aldrich, St. Louis, MO, USA). Incubation with primary antibody was overnight. The second incubation was 2 hours at room temperature in the dark. Samples were analysed using an Olympus IX 70 fluorescent microscope equipped with a Cell R system at 40x, 100x, and 400x magnification.

**2.6. Statistical Analysis.** Microscopic analysis was carried out two times at a minimum, using two samples per group. In case of MTT assay, two independent experiments with quadruplicate measurements were performed. Cell viability was compared by analysis of variance (ANOVA). If ANOVA indicated a significant difference ( $P < 0.05$ ) statistical comparisons were computed by two-tailed unpaired *t*-test with the value of significance  $P < 0.05$ . Statistical analysis was performed using the SigmaPlot 12.5 software (Systat Software Inc., San Jose, California, USA).

### 3. Results

**3.1. Sample Characterization.** Sample characterization was performed by SEM. Figure 2 shows SEM images of the titanium sample surfaces.

The surface roughness quantified by arithmetical mean roughness  $R_a$  and ten-point mean roughness  $R_z$  of each sample is shown in Figure 3. Values of  $R_a$  were between 0.3 and 0.6  $\mu\text{m}$  and  $R_z$  between 1.5 and 3.0  $\mu\text{m}$ . We did not

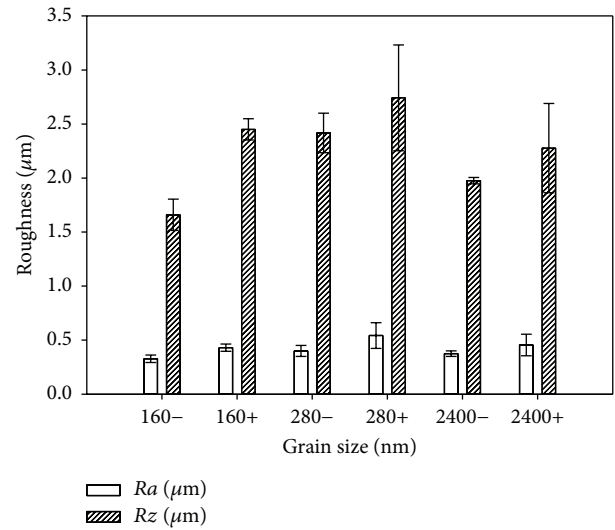


FIGURE 3: The surface roughness expressed by arithmetical mean roughness  $R_a$  and ten-point mean roughness  $R_z$ . The standard errors were calculated from three independent measurements. Error bars indicate means  $\pm$  standard deviations.

find any significant differences in surface roughness (for both parameters  $R_a$  and  $R_z$ ) among studied materials ( $P = 0.1097$  and  $P = 0.0623$ , resp.).

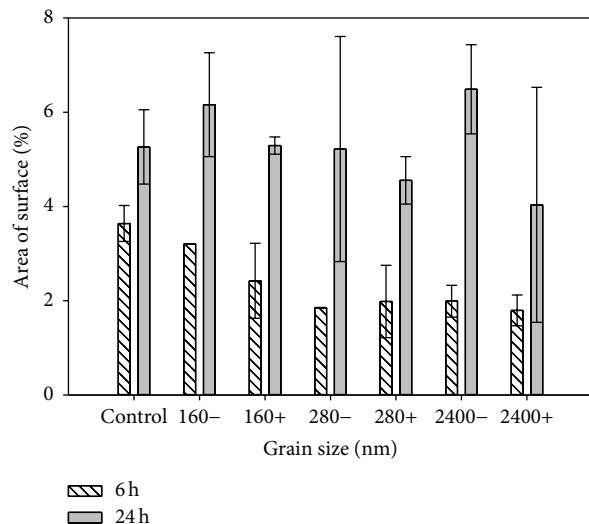


FIGURE 4: The area of surface (percentage) of six studied titanium materials with different grain sizes and sections occupied by human fibroblasts HFL1 at 6 h and 24 h after plating. Results from two distinct experiments on the basis of duplicate determination were combined. Error bars indicate means  $\pm$  standard deviations.

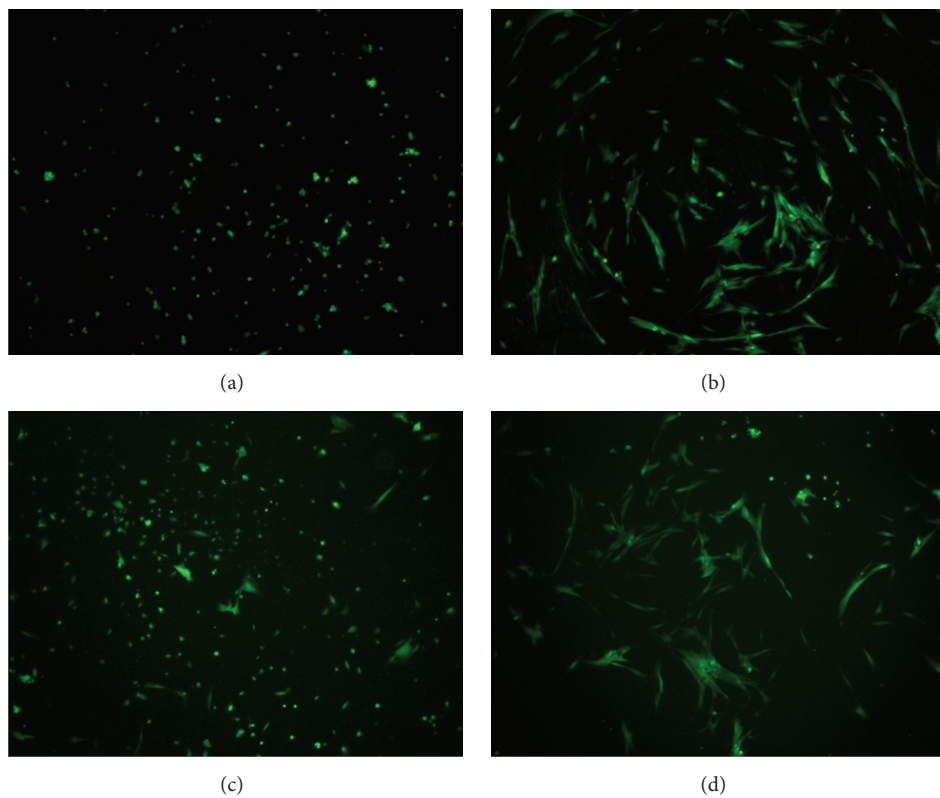


FIGURE 5: Fluorescence photographs of human fibroblasts HFL1 on tested titanium material (a, b) as well as control (c, d) at 6 h (a, c) and 24 h (b, d) after plating, 40x magnification.

### 3.2. Cell Viability and Proliferation

**3.2.1. Cell Adherence and Spreading.** The initial cell attachment within the first 6 hours was significantly slower on titanium materials with grain size 2400 (– and +) nm and 280 (– and +) nm, when compared with control (tissue

culture plate) ( $P = 0.0043$ ) (Figures 4, 5(a), and 5(c)). The cells adhered to the surface with 160 (– and +) nm grains as well as to control plate. The area occupied by fibroblasts on all studied materials reached very similar values as the control at 24 hours of cultivation (Figures 4, 5(b), and 5(d)). We also analysed differences between particular materials.

The occupied area after 6 hours was significantly higher on material 160– in contrast to 280– and both types of 2400 (– and +) ( $P < 0.0001$ ;  $P = 0.0170$ ;  $P = 0.0259$ ; resp.).

Microscopic observation revealed that after 6 h, fibroblasts presented a mainly rounded morphology (Figures 5(a) and 5(c)). After 24 h the cells elongated and presented a mainly spindle-like structure. On the tissue culture plastic, we did not see any specific orientation (Figure 5(d)). However, on material samples the cells were aligned along concentric grooves (Figures 1(b) and 5(b)).

**3.2.2. MTT Assay.** The viability of two cell lines (hFOB 1.19, HFL1) was estimated by MTT assay (Figure 6). The viability of fibroblasts growing on materials 160–, 280+, and 2400+ was significantly lower than on control plates ( $P = 0.026$ ). The osteoblast viability was lower, when growing on all types of studied titanium materials with the exception of 160+ material in comparison with the control ( $P < 0.0001$ ).

The medians of viability of the cells (% of positive control) are shown in Table 1. We found higher viability of osteoblasts comparing materials 280– with 160+ and 2400+ with 160+ ( $P = 0.0162$ ,  $P = 0.0372$ ; resp.). The comparison of other pairs of materials did not exhibit any significant differences. On the other hand, material 160+ was a significantly better substrate for culturing osteoblasts than all other studied materials ( $P = 0.0072$ ).

**3.3. Immunocytochemistry.** In order to compare morphology of the cytoskeleton, fibroblastic cells grown on the six different titanium materials underwent actin labelling with TRITC conjugated phalloidin and vinculin labelling with goat  $\alpha$ -mouse Atto488 conjugated secondary antibody for mouse monoclonal anti-human vinculin antibody HVIN-1 (Figure 7).

Two hours after seeding, cytoskeleton analysis showed that cells presented a round shape and were not yet spread properly on the surfaces. On all tested materials, at this point in time, focal contacts could be seen as positive spots localised at the cellular edge.

After 48 h, the cytoskeleton analysis mainly showed cells with an elongated bipolar morphology. On all tested surfaces, vinculin-positive focal contacts were present homogeneously on the whole cell surface, with a slightly higher density at the cell periphery, at the ends of F-actin filaments. These data denote that the adhesion phase occurred on all tested materials.

## 4. Discussion

In our work we examined how grain size of nanostructured titanium material influences the behaviour of fibroblastic as well as osteoblastic cells grown on its surface.

The grain size was shown to be an important factor that influenced not only the strength of material but also its interactions with cells. Kim et al. proved that the ultrafine grain titanium prepared by the ECAP method had better biocompatibility concerning wettability, cell adhesion, and proliferation of mouse fibroblasts [39]. Our results did not

TABLE 1: Medians of viability of two cell lines (hFOB 1.19, HFL1) estimated by MTT assay expressed as % of positive control.

Material	Cross-section			Longitudinal section		
	160–	280–	2400–	160+	280+	2400+
hFOB 1.19	72.2	62.2	68.5	91.5	62.3	62.3
HFL1	68.1	71.4	77.5	77.8	71.5	73.4

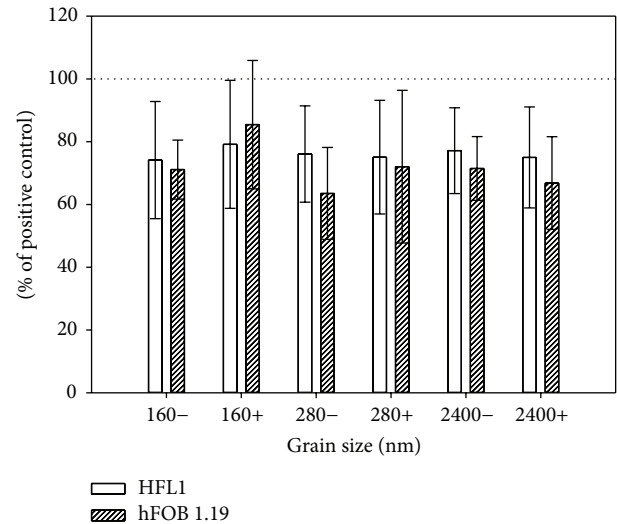


FIGURE 6: Comparison of the viability assessed by MTT assay of human fibroblasts HFL1 and human fetal osteoblast cell line, hFOB 1.19 grown on six studied titanium materials with different grain sizes. The standard errors were calculated from a combination of two independent experiments with quadruplicate measurements. Data expressed as % of positive control. Error bars indicate means  $\pm$  standard deviations.

clearly prove that grain size has a distinct impact on viability or proliferation of used fibroblast model (HFL1). The only differences we saw were related to the initial phase of attachment, but until 24 hours after seeding, differences almost disappear. We saw faster cell attachment on material with the smallest grain size in examination.

The metabolic activity, assessed by MTT test, of the cells grown on 160–, 280+, and 2400+ titanium was significantly decreased against control. However, the tested materials did not differ among each other, which indicated that all tested materials were cytocompatible. This is in line with the numerous studies demonstrating the biocompatible character of titanium as a substrate for cell culturing [40–43].

The usage of a second cell model (hFOB 1.19) revealed that one of the tested materials seems to be as good as control with respect to metabolic activity of the osteoblasts cultured on its surface. It was the material with the smallest grain size that seemed to be consistent with the studies that detected that the smaller the grain size, the better the viability [44–46]. Other studied materials were significantly worse than control and 160+. Interestingly, this result was reached only for one of two materials with one certain grain size. This observation indicated that two different sections differ in the viability of cells grown on its surface, which is in agreement with

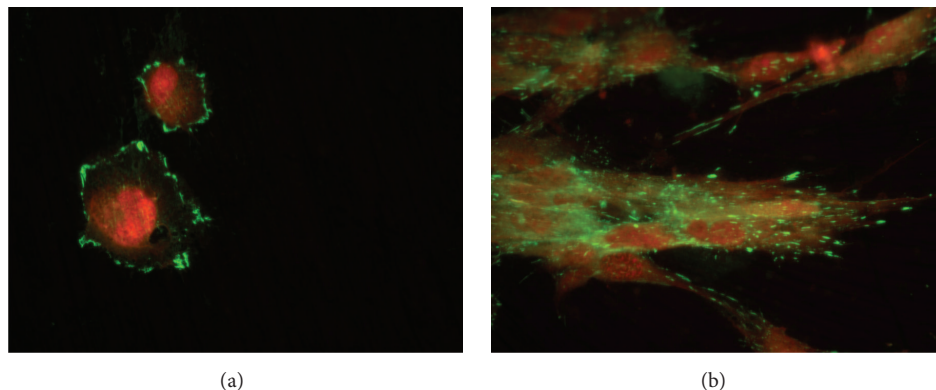


FIGURE 7: Visualisation of focal adhesion and cytoskeleton of human fibroblasts HFL1 on tested titanium material after 2 h (a) and 48 h (b) of seeding. Actin filament (red), vinculin (green), 400x magnification.

the study of Hoseini et al., who conclude that crystallographic texture, rather than grain size, plays a principal role in the surface biocompatibility [47].

It is well established that the proteins of extracellular matrix, membrane receptors, and cytoskeletal proteins are responsible for cell-substrate interactions. That is why we decided to analyse two important cytoskeletal proteins actin and vinculin by immunocytochemical staining. Actin is a critical player in many cellular functions, such as cell motility and the maintenance of cell shape and polarity [48]. Vinculin is a cytoplasmic actin-binding protein enriched in focal adhesions and adherens junctions required for strong cell adhesion [49]. As early as 2 h after seeding, the cells adhered and began to spread (Figure 7(a)). The cells displayed well-spreading morphology with many vinculin spots after 24 h (Figure 7(b)). This observation proved that the adhesion phase occurred on all tested materials.

We also intend to examine differences between two used cell models. Fibroblasts represent soft tissue and osteoblast hard tissue, and the dental implant needs to be in contact with both. We did not record significant differences in viability among tested materials plating with fibroblast cells. When we used osteoblasts as a cell model, we recorded that material with a grain size 160 nm with longitudinal section seemed to be as good as a conventional culture plate with respect to cell viability and proliferation. Therefore, this material could be recommended for a detailed study of cell behaviour *in vitro* as well as *in vivo*.

## 5. Conclusions

The aim of this study was to evaluate if any of the six studied materials is better than others with respect to biocompatibility and cell proliferation. Similar cellular behaviour was observed on all studied biomaterials. There were differences related to the initial phase of attachment, but not in proliferation. Furthermore, the results reported in this paper indicate that osteoblasts grow on material with a grain size of 160 nm with longitudinal section as well as on a conventional culture plate, whereas, for other studied materials, we observed

decreased viability. This material could be recommended for further evaluation with respect to osseointegration *in vivo*.

## Conflict of Interests

The authors declare that there is no conflict of interests regarding the publication of this paper.

## Acknowledgment

This study was supported by the National Sustainability Program I (NPU I) Nr. LO1503 provided by the Ministry of Education Youth and Sports of the Czech Republic.

## References

- [1] N. G. Durmus and T. J. Webster, "Nanostructured titanium: the ideal material for improving orthopedic implant efficacy?" *Nanomedicine*, vol. 7, no. 6, pp. 791–793, 2012.
- [2] N. K. Tolochko, V. V. Savich, T. Laoui et al., "Dental root implants produced by the combined selective laser sintering/melting of titanium powders," *Proceedings of the Institution of Mechanical Engineers, Part L: Journal of Materials: Design and Applications*, vol. 216, no. 4, pp. 267–270, 2002.
- [3] T. Hayashi, K. Maekawa, M. Tamura, and K. Hanyu, "Selective laser sintering method using titanium powder sheet toward fabrication of porous bone substitutes," *JSME International Journal Series A Solid Mechanics and Material Engineering*, vol. 48, no. 4, pp. 369–375, 2005.
- [4] H. Nakamura, L. Saruwatari, H. Aita, K. Takeuchi, and T. Ogawa, "Molecular and biomechanical characterization of mineralized tissue by dental pulp cells on titanium," *Journal of Dental Research*, vol. 84, no. 6, pp. 515–520, 2005.
- [5] Á. Joób-Fancsaly, T. Divinyi, Á. Fazekas, C. Daroczi, A. Karacs, and G. Pető, "Pulsed laser-induced micro- and nanosized morphology and composition of titanium dental implants," *Smart Materials and Structures*, vol. 11, no. 5, pp. 819–824, 2002.
- [6] H.-M. Kim, H. Takadama, F. Miyaji, T. Kokubo, S. Nishiguchi, and T. Nakamura, "Formation of bioactive functionally graded structure on Ti-6Al-4V alloy by chemical surface treatment," *Journal of Materials Science: Materials in Medicine*, vol. 11, no. 9, pp. 555–559, 2000.

- [7] P. Fischer, V. Romano, H. P. Weber, N. P. Karapatis, E. Boillat, and R. Glardon, "Sintering of commercially pure titanium powder with a Nd:YAG laser source," *Acta Materialia*, vol. 51, no. 6, pp. 1651–1662, 2003.
- [8] B. Engel and D. L. Bourell, "Titanium alloy powder preparation for selective laser sintering," *Rapid Prototyping Journal*, vol. 6, no. 2, pp. 97–106, 2000.
- [9] S. Das, M. Wohlert, J. J. Beaman, and D. L. Bourell, "Processing of titanium net shapes by SLS/HIP" *Materials & Design*, vol. 20, no. 2-3, pp. 115–121, 1999.
- [10] I. V. Shishkovskii, Y. G. Morozov, S. V. Fokeev, and L. T. Volova, "Laser synthesis and comparative testing of a three-dimensional porous matrix of titanium and titanium nickelide as a repository for stem cells," *Powder Metallurgy and Metal Ceramics*, vol. 50, no. 9-10, pp. 606–618, 2012.
- [11] J. Petruzelka, L. Dluhos, D. Hrusak, and J. Sochova, "Nanotextured titan—a new material for dental implants," *Česká Stomatologie*, vol. 106, no. 3, pp. 72–77, 2006.
- [12] J. Vanek, "Klasifikace materiálu," in *Dentalní Implantologie*, A. Simunek, Ed., pp. 29–33, Nucleus HK, Hradec Kralove, Czech Republic, 2nd edition, 2008.
- [13] C. A. St Pierre, M. Chan, Y. Iwakura, D. C. Ayers, E. A. Kurt-Jones, and R. W. Finberg, "Periprosthetic osteolysis: characterizing the innate immune response to titanium wear-particles," *Journal of Orthopaedic Research*, vol. 28, no. 11, pp. 1418–1424, 2010.
- [14] M. Lai, K. Cai, Y. Hu, X. Yang, and Q. Liu, "Regulation of the behaviors of mesenchymal stem cells by surface nanostructured titanium," *Colloids and Surfaces B: Biointerfaces*, vol. 97, pp. 211–220, 2012.
- [15] R. Z. Valiev, O. A. Kaibyshev, R. I. Kuznetsov, R. S. Musalimov, and N. K. Tsenev, "The low-temperature superplasticity of metallic materials," *Doklady Akademii Nauk SSSR (Proceedings of the Academy of Sciences of the USSR)*, vol. 301, no. 4, pp. 864–866, 1988.
- [16] R. Z. Valiev, N. A. Krasilnikov, and N. K. Tsenev, "Plastic deformation of alloys with submicron-grained structure," *Materials Science and Engineering A*, vol. 137, pp. 35–40, 1991.
- [17] R. Z. Valiev, R. K. Islamgaliev, and I. V. Alexandrov, "Bulk nanostructured materials from severe plastic deformation," *Progress in Materials Science*, vol. 45, no. 2, pp. 103–189, 2000.
- [18] R. Z. Valiev, I. P. Semenova, V. V. Latysh et al., "Nanostructured titanium for biomedical applications," *Advanced Engineering Materials*, vol. 10, no. 8, pp. B15–B17, 2008.
- [19] D. Kopecka, A. Simunek, and R. Slezák, "Nanomaterials in dentistry—state of the art," *Praktické Zubní Lékařství*, vol. 57, no. 4, pp. 59–62, 2009.
- [20] D. Hrusak, M. Zemko, L. Dluhos, and L. Kraus, "Usage of nanostructured titanium for endosteal implants," in *Proceedings of the 1st Conference with International Participation Nanocon, SIB3*, Roznov pod Radhostem, Czech Republic, October 2009.
- [21] T. J. Webster, R. W. Siegel, and R. Bizios, "Osteoblast adhesion on nanophase ceramics," *Biomaterials*, vol. 20, no. 13, pp. 1221–1227, 1999.
- [22] N. Tran and T. J. Webster, "Nanotechnology for bone materials," *Wiley Interdisciplinary Reviews: Nanomedicine and Nanobiotechnology*, vol. 1, no. 3, pp. 336–351, 2009.
- [23] G. Balasundaram and T. J. Webster, "A perspective on nanophase materials for orthopedic implant applications," *Journal of Materials Chemistry*, vol. 16, no. 38, pp. 3737–3745, 2006.
- [24] F. Varíola, F. Vetrone, L. Richert et al., "Improving biocompatibility of implantable metals by nanoscale modification of surfaces: an overview of strategies, fabrication methods, and challenges," *Small*, vol. 5, no. 9, pp. 996–1006, 2009.
- [25] M. J. Dalby, N. Gadegaard, R. Tare et al., "The control of human mesenchymal cell differentiation using nanoscale symmetry and disorder," *Nature Materials*, vol. 6, no. 12, pp. 997–1003, 2007.
- [26] S. Oh, K. S. Brammer, Y. S. J. Li et al., "Stem cell fate dictated solely by altered nanotube dimension," *Proceedings of the National Academy of Sciences of the United States of America*, vol. 106, no. 7, pp. 2130–2135, 2009.
- [27] P. Bertoncini, S. Le Chevalier, S. Lavenus, P. Layrolle, and G. Louarn, "Early adhesion of human mesenchymal stem cells on TiO<sub>2</sub> surfaces studied by single-cell force spectroscopy measurements," *Journal of Molecular Recognition*, vol. 25, no. 5, pp. 262–269, 2012.
- [28] S. M. Sporer and W. G. Paprosky, "Biologic fixation and bone ingrowth," *Orthopedic Clinics of North America*, vol. 36, no. 1, pp. 105–111, 2005.
- [29] D. Buser, H. P. Weber, K. Donath, J. P. Fiorellini, D. W. Paquette, and R. C. Williams, "Soft tissue reactions to non-submerged unloaded titanium implants in beagle dogs," *Journal of Periodontology*, vol. 63, no. 3, pp. 225–235, 1992.
- [30] M. A. Listgarten, N. P. Lang, H. E. Schroeder, and A. Schroeder, "Periodontal tissues and their counterparts around endosseous implants," *Clinical Oral Implants Research*, vol. 2, no. 1, pp. 1–19, 1991.
- [31] E. Eisenbarth, J. Meyle, W. Nachtigall, and J. Breme, "Influence of the surface structure of titanium materials on the adhesion of fibroblasts," *Biomaterials*, vol. 17, no. 14, pp. 1399–1403, 1996.
- [32] F. H. Jones, "Teeth and bones: applications of surface science to dental materials and related biomaterials," *Surface Science Reports*, vol. 42, no. 3–5, pp. 75–205, 2001.
- [33] B. Größner-Schreiber, M. Herzog, J. Hedderich, A. Dück, M. Hannig, and M. Griepentrog, "Focal adhesion contact formation by fibroblasts cultured on surface-modified dental implants: an *in vitro* study," *Clinical Oral Implants Research*, vol. 17, no. 6, pp. 736–745, 2006.
- [34] W. Baschong and J. T. Lambrecht, "Influence of the implant surface on the early phase of osteogenesis in vitro," *Schweizer Monatsschrift für Zahnmedizin*, vol. 114, no. 8, pp. 792–799, 2004.
- [35] C. Jin, L.-F. Ren, H.-Z. Ding, G.-S. Shi, H.-S. Lin, and F. Zhang, "Enhanced attachment, proliferation, and differentiation of human gingival fibroblasts on titanium surface modified with biomolecules," *Journal of Biomedical Materials Research Part B: Applied Biomaterials*, vol. 100, no. 8, pp. 2167–2177, 2012.
- [36] L. Meirelles, A. Arvidsson, T. Albrektsson, and A. Wennerberg, "Increased bone formation to unstable nano rough titanium implants," *Clinical Oral Implants Research*, vol. 18, no. 3, pp. 326–332, 2007.
- [37] M. S. Lord, M. Foss, and F. Besenbacher, "Influence of nanoscale surface topography on protein adsorption and cellular response," *Nano Today*, vol. 5, no. 1, pp. 66–78, 2010.
- [38] S. A. Harris, R. J. Enger, B. L. Riggs, and T. C. Spelsberg, "Development and characterization of a conditionally immortalized human fetal osteoblastic cell line," *Journal of Bone and Mineral Research*, vol. 10, no. 2, pp. 178–186, 1995.
- [39] T. N. Kim, A. Balakrishnan, B. C. Lee et al., "In vitro biocompatibility of equal channel angular processed (ECAP) titanium," *Biomedical Materials*, vol. 2, no. 3, pp. S117–S120, 2007.

- [40] S. G. Steinemann, “Titanium—the material of choice?” *Peri-odontology* 2000, vol. 17, no. 1, pp. 7–21, 1998.
- [41] M. Schuier, D. Trentin, M. Textor, and S. G. P. Tosatti, “Biomedical interfaces: titanium surface technology for implants and cell carriers,” *Nanomedicine*, vol. 1, no. 4, pp. 449–463, 2006.
- [42] L. Le Guehennec, M.-A. Lopez-Heredia, B. Enkel, P. Weiss, Y. Amouriq, and P. Layrolle, “Osteoblastic cell behaviour on different titanium implant surfaces,” *Acta Biomaterialia*, vol. 4, no. 3, pp. 535–543, 2008.
- [43] Y. Estrin, H.-E. Kim, R. Lapovok, H. P. Ng, and J.-H. Jo, “Mechanical strength and biocompatibility of ultrafine-grained commercial purity titanium,” *BioMed Research International*, vol. 2013, Article ID 914764, 6 pages, 2013.
- [44] T. N. Kim, A. Balakrishnan, B. C. Lee et al., “In vitro fibroblast response to ultra fine grained titanium produced by a severe plastic deformation process,” *Journal of Materials Science: Materials in Medicine*, vol. 19, no. 2, pp. 553–557, 2008.
- [45] Y. Estrin, E. P. Ivanova, A. Michalska, V. K. Truong, R. Lapovok, and R. Boyd, “Accelerated stem cell attachment to ultrafine grained titanium,” *Acta Biomaterialia*, vol. 7, no. 2, pp. 900–906, 2011.
- [46] A. Farzin, M. Ahmadian, and M. H. Fathi, “Comparative evaluation of biocompatibility of dense nanostructured and microstructured Hydroxyapatite/Titania composites,” *Materials Science and Engineering C*, vol. 33, no. 4, pp. 2251–2257, 2013.
- [47] M. Hoseini, P. Bocher, A. Shahryari, F. Azari, J. A. Szpunar, and H. Vali, “On the importance of crystallographic texture in the biocompatibility of titanium based substrate,” *Journal of Biomedical Materials Research Part A*, vol. 102, no. 10, pp. 3631–3638, 2014.
- [48] R. Dominguez and K. C. Holmes, “Actin structure and function,” *Annual Review of Biophysics*, vol. 40, no. 1, pp. 169–186, 2011.
- [49] K. A. DeMali, “Vinculin—a dynamic regulator of cell adhesion,” *Trends in Biochemical Sciences*, vol. 29, no. 11, pp. 565–567, 2004.

## Review Article

# 3D Nanoprinting Technologies for Tissue Engineering Applications

Jin Woo Lee

*Department of Molecular Medicine, School of Medicine, Gachon University, Songdo-Dong, Yeonsu-gu, Incheon 406-840, Republic of Korea*

Correspondence should be addressed to Jin Woo Lee; [jwlee@gachon.ac.kr](mailto:jwlee@gachon.ac.kr)

Received 5 August 2015; Revised 21 October 2015; Accepted 22 October 2015

Academic Editor: Ramaswamy Narayanan

Copyright © 2015 Jin Woo Lee. This is an open access article distributed under the Creative Commons Attribution License, which permits unrestricted use, distribution, and reproduction in any medium, provided the original work is properly cited.

Tissue engineering recovers an original function of tissue by replacing the damaged part with a new tissue or organ regenerated using various engineering technologies. This technology uses a scaffold to support three-dimensional (3D) tissue formation. Conventional scaffold fabrication methods do not control the architecture, pore shape, porosity, or interconnectivity of the scaffold, so it has limited ability to stimulate cell growth and to generate new tissue. 3D printing technologies may overcome these disadvantages of traditional fabrication methods. These technologies use computers to assist in design and fabrication, so the 3D scaffolds can be fabricated as designed and standardized. Particularly, because nanofabrication technology based on two-photon absorption (2PA) and on controlled electrospinning can generate structures with submicron resolution, these methods have been evaluated in various areas of tissue engineering. Recent combinations of 3D nanoprinting technologies with methods from molecular biology and cell dynamics have suggested new possibilities for improved tissue regeneration. If the interaction between cells and scaffold system with biomolecules can be understood and controlled and if an optimal 3D environment for tissue regeneration can be realized, 3D nanoprinting will become an important tool in tissue engineering.

## 1. Introduction

Tissue engineering recovers an original function of tissue by replacing the damaged part with a new tissue or organ that has been regenerated using various engineering technologies. Tissue engineering is composed of three essential components: cell, biomolecules, and scaffold. Scaffolds supply an artificial structure that can support three-dimensional (3D) tissue formation. Cells seeded into the scaffold proliferate and differentiate, and biomolecules in the culture medium accelerate these processes. When the three components are suitably combined, a tissue is regenerated successfully. To achieve the tissue regeneration, scaffolds should be biocompatible and must have adequate pore size, high interconnectivity, and appropriate mechanical properties. Biodegradability should also be considered, because scaffolds should preferably be absorbed by the body, thereby eliminating the need for surgical removal.

Initially, most scaffolds were fabricated by traditional methods [1–13] such as gas foaming, freeze-drying,

particulate leaching, phase separation/inversion, and fiber bonding. However, because those methods do not control the architecture, pore shape, porosity, or interconnectivity of the scaffold, they did not adequately stimulate cell growth and tissue generation.

3D printing technology using computer-aided design (CAD) and computer-aided manufacturing (CAM) may overcome these disadvantages. Because these methods use computer software to design and fabricate the scaffolds, their internal architectures such as the pore size, pore shape, porosity, and the interconnectivity of the scaffolds can be freely controlled. In addition, computer-aided 3D printing can produce reproducible constructs, so it enables standardization of scaffolds. This standardization eliminates variability of the inner architecture among scaffolds, so it improves the repeatability and reliability of experiments. These technologies can also fabricate customized scaffolds for patients.

Various 3D printing technologies [14–28] including stereolithography, deposition modeling, inkjet printing, selective laser sintering, and electrospinning technology have been

developed. Those technologies have been widely used in studies of regeneration of tissues such as bone, cartilage, ligament, muscle, skin, and neurons and of organs such as trachea, liver, kidney, and heart. 2PP and electrospinning can fabricate constructs to submicron precision. Therefore, this review will provide the present condition of scaffold fabrication using these 3D printing technologies.

## 2. 3D Nanoprinting for Tissue Engineering

**2.1. Two-Photon Absorption (2PA) Based 3D Printing.** Stereolithography (SL) was developed independently by Kodama [35] and Nakai and Marutani [36] in the 1980s. 3D Systems Inc. sold a commercialized SL system for the first time. SL uses an ultraviolet (UV) laser beam to irradiate the surface of a liquid photopolymer, causing it to solidify. Many scanned UV laser lines are overlapped on the surface to solidify a specified cross-sectional area; many such cross-sectional areas are accumulated step by step to form the desired 3D shape. Microstereolithography (MSTL) uses the same fabrication mechanism as SL but uses optical components to reduce the diameter of the laser beam to a few micrometers [37]. The laser beam is passed through a beam expander and focusing lens (Figure 1(a)) and then solidifies a very small area of the liquid photopolymer surface. MSTL enables fabrication of 3D freeform structures at micrometer scales.

Two-photon polymerization (2PP) is a laser-based 3D printing technique that uses two-photon absorption (2PA) [38, 39]. 2PA can be used to induce laser-based erosion by photoreaction of an irradiated material and ablation by an intense laser. In 2PP, a laser is used to trigger a chemical reaction that causes polymerization of a photosensitive material, as in SL and MSTL. However, unlike the single-photon polymerization process of SL and MSTL, 2PP allowed electron transitions over excited energy levels for the polymerization process, when an atom absorbs two photons simultaneously (~femtosecond level) (Figure 1(b)). For instance, when a specific photoinitiator that reacts at wavelength  $\lambda = 400$  nm simultaneously absorbs two photons with  $\lambda = 800$  nm, their energies add up to equal the energy of one photon with  $\lambda = 400$  nm and thus initiate the polymerization process. Photopolymerization that is triggered by nonlinear excitation happens at the focal point, but other regions are not affected by the laser energy. This phenomenon has the potential to reduce solidification resolution to below the diffraction limit of the applied light. In addition, the movement of the laser focal point and solidification inside the liquid photopolymer guarantee the fabrication of a 3D product. Therefore, 2PP currently has the highest resolution of all 3D printing techniques.

By combining CAD and CAM, the inner architecture of the structure can be precisely controlled. As a result of these features, 2PP offers great potential for the fabrication of appropriate scaffolds for tissue engineering. In addition, development of photodegradable polymer has enabled a two-photon erosion process, and modulation of a two-photon pulse laser has produced an ablation technique with submicron resolution.

**2.1.1. Two-Photon Polymerization Technology for Tissue Engineering.** By exploiting the high resolution of 2PP, many researchers have focused on the realization of 3D environments for cell adhesion and proliferation. Mostly, this research concentrated on methods to fabricate the 3D scaffold, which is an essential environment to regenerate damaged tissue.

Koroleva et al. [40] used a combination of 2PP and micro-molding to fabricate 3D fibrin scaffolds with tightly controllable pore sizes and interconnections. The authors used 2PP to fabricate master structures and then used two-step replication process to regenerate. The fabricated fibrin scaffolds were highly porous and well interconnected. Culture of endothelial cells in the scaffolds resulted in directed lining and spreading of cells within a replicated pore network, whereas endothelial cells encapsulated in fibrin gel blocks showed chaotic and irregular distributions. These results demonstrated that the combination of 2PP and micromolding technique can supply complex 3D structures for tissue engineering.

Koroleva et al. [41] used 2PP to produce well-defined macroscopic scaffolds for engineering of neural tissue. Their scaffolds can be replicated by soft lithography, so production speed is relatively fast. Photo-cross-linkable poly(lactic acid) (PLA) was used to produce scaffolds by 2PP and soft lithography. PLA 3D scaffolds sustained a high degree (99%) of Schwann cell purity and provided a suitable substrate to support Schwann cell adhesion. Most of the Schwann cells in the scaffolds showed alignment of actin filaments and formation of focal contacts. These photo-cross-linked PLA scaffolds successfully support the growth of primary Schwann cells.

Claeyssens et al. [29] fabricated microstructures using 2PP process and the biodegradable copolymer poly( $\epsilon$ -caprolactone-co-trimethylene carbonate)-b-poly(ethylene glycol)-b-poly( $\epsilon$ -caprolactone-co-trimethylene carbonate) with 4,4'-bis(diethylamino)benzophenone as the photoinitiator. The minimum line width of structures was  $4\ \mu\text{m}$ , and the fabricated structure showed a fully interconnected 3D shape (Figure 2). Initial cytotoxicity was not detected, and cell proliferation speed was moderate. These proliferation results demonstrated that this material can be applied to the scaffold for tissue engineering.

Correa et al. [42] used 2PP to fabricate microstructures that contained chitosan, which is a biodegradable and biocompatible polymer that has applications in blood coagulation, soft tissue, and bone regeneration. Chitosan could provide microstructures with appealing properties for medical applications. The chitosan did not react chemically with the matrix resin and therefore retains its characteristics after the fabrication process.

Kufelt et al. [43] fabricated the 3D hydrogel microenvironments with predefined geometry and porosity using 2PP and chitosan. They explored a new synthesis of water-soluble photosensitive chitosan and the fabrication of well-defined microstructures from the generated materials. To modulate the mechanical and biochemical properties of the material, chitosan was combined and cross-linked with synthetic poly(ethylene glycol) diacrylate. For a biological adaption to the *in vivo* situation, chitosan was covalently cross-linked

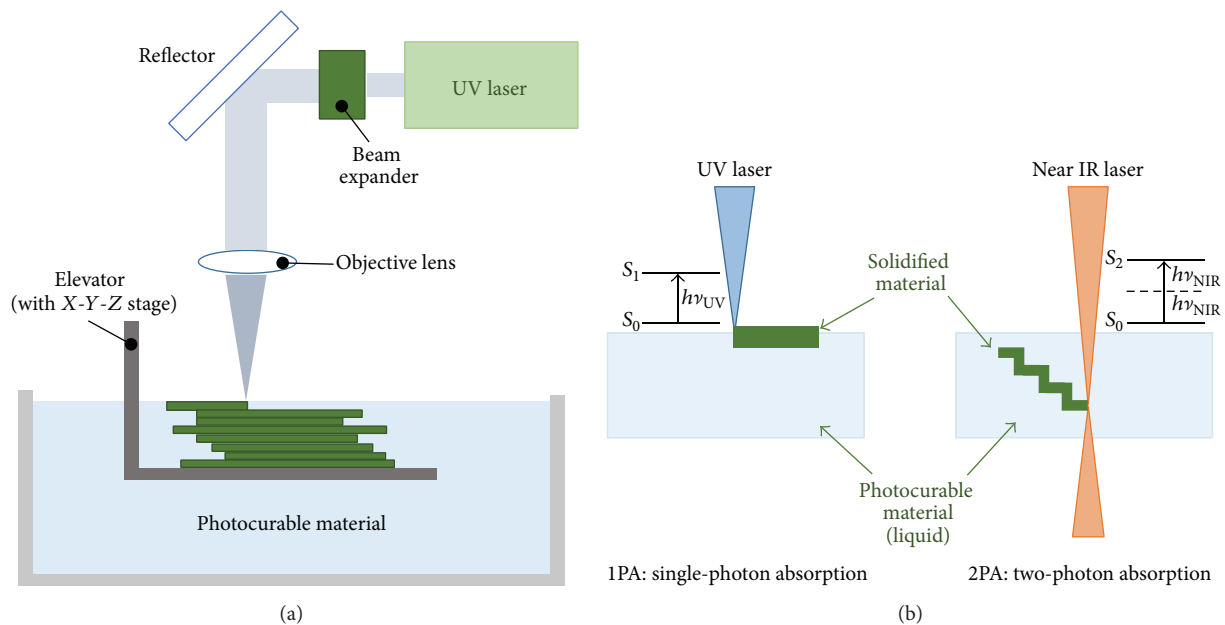


FIGURE 1: (a) Fundamental principle of MSTL technology. (b) Comparison between single-photon polymerization and two-photon polymerization.

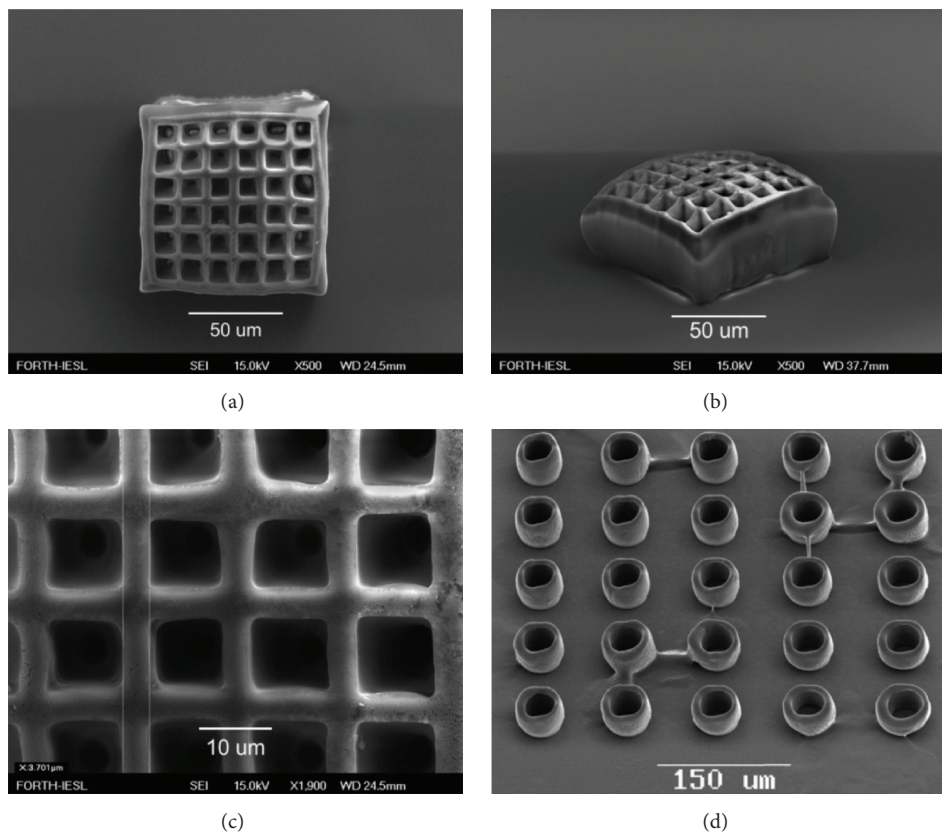


FIGURE 2: 3D structure fabricated using two-photon polymerization. (a) Top view, (b) side view, (c) detail, and (d) large cylindrical structures (figures were reproduced from [29] with permission of ACS Publications).

with a photosensitive modified vascular endothelial growth factor (VEGF). Performed *in vitro* studies revealed that modified chitosan is biocompatible and VEGF enhanced CH bioactivity. Furthermore, a 3D chitosan scaffold was successfully seeded with cells. From the study, the established chitosan showed a potential for future applications in tissue engineering.

Cha et al. [44] used 2PP to incorporate micropatterns on the scaffold. They fabricated 3D scaffolds with micropillar and microridge patterns on each layer and observed the effects of the patterns on cellular behaviors including adhesion, proliferation, and osteogenic differentiation. Preosteoblasts adhered significantly better to scaffolds with micropatterns than to a scaffold without a pattern. The expression results of osteogenic markers including ALP and Runx2 showed the superiority of scaffolds that had micropillar and microridge patterns. Thus, use of a femtosecond laser to print micropatterns on 3D scaffolds may be a useful method to encourage tissue regeneration.

Marino et al. [45] fabricated a trabecula-like structure, which was named “Osteoprint” that resembles the typical microenvironment of trabecular bone cells using two-photon polymerization process. Starting from microtomography images of the trabecular bone, they prepared several Osteoprints through two-photon polymerization and tested the behavior of SaOS-2 bone-like cells cultured on their structures. They found that Osteoprints deeply affect cellular behavior, determining an exit from the cell cycle and an enhancement of osteogenic differentiation. And they also found an upregulation of the genes involved in SaOS-2 cell maturation and an increase in hydroxyapatite production and accumulation upon SaOS-2 culture on the Osteoprints. Their finding showed the new perspectives in “bioinspired” approaches for tissue engineering and regenerative medicine.

Doraiswamy et al. [46] fabricated three-dimensional microstructured medical devices by 2PP of Ormocer organic–inorganic hybrid materials. Neuroblast-like cells and epithelial-like cells showed good viability of fabricated Ormocer. Microneedle arrays with unique geometries and Lego-like interlocking tissue engineering scaffolds were fabricated using 2PP. These results showed that 2PP can create biomedical microdevices with a larger range of sizes and shapes than can reactive ion etching, surface/bulk micromachining, injection molding, polysilicon micromolding, or other conventional microfabrication techniques.

In most biological studies, cell movement is a subject of ongoing study. Especially in cancer biology, the understanding of the cell migration is very important to estimate and forecast cancer metastasis. However, most related studies have been conducted in standard two-dimensional (2D) environments such as plastic plates coated with extracellular matrix, or glass tissue culture plates. Study of realistic cellular motion and migration requires an effective 3D biomimetic environment. Use of 2PP to fabricate such an environment with high resolution has been the subject of several studies.

Otuka et al. [47] used 2PP to fabricate microenvironment for *in situ* monitoring of cell growth and movement. They fabricated a microenvironment that was doped at specific site with ciprofloxacin (an antibiotic that is used in the treatment

of diseases caused by *E. coli*) and that included microfences that can trap bacteria. Development of *E. coli* was inhibited near sites that were doped with ciprofloxacin, and the microfence traps increased the density of *E. coli* near them. These microenvironments showed potential as a platform for drug delivery system by promoting or inhibiting the growth of bacteria.

Zhang et al. [30] used poly(ethylene glycol) diacrylate (PEDGA) biomaterial to fabricate suspended web structures that exhibit positive or negative Poisson’s ratio (NPR). The authors observed cellular responses involved in tuning Poisson’s ratio in biological scaffolds and developed high-resolution NPR webs that demonstrated biaxial behavior during expansion or contraction as one or more cells applied local forces and moved the structures. The NPR structures fostered unusual cell division, and cells migrated toward regions that were stiffer than average (Figure 3). This 2PP process demonstrated that Poisson’s ratio of photo-cross-linkable biomaterials can be tuned; this approach has potential applications in mechanobiology.

Raimondi et al. [48] applied femtosecond laser 2PP to fabricate 3D microscaffolds, or “niches,” using a hybrid organic–inorganic photoresist. They developed two niche heights, 20 and 80–100  $\mu\text{m}$ , and four lattice pore dimensions (10, 20, and 30  $\mu\text{m}$  and graded) and they prepared primary rat mesenchymal stem cells (MSCs) to study cell viability, migration, and proliferation in the niches. MSCs preferentially stayed on/in the structures once they ran into them through random migration from the surrounding flat surface, invaded those with a lattice pore dimension greater than 10  $\mu\text{m}$ , and adhered to the internal lattice while the cell nuclei acquired a roundish morphology. In the niches, the highest MSC density was found in those areas where proliferation was observed. The microgeometry inducing the highest cell density was 20  $\mu\text{m}$  high with graded pores, in which cell invasion was favored in the central region of large porosity and cell adhesion was favored in the lateral regions of high scaffold surface density. Their result showed the crucial role played by the niche 3D geometry on MSC colonization in culture.

Jeon et al. [49] also used 2PP to fabricate patterns with various height and high aspect ratios (~10) and then used them in studies of cell guidance. They seeded fibroblasts on orthogonal mesh patterns (8  $\mu\text{m}$  and 4  $\mu\text{m}$  height, 5  $\mu\text{m}$  and 5.5  $\mu\text{m}$  height, and 5  $\mu\text{m}$  and 6  $\mu\text{m}$  height) and on parallel line patterns with different heights (1.5, 0.8, and 0.5  $\mu\text{m}$ ). The seeded fibroblasts received different contact strengths depending on the wall height. A threshold of approximately 1  $\mu\text{m}$  in height influenced cell alignment both on mesh and on line patterns. This technology may be used in design of microdevices for controlling cell behavior and for investigating cell signal transduction.

Drug delivery is administration of pharmaceutical materials to achieve a therapeutic effect in living creatures. A drug delivery system (DDS) supplies a predetermined drug releasing profile which ensures an optimal absorption of the drug to improve its safety and efficacy. 3D microscale or nanoscale systems [50–55] made from various biomaterials may have applications [56–62] in DDSs, and 2PP has been evaluated as a tool for development of DDSs.

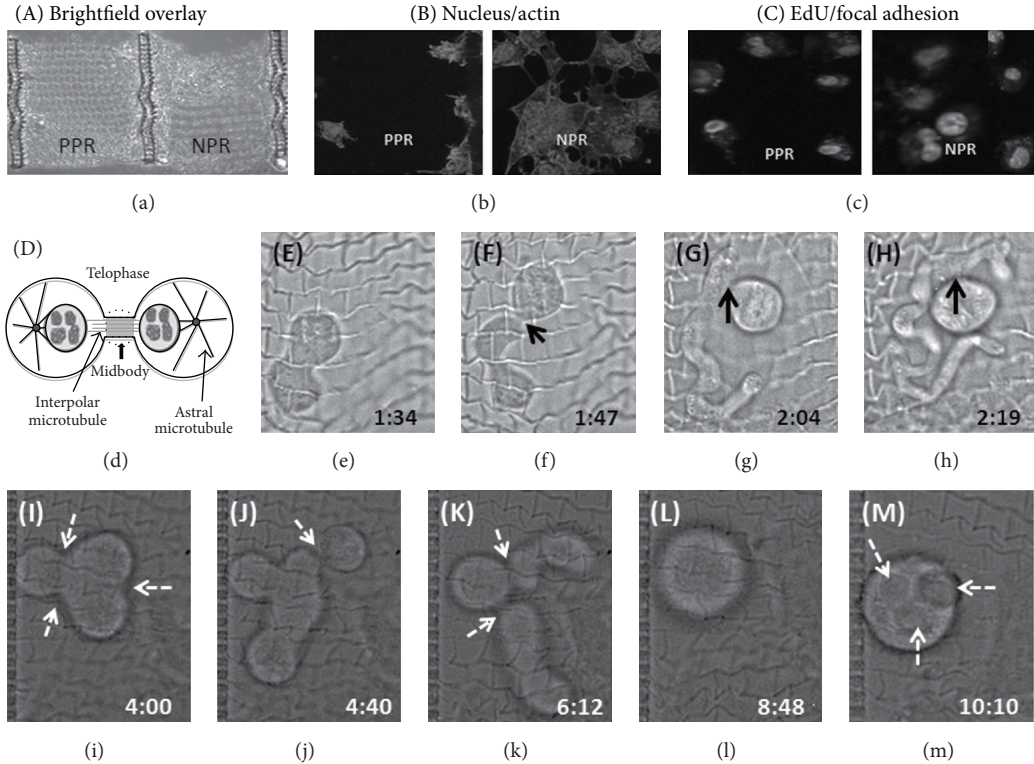


**FIGURE 3:** (a–c) Immunostaining of 10T1/2 cells for adhesion (nucleus, actin, and focal adhesions) and proliferation (EdU). (d) Schematic illustration showing cell in telophase: the cleavage furrow ingresses, compresses the midzone, and creates an intercellular bridge containing a microtubule midbody. In normal cell division, the bridge is resolved creating two daughter cells. The NPR structure induces aberrant cell-division response: (e–h) Abnormal cell division initiates and results in the formation of a long structure. Black arrow indicates persistent midbody connection. (i–m) Multiple sites of symmetric as well as asymmetric furrow formation during cell division on the NPR webs (dotted white arrows) (figures were reproduced from [30] with permission of John Wiley and Sons).

Chan et al. [63] used 2PP to deposit complex protein microstructures with submicrometer features and controllability. In bovine serum albumin (BSA) protein solution, the method produced 2D line voxels with lateral fabrication resolution of 200 nm and elliptical 3D spot voxels with dimensions of 400 nm (lateral) and 1.5  $\mu\text{m}$  (axial). The authors fabricated BSA-based micropillar arrays and used them as platforms for cell niche studies. A study using fibroblasts showed good cell attachment and growth and good expression of adhesion molecules without the need for a matrix coating. This work presented a useful method to engineer protein microstructures with submicrometer topological features to mimic the native matrix niche. These structures have applications in cell–matrix interaction studies.

Turunen et al. [64] studied using picosecond and femtosecond lasers to induce photo-cross-linking of protein microstructures. The capability of a picosecond laser (Nd:YAG) to induce protein crosslinking by a multiphoton excitation was evaluated by fabricating 2D and 3D microstructures of bovine serum albumin (BSA), biotinylated bovine serum albumin (bBSA), and avidin. The authors fabricated sub-micrometer-scale and micrometer-scale structures from several different protein compositions and photosensitizers by varying the average laser power and scanning speed and then compared the surface topography and resolution of the resulting protein

patterns to those of protein patterns fabricated using a femtosecond Ti:Sapphire laser. The study demonstrated that a low-cost Nd:YAG microlaser can be used for direct laser writing of protein microstructures.

Farsari et al. [65, 66] functionalized the surface of 3D structures fabricated using three-photon polymerization and then immobilized photosensitive biotin on the structure surface. The existence and distribution of biotin were measured using fluorescence microscopy and a surface acoustic sensor technique to detect the presence of avidin. The same research group has studied the immobilization of peptides. The methods developed by this group can be used to fabricate scaffolds for cell growth and tissue engineering.

Gittard et al. [67] fabricated microneedles with antimicrobial function for transdermal delivery of protein- and nucleic acid-based drugs. Existing microneedle-generated pores may allow microorganisms to penetrate the stratum corneum layer of the epidermis and infection. Therefore, the authors used 2PP, micromolding, and pulsed laser deposition to fabricate microneedles that had antimicrobial functionality. The authors fabricated needles from Ormocer and either coated them with silver or left them bare. The silver-coated Ormocer microneedles showed antibacterial properties but did not inhibit growth of human keratinocytes. This result showed that use of silver coating is an effective approach for

creating microneedles that have antimicrobial characteristics. In a follow-up study, the authors fabricated microneedle arrays that contain Polyethylene Glycol-Gentamicin Sulfate, which inhibited growth of *Staphylococcus aureus* bacteria [68].

**2.1.2. Two-Photon Erosion Technology for Tissue Engineering.** Photodegradation is the alteration of a molecule by infrared, visible, or ultraviolet radiation. Two-photon excitation using a pulsed laser induces degradation within hydrogels over multiple length scales by cleaving components within the cross-linked biomaterial. This method achieves submicrometer resolution and can erode the focal volume within the bulk material; these traits have been exploited to develop platforms for various *in vitro* studies.

Lee et al. [69] suggested a micropatterning technique that uses two-photon-induced erosion (2PIE) to control the 3D arrangement of biomolecules and cells at the micrometer scale. The authors fabricated a 3D micropattern of cell adhesive ligand (Arg-Gly-Asp-Ser: RGDS) in collagenase-sensitive poly(ethylene glycol-co-peptide) diacrylate hydrogels to guide cell migration along predefined 3D pathways and human dermal fibroblasts encapsulated within the micropatterned collagenase-sensitive hydrogels were located in the center of the hydrogel construct. After preparation of the 3D pathway, cells migrated along predefined 3D RGDS pathways. Their result showed the possibility of guiding tissue regeneration by using 3D scaffolds with highly defined microscale geometry.

Kloxin et al. [70] synthesized photodegradable poly(ethylene glycol) based hydrogel, which has physical and biological properties that can be modulated in the presence of cells by ultraviolet, visible, and two-photon irradiation. 3D channels that were fabricated using 2PIE within a hydrogel allowed migration of hydrogel-encapsulated cells, and variation of the gel composition induced chondrogenic differentiation of encapsulated stem cells. These photodegradable hydrogels showed promise as *in vitro* 3D cell culture platforms in which an interaction between cells and materials is elucidated by the processing information of cells. These methods may be useful in applications such as drug-delivery vehicles and tissue-engineering systems.

Tibbitt et al. [31] presented a PEG-based hydrogel in which the geometry and context of the extracellular environment were controlled by 2PIE (Figure 4). They characterized the 2PIE process and demonstrated its efficacy in cell culture. To erode a gel completely, they selected 2PIE parameters in the presence of cells and then eroded microscale structures on and in the gel to confirm the patterning resolution. They used 2PIE to erode the material at the cell-gel interface and remove cell adhesion sites selectively. Finally, they monitored the stem cell response by detachment between cells and soft materials. This technique allows users to manipulate precisely the context and geometry of a cell's underlying microenvironment.

**2.1.3. Two-Photon Ablation Technology for Tissue Engineering.** Two-photon lithography (2PL) can provide high-resolution material processing without requiring a chemical developer

or a photomask [71, 72]. Intense pulses of femtosecond laser can cause nonlinear absorption processes (e.g., multiphoton-initiated avalanche ionization) that can damage transparent dielectrics [73]. However, heat exchange is limited during femtosecond pulsed laser irradiation, so thermal stress and collateral damage are minimized. Thus this laser can achieve submicrometer resolution when ablating biomaterials.

Jeon et al. [32] used a two-photon laser to write nanoscale chemical patterns on thin polymer film. Poly(ethylene glycol) methacrylate (PEG-MA) layers were prepared on quartz substrates, and then nonlinear absorbance of pairs of photons from femtosecond laser was used to ablate the underlying substrate. Single-shot ablation allowed the patterning of nanoscale features without a damage of the substrate (Figure 5). The diameter of the laser spot was  $0.86\text{ }\mu\text{m}$  at  $1/e^2$  width, and the exposed feature size on the substrate was  $\sim 80\text{ nm}$  in that condition. Fabricated patterns could control the adhesion and migration of 3T3 fibroblasts, so this study demonstrated the use of two-photon ablation technology to realize a microenvironment.

**2.2. 3D Printing Based on Controlled Electrospinning.** Electrospinning is a versatile 3D printing technique that uses a biopolymer; the method was first proposed in 1934 [26]. Electrospinning is based on the creation of fibers by ejecting an electrically charged viscoelastic polymer solution onto a collector. The travel pathway of the charged polymer solution is guided by a strong electric field that is generated by a high voltage between a polymer solution outlet and the collector guide [27]. By the control of solution conditions (pH, concentration, and solvent), device conditions (distance between tip and plate, strength of electric field, and dimensions of nozzle), and collection methods (plate versus rotating mandrel and speed of collection), this technique can produce ultrafine fibers with a wide range of diameters from several micrometers to a few nanometers. However, electrospun nanofibers undergo a whipping motion, so an electrospun product is normally a nonwoven mat of randomly oriented fibers. This characteristic has limited the use of this method to fabricate patient-customized architectures for use in tissue regeneration. However, various techniques to align and position the nanofibers have been developed, so the electrospinning technology has been utilized in tissue engineering and regenerative medicine area.

**2.2.1. 2D Pattern Fabrication Using Controlled Electrospinning.** Research on the morphology of nanofibrous structures has mainly focused on nanofiber alignment [33, 74–77]. However, although achieving alignment of the nanofiber was a significant breakthrough that allowed deposition of structured nanofiber mats, the precision of alignment is still limited by difficulties in controlling the geometric features of the electrospun mats and in introducing geometrical functionalities. Therefore, new methods, such as direct nanofiber patterning, a prepatterned conductive collector, have been studied.

Bellan and Craighead [78] used electric fields to confine and steer an electrospun polymer jet for controlled deposition of functional materials and used an electrode between the electrospinning tip and grounded sample to suppress the

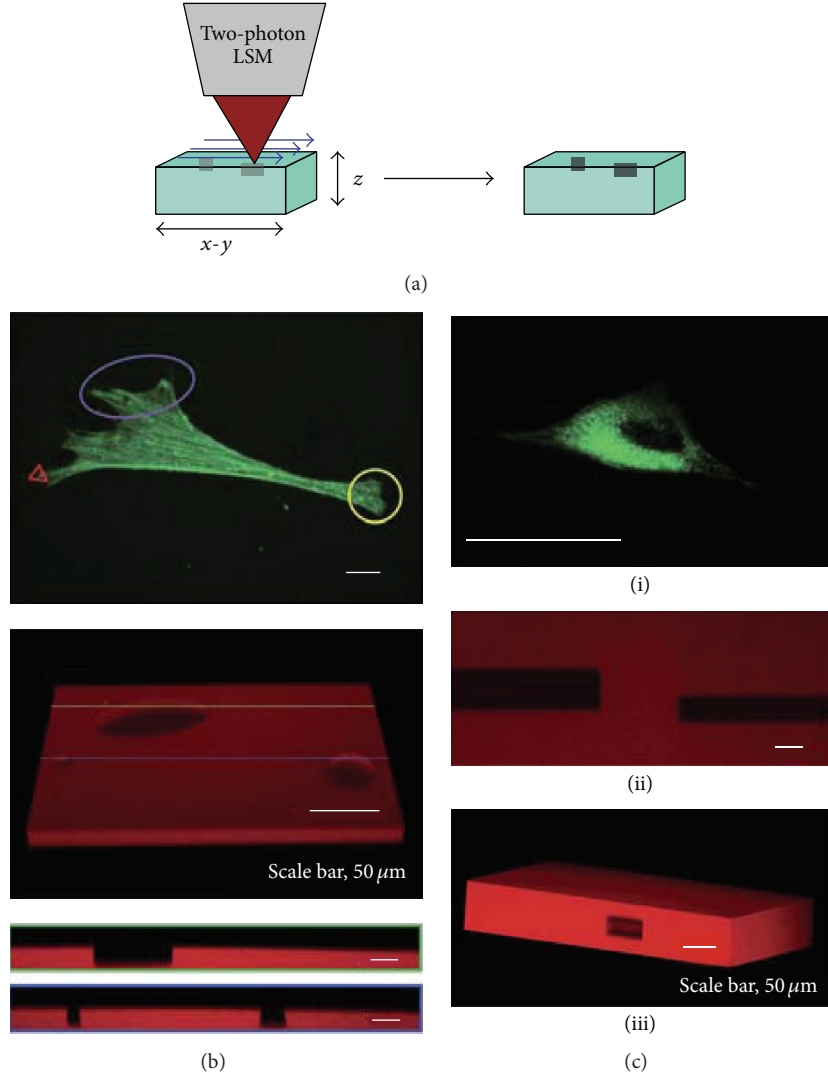


FIGURE 4: Feature formation to control ECM context and geometry. (a) Defined features can be patterned at the surface or within PEGdiPDA hydrogels by rastering the focal point of a two-photon laser scanning microscope (LSM, Zeiss LSM 710) through specific geometries using region of interest software. (b) Surface feature formation can be performed on size scales relevant to the cell ( $\sim 1$  to  $100$  nm) and spatially confined to desired regions to disrupt adhesion at the front or back side of adhered cells (purple oval and yellow circle) or to disrupt adhesion at individual filopodia (red triangle). To demonstrate this strategy, feature formation was performed in the absence of cells on the order of microns (red triangle) to  $100$  nm (purple oval) and was monitored with confocal microscopy (3D renderings of fluorescent confocal stacks and the corresponding cross sections, green and blue lines). (c) Features were also patterned within the bulk of PEGdiPDA hydrogels to motivate the utility of this approach for directing encapsulated cells ((c)(i)) to migrate down specific channels ((c)(ii)) or for defining the geometry of the cell niche ((c)(iii)).  $20$  nm and  $30$  nm wide channels were patterned into PEGdiPDA gels ((c)(ii)) for representative channel formation, and a  $45$  nm wide square cylinder was patterned into a gel ((c)(iii)) as a representative change to the geometry of the cell niche. Scale bars represent  $20$  nm, except as noted (figures were reproduced from [31] with permission of Royal Society of Chemistry).

chaotic whipping mode, thereby reducing the diameter of the characteristic spot. By modifying the electrode setup, they deposited isolated electrospun fibers in controlled positions and terminated electrospun fibers quickly. Their results will allow the increase in the complexity of the geometries that can be fabricated using electrospun nanofibers.

Dalton et al. [79] used melt electrospinning and demonstrated that simple nanofibrous patterns with line widths as small as  $500$  μm can be fabricated by increasing the tip-to-collector distance and reducing the speed of the plate

collector. Electrospun fibers collected in focused spots were used in the patterning and drawing of a cell adhesive scaffold. Aligned electrospun fiber lines of  $200$ – $400$  μm width could be applied continuously or discretely onto a slide mounted on an  $x$ - $y$  stage. This direct electrospinning writing technique will provide scaffold-building devices suitable for tissue engineering applications.

Zhang and Chang [80] used electroconductive collectors to fabricate poly(lactic acid) (PLA) electrospun mats with different patterned structures (Figure 6). To control the

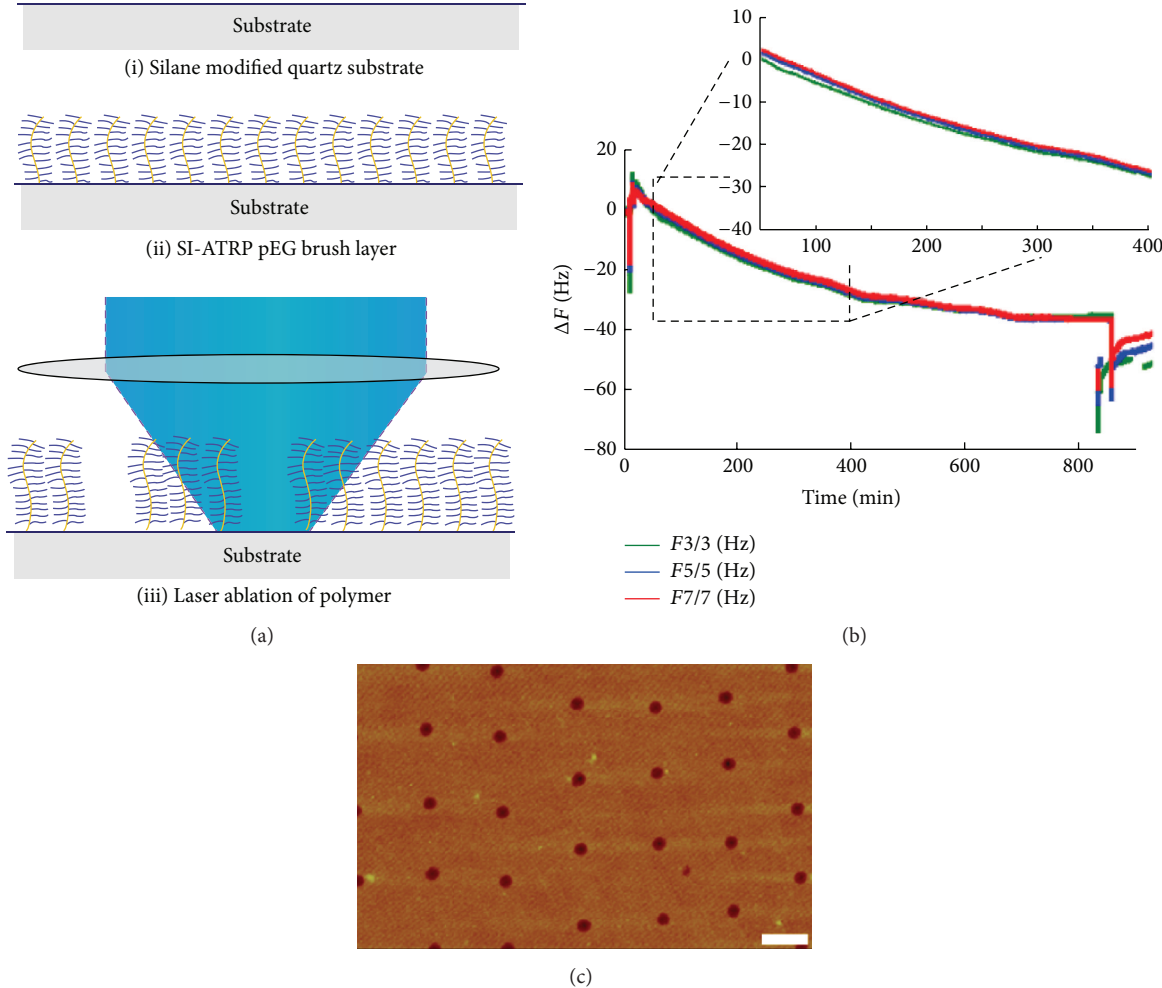


FIGURE 5: (a) Schematic of laser ablation. Polymer is grown from surface-bound ATRP initiator and ablated by a 100 fs, 400 nm laser pulse. (b) QCM-D measurement of polymer thickness. A measurement result indicates linear growth of the living radical polymerization, ensuring the smooth, uniform films necessary for consistent laser ablation. (c) AFM image of 250 nm dot pattern in 20 nm film (scale bar is 1  $\mu$ m) (figures were reproduced from [32] with permission of ACS Publications).

patterns and architectures and the parameters that affect the formation of the patterns of the fibrous materials, the authors designed an electroconductive template. They demonstrated that protrusions on collectors are an important feature that may induce structures in the electrospun mat and that woven constructs can be fabricated by time-dependent control of the protrusion arrangement of the collector. These effects of protrusion arrangement and designed patterns have potential for use in supplying fibrous mats for biomedical applications.

Kharaziha et al. [81] fabricated elastomeric biodegradable poly(glycerol sebacate) (PGS):gelatin aligned nanofibrous scaffolds with various chemical composition, stiffness, and anisotropy. They incorporated PGS to create nanofibrous scaffolds that mimic the architecture of the left ventricular myocardium. They studied attachment, proliferation, alignment, and differentiation of neonatal rat cardiac fibroblast cells. They also studied protein expression and contractile function of cardiomyocytes on PGS:gelatin scaffolds. An

aligned nanofibrous scaffold with 33 wt% PGS enhanced the cellular alignment of cardiomyocytes and elicited optimal synchronous contractions of them. These results suggest that the electrospun PGS:gelatin scaffold with an alignment had an important influence on the organization, phenotype, and contraction of cardiac cells and can be used in engineering of cardiac tissue.

**2.2.2. 3D Scaffold Fabrication Using Controlled Electrospinning.** Despite numerous benefits of electrospinning technology, it cannot easily fabricate macroscopically porous 3D nanofibrous scaffolds, due to their entangled fibers and densely packed membranous structure [82]. Although electrospun scaffolds provide favorable cellular interaction due to internal architectures, as in native tissue, cellular migration within 3D electrospun scaffolds has been limited because of their inherently small pore sizes. Furthermore, the porosity of these scaffolds cannot be controlled. To solve these problems,

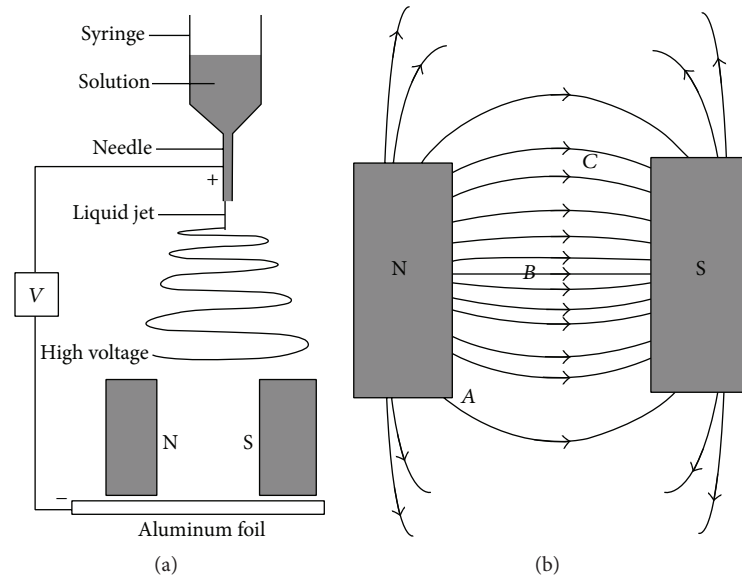


FIGURE 6: (a) Illustration of the apparatus for magnetic electrospinning (MES) to generate aligned fibers. The key component of the system is a magnetic field generated by two parallel-positioned permanent magnets. (b) Calculated magnetic field strength vectors in the region between the two magnets (top view) (figures were reproduced from [33] with permission of John Wiley and Sons).

some new approaches have been developed that control the electrode position to produce advanced electrospun 3D scaffolds.

Lee et al. [83] developed direct-write electrospinning (DWES) with improved focusing and scanning functionalities to generate nanofibrous mats. The authors demonstrated that DWES could control the geometry and dimensions of nanofibrous patterns and mats. Fabricated nanofibrous mats were used as patterns for cell alignment. 3D nanofibrous scaffolds with regular pores were developed by stacking the nanofibrous mats into a 3D structure [83, 84]. After preparing the 3D nanofibrous structures, they compared the cellular interactions induced by DWES, conventional electrospinning, and salt leaching technique. Cell migration to the inner space was better in the DWES scaffold than in the scaffold produced using conventional electrospinning. Scaffolds fabricated using DWES will eventually improve cellular migration into the core and aid in 3D tissue formation.

Teo et al. [33] controlled the motion of the electrospinning jet by use of knife edges to control the electrostatic field forces. The authors used polycaprolactone (PCL) as a biodegradable base material and fabricated tubular scaffolds with diagonally aligned fibers to be collected on a rotating tube. The tubular scaffold was formed with uniform thickness and possessed superior mechanical strength without any line of weakness. This technique may be used in development of strong tubular structures as blood vessel scaffolds.

Vaz et al. [85] used sequential multilayering electrospinning (ME) with a rotating mandrel-type collector to develop a scaffold that mimics both morphology and mechanical properties of a blood vessel. A bilayered tubular scaffold was composed of an outer layer composed of well-oriented stiff PLA fibers and an inner region composed of randomly oriented pliable PLA/PCL fibers. The degree of fiber orientation in the two layers was controlled by adjusting the rotation speed of

the collector. Their scaffolds showed 10% elastic strain. They improved the attachment and proliferation of 3T3 mouse fibroblasts and human venous myofibroblasts. These results suggest that electrospun PLA/PCL bilayered tubular scaffolds with appropriate characteristics may be useful to guide regeneration of blood vessels.

Ignatova et al. [86] fabricated biocomponent nanofibrous mats by electrospinning mixed solutions of chitosan (Ch) or quaternized chitosan (Qch) and poly[(L-lactide)-co-(D,L-lactide)] (PLA). Cross-linked electrospun Ch/PLA and QCh/PLA mats inhibited growth of the *S. aureus* and *E. coli* more effectively than did solvent-cast film fabricated using the same materials. The reason for the difference was that Ch and QCh that were incorporated into electrospun mats decreased the ability of the bacteria to adhere to them. These hybrid nanofibrous mats may be useful in wound-healing applications.

Kim and Park [87] fabricated biodegradable polymeric nanocylinders by degradation of electrospun nanofibers. To make nanocylinders, nanofiber aggregates were uniformly dispersed in aqueous solution by aminolytic degradation of long electrospun fibers for reassembly of the fibers with controllable orientation and architecture. From transverse fragmentation of semicrystalline poly(L-lactic acid) (PLA) nanofibers, cylindrical and biodegradable nanomaterials with various aspect ratios were prepared. This approach showed the fabrication of ECM-mimicking nanofilaments which could potentially be assembled into highly ordered structures.

Zhang and Chang [34] suggested a static method to fabricate 3D fibrous tubes composed of ultrafine electrospun fibers (Figure 7). They used a 3D collecting template based on manipulation of electric fields and forces to fabricate 3D architecture. This technique can fabricate micro- and macro-tubes with multiple micropatterns, multiple interconnected

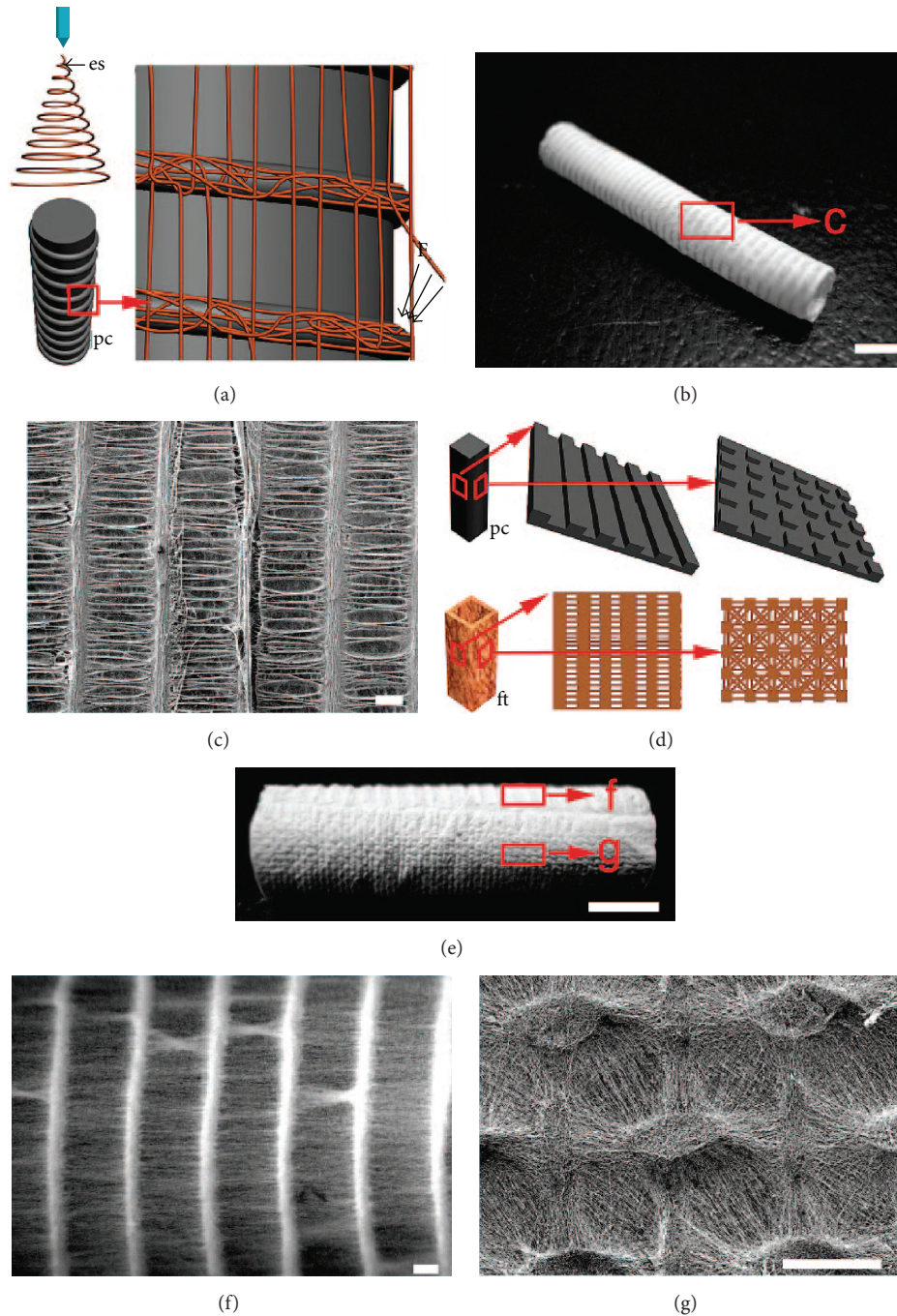


FIGURE 7: (a) Schematic illustration of collecting process using a cylindrical collector with equally spaced circular protrusions (es, electrospinning process; pc, patterned collector). (b) A fibrous tube with patterned architectures (scale bar = 5 mm). (c) Magnified image of panel (b) (scale bar = 200  $\mu$ m). (d) Schematic illustration of collectors with two different patterns and relevant fibrous tube (pc, patterned collector; ft, fibrous tube). (e) A fibrous tube with two different patterns (scale bar = 5 mm). (f, g) Magnified images of two different patterns of panel (e) (scale bar = 200  $\mu$ m) (figures were reproduced from [34] with permission of ACS Publications).

tubes, and many tubes with the same or different sizes, structure, shapes, and patterns. The authors investigated parameters that can affect the order degree of patterns. This technique to control the patterned architecture has many biomedical and industrial applications.

Aligned nanofibrous scaffolds fabricated using electrospinning can affect cell and matrix organization. However, their widespread application has been impeded by the poor cell infiltration due to the tight packing of the fibers. Therefore, Baker et al. [88] suggested tunable composite

nanofibrous scaffolds with water-soluble sacrificial fibers. Composites were composed of two fibers: slow-degrading poly( $\epsilon$ -caprolactone) (PCL) and water-soluble poly(ethylene oxide) (PEO), which is removed to increase the internal pore size in the fabricated 3D scaffold. PEO was spontaneously degraded by hydration, thereby leaving large pores that facilitated cellular infiltration. Although more than half of the initial fibers were removed, the remaining scaffold induced sufficient cell alignment and formation of a highly organized extracellular matrix at several length scales, and 3D cartilage tissue (>1 mm thick) was formed at 12 weeks after implantation. This technique can be used to support regeneration of load-bearing fibrous tissues.

### 3. Summary

This review has described 3D printing technologies with nanometer resolution for use in tissue engineering. 3D printing technologies have great advantages over traditional scaffold fabrication methods in the control of porosity, pore size, and interconnectivity. 3D printing methods can fabricate a 3D scaffold as designed, so they can be used to standardize 3D scaffolds. Among various 3D printing methods, two-photon laser-based nanofabrication and controlled electrospinning have received attention in various areas of tissue engineering due to their abilities to fabricate structures with high surface-to-volume ratio and highly interconnected porous architecture at submicrometer resolution. Use of these methods has yielded precise 3D scaffolds that mimic the organization of the extracellular matrix, and their characteristics have helped to study unknown cellular behaviors including adhesion, proliferation, and differentiation. The scaffolds have been used in studies of molecular biology and cell dynamics, so new possibilities for the improvement of tissue regeneration have been suggested. Future development of 3D nanoscaffolds should focus on increasing the precision of scaffold fabrication systems, on identifying new biomaterials, and on the role of biomolecules in cell behaviors such as adhesion, proliferation, and differentiation. Given the concentration on these topics, 3D nanoprinting technologies will become important tools in tissue engineering in the near future. High-resolution 3D biomimetic environments will become useful substrates in the search for mechanisms of vital phenomenon.

### Conflict of Interests

There is no potential conflict of interests to disclose for this work.

### Acknowledgments

This research was supported by Gachon University Gil Medical Center (Grant no. FRD2014-02) and the National Research Foundation of Korea (NRF) grant funded by the Korea government (no. 2014R1A1A2A16054777).

### References

- [1] R. Thomson, M. Yaszemski, and A. G. Mikos, "Polymer scaffold processing," in *Principles of Tissue Engineering*, R. Lanza, R. Langer, and W. Chick, Eds., pp. 263–272, R.G. Landes Company, Austin, Tex, USA, 1997.
- [2] C. M. Agrawal, K. A. Athanasiou, and J. D. Heckman, "Biodegradable PLA-PGA polymers for tissue engineering in orthopaedics," *Materials Science Forum*, vol. 250, pp. 115–128, 1997.
- [3] R. B. Langer, "Selected advances in drug delivery and tissue engineering," *Journal of Controlled Release*, vol. 62, no. 1-2, pp. 7–11, 1999.
- [4] L. Lu and A. G. Mikos, "The importance of new processing techniques in tissue engineering," *MRS Bulletin*, vol. 21, no. 11, pp. 28–32, 1996.
- [5] T. Ozdemir, A. M. Higgins, and J. L. Brown, "Osteoinductive biomaterial geometries for bone regenerative engineering," *Current Pharmaceutical Design*, vol. 19, no. 19, pp. 3446–3455, 2013.
- [6] W. Chen, Y. Tabata, and Y. W. Tong, "Fabricating tissue engineering scaffolds for simultaneous cell growth and drug delivery," *Current Pharmaceutical Design*, vol. 16, no. 21, pp. 2388–2394, 2010.
- [7] A. G. Mikos, A. J. Thorsen, L. A. Czerwonka et al., "Preparation and characterization of poly(L-lactic acid) foams," *Polymer*, vol. 35, no. 5, pp. 1068–1077, 1994.
- [8] A. G. Mikos, Y. Bao, L. G. Cima, D. E. Ingber, J. P. Vacanti, and R. B. Langer, "Preparation of poly(glycolic acid) bonded fiber structures for cell attachment and transplantation," *Journal of Biomedical Materials Research*, vol. 27, no. 2, pp. 183–189, 1993.
- [9] H. Hall, "Modified fibrin hydrogel matrices: both, 3D-scaffolds and local and controlled release systems to stimulate angiogenesis," *Current Pharmaceutical Design*, vol. 13, no. 35, pp. 3597–3607, 2007.
- [10] G. M. Harris, K. Rutledge, Q. Cheng, J. Blanchette, and E. Jabbarzadeh, "Strategies to direct angiogenesis within scaffolds for bone tissue engineering," *Current Pharmaceutical Design*, vol. 19, no. 19, pp. 3456–3465, 2013.
- [11] E. Vanderleyden, S. Mullens, J. Luyten, and P. Dubrule, "Implantable (bio)polymer coated titanium scaffolds: a review," *Current Pharmaceutical Design*, vol. 18, no. 18, pp. 2576–2590, 2012.
- [12] A. G. Mikos, G. Sarakinos, S. M. Leite, J. P. Vacant, and R. Langer, "Laminated three-dimensional biodegradable foams for use in tissue engineering," *Biomaterials*, vol. 14, no. 5, pp. 323–330, 1993.
- [13] D. J. Mooney, D. F. Baldwin, N. P. Suh, J. P. Vacanti, and R. Langer, "Novel approach to fabricate porous sponges of poly(D,L-lactic-co-glycolic acid) without the use of organic solvents," *Biomaterials*, vol. 17, no. 14, pp. 1417–1422, 1996.
- [14] I. Zein, D. W. Hutmacher, K. C. Tan, and S. H. Teoh, "Fused deposition modeling of novel scaffold architectures for tissue engineering applications," *Biomaterials*, vol. 23, no. 4, pp. 1169–1185, 2002.
- [15] T. D. Roy, J. L. Simon, J. L. Ricci, E. D. Rekow, V. P. Thompson, and J. R. Parsons, "Performance of hydroxyapatite bone repair scaffolds created via three-dimensional fabrication techniques," *Journal of Biomedical Materials Research—Part A*, vol. 67, no. 4, pp. 1228–1237, 2003.
- [16] T.-M. G. Chu, D. G. Orton, S. J. Hollister, S. E. Feinberg, and J. W. Halloran, "Mechanical and in vivo performance of hydroxyapatite implants with controlled architectures," *Biomaterials*, vol. 23, no. 5, pp. 1283–1293, 2002.
- [17] F. Pati, J. Jang, D.-H. Ha et al., "Printing three-dimensional tissue analogues with decellularized extracellular matrix bioink," *Nature Communications*, vol. 5, article 3935, 2014.

- [18] R. A. Barry III, R. F. Shepherd, J. N. Hanson, R. G. Nuzzo, P. Wiltzius, and J. A. Lewis, "Direct-write assembly of 3D hydrogel scaffolds for guided cell growth," *Advanced Materials*, vol. 21, no. 23, pp. 2407–2410, 2009.
- [19] M. N. Cooke, J. P. Fisher, D. Dean, C. Rimnac, and A. G. Mikos, "Use of stereolithography to manufacture critical-sized 3D biodegradable scaffolds for bone ingrowth," *Journal of Biomedical Materials Research—Part B: Applied Biomaterials*, vol. 64, no. 2, pp. 65–69, 2003.
- [20] J. W. Lee, P. X. Lan, B. Kim, G. Lim, and D.-W. Cho, "Fabrication and characteristic analysis of a poly(propylene fumarate) scaffold using micro-stereolithography technology," *Journal of Biomedical Materials Research—Part B: Applied Biomaterials*, vol. 87, no. 1, pp. 1–9, 2008.
- [21] W.-S. Chu, S.-Y. Jeong, J. K. Pandey, S.-H. Ahn, J.-H. Lee, and S.-C. Chi, "Fabrication of composite drug delivery system using nano composite deposition system and in vivo characterization," *International Journal of Precision Engineering and Manufacturing*, vol. 9, no. 2, pp. 81–83, 2008.
- [22] K. W. Lee, S. Wang, B. C. Fox, E. L. Ritman, M. J. Yaszemski, and L. Lu, "Poly(propylene fumarate) bone tissue engineering scaffold fabrication using stereolithography: effects of resin formulations and laser parameters," *Biomacromolecules*, vol. 8, no. 4, pp. 1077–1084, 2007.
- [23] P. X. Lan, J. W. Lee, Y.-J. Seol, and D.-W. Cho, "Development of 3D PPF/DEF scaffolds using micro-stereolithography and surface modification," *Journal of Materials Science: Materials in Medicine*, vol. 20, no. 1, pp. 271–279, 2009.
- [24] J.-H. Shim, J. Y. Kim, J. K. Park et al., "Effect of thermal degradation of SFF-based PLGA Scaffolds fabricated using a multi-head deposition system followed by change of cell growth rate," *Journal of Biomaterials Science, Polymer Edition*, vol. 21, no. 8-9, pp. 1069–1080, 2010.
- [25] Y.-M. Ha, I.-B. Park, H.-C. Kim, and S.-H. Lee, "Three-dimensional microstructure using partitioned cross-sections in projection microstereolithography," *International Journal of Precision Engineering and Manufacturing*, vol. 11, no. 2, pp. 335–340, 2010.
- [26] Z.-M. Huang, Y.-Z. Zhang, M. Kotaki, and S. Ramakrishna, "A review on polymer nanofibers by electrospinning and their applications in nanocomposites," *Composites Science and Technology*, vol. 63, no. 15, pp. 2223–2253, 2003.
- [27] E. D. Boland, J. A. Matthews, K. J. Pawlowski, D. G. Simpson, G. E. Wnek, and G. L. Bowlin, "Electrospinning collagen and elastin: preliminary vascular tissue engineering," *Frontiers in Bioscience*, vol. 9, pp. 1422–1432, 2004.
- [28] W. Liu, Y. Li, J. Liu, X. Niu, Y. Wang, and D. Li, "Application and performance of 3D printing in nanobiomaterials," *Journal of Nanomaterials*, vol. 2013, Article ID 681050, 7 pages, 2013.
- [29] F. Claeysens, E. A. Hasan, A. Gaidukeviciute et al., "Three-dimensional biodegradable structures fabricated by two-photon polymerization," *Langmuir*, vol. 25, no. 5, pp. 3219–3223, 2009.
- [30] W. Zhang, P. Soman, K. Meggs, X. Qu, and S. Chen, "Tuning the poisson's ratio of biomaterials for investigating cellular response," *Advanced Functional Materials*, vol. 23, no. 25, pp. 3226–3232, 2013.
- [31] M. W. Tibbitt, A. M. Kloxin, K. U. Dyamenahalli, and K. S. Anseth, "Controlled two-photon photodegradation of PEG hydrogels to study and manipulate subcellular interactions on soft materials," *Soft Matter*, vol. 6, no. 20, pp. 5100–5108, 2010.
- [32] H. Jeon, R. Schmidt, J. E. Barton et al., "Chemical patterning of ultrathin polymer films by direct-write multiphoton lithography," *Journal of the American Chemical Society*, vol. 133, no. 16, pp. 6138–6141, 2011.
- [33] W. E. Teo, M. Kotaki, X. M. Mo, and S. Ramakrishna, "Porous tubular structures with controlled fibre orientation using a modified electrospinning method," *Nanotechnology*, vol. 16, no. 6, pp. 918–924, 2005.
- [34] D. Zhang and J. Chang, "Electrospinning of three-dimensional nanofibrous tubes with controllable architectures," *Nano Letters*, vol. 8, no. 10, pp. 3283–3287, 2008.
- [35] H. Kodama, "Automatic method for fabricating a three-dimensional plastic model with photo-hardening polymer," *Review of Scientific Instruments*, vol. 52, no. 11, pp. 1770–1773, 1981.
- [36] T. Nakai and Y. Marutani, "Fabrication of 3-D prototypes by using ultraviolet laser and liquid photopolymer," in *Proceedings of the Conference on Lasers and Electro-Optics*, ME-2, San Francisco, Calif, USA, June 1986.
- [37] H.-W. Kang, I. H. Lee, and D.-W. Cho, "Development of an assembly-free process based on virtual environment for fabricating 3D microfluidic systems using microstereolithography technology," *Journal of Manufacturing Science and Engineering*, vol. 126, no. 4, pp. 766–771, 2004.
- [38] R. Liska, M. Schuster, R. Inführ et al., "Photopolymers for rapid prototyping," *Journal of Coatings Technology Research*, vol. 4, no. 4, pp. 505–510, 2007.
- [39] J.-F. Xing, X.-Z. Dong, W.-Q. Chen et al., "Improving spatial resolution of two-photon microfabrication by using photoinitiator with high initiating efficiency," *Applied Physics Letters*, vol. 90, no. 13, Article ID 131106, 2007.
- [40] A. Koroleva, S. Gittard, S. Schlie, A. Deiwick, S. Jockenhoevel, and B. Chichkov, "Fabrication of fibrin scaffolds with controlled microscale architecture by a two-photon polymerization-micromolding technique," *Biofabrication*, vol. 4, no. 1, Article ID 015001, 2012.
- [41] A. Koroleva, A. A. Gill, I. Ortega et al., "Two-photon polymerization-generated and micromolding-replicated 3D scaffolds for peripheral neural tissue engineering applications," *Biofabrication*, vol. 4, no. 2, Article ID 025005, 2012.
- [42] D. S. Correa, P. Tayalia, G. Cosensey et al., "Two-photon polymerization for fabricating structures containing the biopolymer chitosan," *Journal of Nanoscience and Nanotechnology*, vol. 9, no. 10, pp. 5845–5849, 2009.
- [43] O. Kufelt, A. El-Tamer, C. Sehring, M. Meißner, S. Schlie-Wolter, and B. N. Chichkov, "Water-soluble photopolymerizable chitosan hydrogels for biofabrication via two-photon polymerization," *Acta Biomaterialia*, vol. 18, pp. 186–195, 2015.
- [44] H. D. Cha, J. M. Hong, T.-Y. Kang, J. W. Jung, D.-H. Ha, and D.-W. Cho, "Effects of micro-patterns in three-dimensional scaffolds for tissue engineering applications," *Journal of Micromechanics and Microengineering*, vol. 22, no. 12, Article ID 125002, 2012.
- [45] A. Marino, C. Filippeschi, G. G. Genchi, V. Mattoli, B. Mazzolai, and G. Ciofani, "The Osteoprint: a bioinspired two-photon polymerized 3-D structure for the enhancement of bone-like cell differentiation," *Acta Biomaterialia*, vol. 10, no. 10, pp. 4304–4313, 2014.
- [46] A. Doraiswamy, C. Jin, R. J. Narayan et al., "Two-photon induced polymerization of organic-inorganic hybrid biomaterials for microstructured medical devices," *Acta Biomaterialia*, vol. 2, no. 3, pp. 267–275, 2006.

- [47] A. J. G. Otuka, D. S. Corrêa, C. R. Fontana, and C. R. Mendonça, “Direct laser writing by two-photon polymerization as a tool for developing microenvironments for evaluation of bacterial growth,” *Materials Science and Engineering C*, vol. 35, no. 1, pp. 185–189, 2014.
- [48] M. T. Raimondi, S. M. Eaton, M. Laganà et al., “Three-dimensional structural niches engineered via two-photon laser polymerization promote stem cell homing,” *Acta Biomaterialia*, vol. 9, no. 1, pp. 4579–4584, 2013.
- [49] H. Jeon, H. Hidai, D. J. Hwang, and C. P. J. Grigoropoulos, “Fabrication of arbitrary polymer patterns for cell study by two-photon polymerization process,” *Journal of Biomedical Materials Research—Part A*, vol. 93, no. 1, pp. 56–66, 2010.
- [50] L. L. Lebel, B. Aissa, M. A. El Khakani, and D. Therriault, “Ultraviolet-assisted direct-write fabrication of carbon nanotube/polymer nanocomposite microcoils,” *Advanced Materials*, vol. 22, no. 5, pp. 592–596, 2010.
- [51] T. D. Brown, P. D. Dalton, and D. W. Hutmacher, “Direct writing by way of melt electrospinning,” *Advanced Materials*, vol. 23, no. 47, pp. 5651–5657, 2011.
- [52] V. Chan, P. Zorlutuna, J. H. Jeong, H. Kong, and R. Bashir, “Three-dimensional photopatterning of hydrogels using stereolithography for long-term cell encapsulation,” *Lab on a Chip*, vol. 10, no. 16, pp. 2062–2070, 2010.
- [53] J. Zheng, H. Xie, W. Yu et al., “Enhancement of surface graft density of MPEG on alginate/chitosan hydrogel microcapsules for protein repellency,” *Langmuir*, vol. 28, no. 37, pp. 13261–13273, 2012.
- [54] U. Gbureck, E. Vorndran, F. A. Müller, and J. E. Barralet, “Low temperature direct 3D printed bioceramics and biocomposites as drug release matrices,” *Journal of Controlled Release*, vol. 122, no. 2, pp. 173–180, 2007.
- [55] G. M. Gratson, F. García-Santamaría, V. Lousse et al., “Direct-write assembly of three-dimensional photonic crystals: conversion of polymer scaffolds to silicon hollow-woodpile structures,” *Advanced Materials*, vol. 18, no. 4, pp. 461–465, 2006.
- [56] W. Wu, A. Deconinck, and J. A. Lewis, “Omnidirectional printing of 3D microvascular networks,” *Advanced Materials*, vol. 23, no. 24, pp. 178–183, 2011.
- [57] V. Karageorgiou and D. Kaplan, “Porosity of 3D biomaterial scaffolds and osteogenesis,” *Biomaterials*, vol. 26, no. 27, pp. 5474–5491, 2005.
- [58] A. Gould, Y. Ji, T. L. Aboye, and J. A. Camarero, “Cyclotides, a novel ultrastable polypeptide scaffold for drug discovery,” *Current Pharmaceutical Design*, vol. 17, no. 38, pp. 4294–4307, 2011.
- [59] S. Maya, B. Sarmento, A. Nair, N. S. Rejinold, S. V. Nair, and R. Jayakumar, “Smart stimuli sensitive nanogels in cancer drug delivery and imaging: a review,” *Current Pharmaceutical Design*, vol. 19, no. 41, pp. 7203–7218, 2013.
- [60] G. G. Adams and S. E. Harding, “Drug delivery systems for the treatment of diabetes mellitus: state of the art,” *Current Pharmaceutical Design*, vol. 19, no. 41, pp. 7244–7263, 2013.
- [61] C. W. Gan, S. Chien, and S.-S. Feng, “Nanomedicine: enhancement of chemotherapeutic efficacy of docetaxel by using a biodegradable nanoparticle formulation,” *Current Pharmaceutical Design*, vol. 16, no. 21, pp. 2308–2320, 2010.
- [62] J. Xie, C. Lei, Y. Hu, G. K. Gay, N. H. B. Jamali, and C.-H. Wang, “Nanoparticulate formulations for paclitaxel delivery across MDCK cell monolayer,” *Current Pharmaceutical Design*, vol. 16, no. 21, pp. 2331–2340, 2010.
- [63] B. P. Chan, J. N. Ma, J. Y. Xu, C. W. Li, J. P. Cheng, and S. H. Cheng, “Femto-second Laser-based free writing of 3D protein microstructures and micropatterns with Sub-micrometer features: a study on voxels, porosity, and cytocompatibility,” *Advanced Functional Materials*, vol. 24, no. 3, pp. 277–294, 2014.
- [64] S. Turunen, E. Käpylä, K. Terzaki et al., “Pico- and femtosecond laser-induced crosslinking of protein microstructures: evaluation of processability and bioactivity,” *Biofabrication*, vol. 3, no. 4, Article ID 045002, 2011.
- [65] T. S. Drakakis, G. Papadakis, K. Sambani et al., “Construction of three-dimensional biomolecule structures employing femtosecond lasers,” *Applied Physics Letters*, vol. 89, no. 14, Article ID 144108, 2006.
- [66] M. Farsari, M. Vamvakaki, and B. N. Chichkov, “Multiphoton polymerization of hybrid materials,” *Journal of Optics*, vol. 12, no. 12, Article ID 124001, 2010.
- [67] S. D. Gittard, R. J. Narayan, C. Jin et al., “Pulsed laser deposition of antimicrobial silver coating on Ormocer microneedles,” *Biofabrication*, vol. 1, no. 4, Article ID 041001, 2009.
- [68] S. D. Gittard, A. Ovsianikov, H. Akar et al., “Two photon polymerization-micromolding of polyethylene glycol-gentamicin sulfate microneedles,” *Advanced Engineering Materials*, vol. 12, no. 4, pp. B77–B82, 2010.
- [69] S.-H. Lee, J. J. Moon, and J. L. West, “Three-dimensional micro-patterning of bioactive hydrogels via two-photon laser scanning photolithography for guided 3D cell migration,” *Biomaterials*, vol. 29, no. 20, pp. 2962–2968, 2008.
- [70] A. M. Kloxin, A. M. Kasko, C. N. Salinas, and K. S. Anseth, “Photodegradable hydrogels for dynamic tuning of physical and chemical properties,” *Science*, vol. 324, no. 5923, pp. 59–63, 2009.
- [71] D. A. Higgins, T. A. Everett, A. Xie, S. M. Forman, and T. Ito, “High-resolution direct-write multiphoton photolithography in poly(methylmethacrylate) films,” *Applied Physics Letters*, vol. 88, no. 18, Article ID 184101, 2006.
- [72] S. Ibrahim, D. A. Higgins, and L. T. Ito, “Direct-write multiphoton photolithography: a systematic study of the etching behaviors in various commercial polymers,” *Langmuir*, vol. 23, no. 24, pp. 12406–12412, 2007.
- [73] P. Grigoropoulos, *Transport in Laser Microfabrication: Fundamentals and Applications*, Cambridge University Press, New York, NY, USA, 2009.
- [74] P. Katta, M. Alessandro, R. D. Ramsier, and G. G. Chase, “Continuous electrospinning of aligned polymer nanofibers onto a wire drum collector,” *Nano Letters*, vol. 4, no. 11, pp. 2215–2218, 2004.
- [75] D. Li, Y. Wang, and Y. Xia, “Electrospinning nanofibers as uniaxially aligned arrays and layer-by-layer stacked films,” *Advanced Materials*, vol. 16, no. 4, pp. 361–366, 2004.
- [76] B. Sundaray, V. Subramanian, T. S. Natarajan, R.-Z. Xiang, C.-C. Chang, and W.-S. Fann, “Electrospinning of continuous aligned polymer fibers,” *Applied Physics Letters*, vol. 84, no. 7, article 1222, 2004.
- [77] D. Yang, B. Lu, Y. Zhao, and X. Jiang, “Fabrication of aligned fibrous arrays by magnetic electrospinning,” *Advanced Materials*, vol. 19, no. 21, pp. 3702–3706, 2007.
- [78] L. M. Bellan and H. G. Craighead, “Control of an electrospinning jet using electric focusing and jet-steering fields,” *Journal of Vacuum Science and Technology B*, vol. 24, no. 6, pp. 3179–3183, 2006.
- [79] P. D. Dalton, N. T. Joergensen, J. Groll, and M. Moeller, “Patterned melt electrospun substrates for tissue engineering,” *Biomedical Materials*, vol. 3, no. 3, Article ID 034109, 2008.

- [80] D. Zhang and J. Chang, "Patterning of electrospun fibers using electroconductive templates," *Advanced Materials*, vol. 19, no. 21, pp. 3664–3667, 2007.
- [81] M. Kharaziha, M. Nikkhah, S.-R. Shin et al., "PGS:gelatin nanofibrous scaffolds with tunable mechanical and structural properties for engineering cardiac tissues," *Biomaterials*, vol. 34, no. 27, pp. 6355–6366, 2013.
- [82] T. G. Kim, H. Shin, and D. W. Lim, "Biomimetic scaffolds for tissue engineering," *Advanced Functional Materials*, vol. 22, no. 12, pp. 2446–2468, 2012.
- [83] J. Lee, S. Y. Lee, J. Jang, Y. H. Jeong, and D.-W. Cho, "Fabrication of patterned nanofibrous mats using direct-write electrospinning," *Langmuir*, vol. 28, no. 18, pp. 7267–7275, 2012.
- [84] J. Lee, J. Jang, H. Oh, Y. H. Jeong, and D.-W. Cho, "Fabrication of a three-dimensional nanofibrous scaffold with lattice pores using direct-write electrospinning," *Materials Letters*, vol. 93, pp. 397–400, 2013.
- [85] C. M. Vaz, S. van Tuijl, C. V. C. Bouten, and F. P. T. Baaijens, "Design of scaffolds for blood vessel tissue engineering using a multi-layering electrospinning technique," *Acta Biomaterialia*, vol. 1, no. 5, pp. 575–582, 2005.
- [86] M. Ignatova, N. Manolova, N. Markova, and I. Rashkov, "Electrospun non-woven nanofibrous hybrid mats based on chitosan and PLA for wound-dressing applications," *Macromolecular Bioscience*, vol. 9, no. 1, pp. 102–111, 2009.
- [87] T. G. Kim and T. G. Park, "Biodegradable polymer nanocylinders fabricated by transverse fragmentation of electrospun nanofibers through aminolysis," *Macromolecular Rapid Communications*, vol. 29, no. 14, pp. 1231–1236, 2008.
- [88] B. M. Baker, R. P. Shah, A. M. Silverstein, J. L. Esterhai, J. A. Burdick, and R. L. Mauck, "Sacrificial nanofibrous composites provide instruction without impediment and enable functional tissue formation," *Proceedings of the National Academy of Sciences of the United States of America*, vol. 109, no. 35, pp. 14176–14181, 2012.

## Research Article

# Enhanced Hydrophilicity and Protein Adsorption of Titanium Surface by Sodium Bicarbonate Solution

Shengnan Jia,<sup>1</sup> Yu Zhang,<sup>1</sup> Ting Ma,<sup>1</sup> Haifeng Chen,<sup>2</sup> and Ye Lin<sup>1</sup>

<sup>1</sup>Department of Implant Dentistry, School and Hospital of Stomatology, Peking University, Beijing 100081, China

<sup>2</sup>Department of Biomedical Engineering, College of Engineering, Peking University, Beijing 100871, China

Correspondence should be addressed to Ye Lin; [yorcklin@263.net](mailto:yorcklin@263.net)

Received 27 August 2015; Accepted 21 October 2015

Academic Editor: Daniel S. Oh

Copyright © 2015 Shengnan Jia et al. This is an open access article distributed under the Creative Commons Attribution License, which permits unrestricted use, distribution, and reproduction in any medium, provided the original work is properly cited.

The aim of this study was to investigate a novel and convenient method of chemical treatment to modify the hydrophilicity of titanium surfaces. Sand-blasted and acid-etched (SLA) titanium surfaces and machined titanium surfaces were treated with sodium bicarbonate ( $\text{NaHCO}_3$ ) solution. The wetting behavior of both kinds of surfaces was measured by water contact angle (WCA) test. The surface microstructure was assessed with scanning electron microscopy (SEM) and three-dimensional (3D) optical microscopy. The elemental compositions of the surfaces were analyzed by X-ray photoelectron spectroscopy (XPS). The protein adsorption analysis was performed with fibronectin. Results showed that, after 1 M  $\text{NaHCO}_3$  treatment, the hydrophilicity of both SLA and machined surfaces was enhanced. No significant microstructural change presented on titanium surfaces after  $\text{NaHCO}_3$  treatment. The deprotonation and ion exchange activities might cause the enhanced hydrophilicity of titanium surfaces. The increased protein adsorption of  $\text{NaHCO}_3$ -treated SLA surfaces might indicate their improved tissue-integration in clinical use.

## 1. Introduction

Titanium implant is widely used in dentistry because of its extraordinary biocompatibility and mechanical properties [1]. The tissue-integration of titanium surface plays a key role in the long-term clinical success. Different surface treatments that favor the bioactivity and bioconductivity of titanium implants have been investigated [2].

The interactions between titanium surface and host cells can be influenced by the surface characteristics of implants including topography, chemical properties, surface charge, and hydrophilicity [3]. The modification of Ti surfaces' topography is claimed to be influential to protein adsorption, osteoblast proliferation and differentiation, and tissue-integration [4].

Sand-blasted and acid-etched (SLA) Ti surface implants are widely used in clinical dental practice. This kind of surface is reported to have micro- and nanometer scale topography created by blasting and acid-etching processes. It was suggested that the topography of biomaterial surface in micro- or nanometer scale can promote higher cell-adhesion strengths [5].

Additionally, surface charge, surface energy, hydrophilicity, and other physicochemical properties of implant surfaces can also influence tissue-integration. In the last decade, interest in the hydrophilicity property of titanium surface has increased in both *in vitro* [6, 7] and *in vivo* [7, 8] studies. Most of these studies stated that hydrophilicity enhanced cell adhesion, proliferation and differentiation, and bone mineralization at an early stage [9, 10].

Hence, various techniques were attempted to increase the hydrophilicity of implant surfaces [11–14]. Nonetheless, these attempts of different techniques are argued to be either unpractical with high-standard technical requirements and rather long processing time or requiring severe chemical conditions, which, in clinical implantology, might probably impede the proposed application of the treated specimens.

Recently, a chemical treatment with NaOH has been reported to significantly improve the hydrophilicity of titanium surfaces [15, 16]. Performed by soaking the Ti discs or implants in 0.05 M NaOH for 30 s at room temperature, this treatment was reported to support fast and homogenous protein adsorption and consecutive osseointegration [15, 17].

Furthermore, it was also stated that enhanced surface energy by NaOH-induced hydrophilicity is responsible for the promotion of blood components adhesion [15] and cell adhesion to titanium surfaces [18]. NaOH-treated Ti implants were demonstrated with stronger osseointegrative potential *in vivo* as well [19]. Stadlinger et al. tested NaOH-treated and untreated implants in the mandible of an *in vivo* minipig model. By comparing the removal torque and interfacial stiffness, surfaces of NaOH-treated implants exhibited a tendency to promote early peri-implant bone formation [20].

Sodium bicarbonate ( $\text{NaHCO}_3$ ) solution is widely used as mouth-rinse in clinic for oral hygiene maintenance [21]. The aim of this study was to develop a mild alkali treatment method for preparing enhanced hydrophilic Ti implant surfaces. The experiment was designed for SLA and machined Ti implant surfaces to be treated with 1 M  $\text{NaHCO}_3$  solution. In this study, detailed physicochemical characterization of the  $\text{NaHCO}_3$ -treated Ti surfaces is presented as key findings. The influences of surface roughness and surface chemistry on the hydrophilicity transformations of the specimens were also evaluated. This evaluation was performed by measuring changes in the physicochemical properties of the Ti specimens with respect to chemical surface treatment and surface roughness. Fibronectin adsorption ability on  $\text{NaHCO}_3$ -treated SLA Ti surfaces was also investigated by comparing with untreated SLA Ti surfaces.

## 2. Materials and Methods

**2.1. Specimen Preparation.** Two types of Ti discs were employed as experiment specimens, which were machined and SLA Ti discs (Wego Jericom Biomaterials Co., Weihai, China). Both kinds of the discs have a diameter of 15 mm and a thickness of 1 mm. Machined Ti discs were made of commercially pure titanium that conformed with ISO 5832-2 grade 4 by milling process. As stated in the previous study [22], SLA discs were produced by sand-blasting machined Ti discs with  $\text{Al}_2\text{O}_3$  particles (particle size 250–500  $\mu\text{m}$ ) and then acid-etching the specimens in a boiling mixture of hydrochloric and sulphuric acid. Both discs were treated in nitric acid, deionised water, and air in sequence for them to be cleaned, rinsed, and dried correspondingly. At last, discs were stored in aluminum foil.

**2.2.  $\text{NaHCO}_3$  Solution Treatment.**  $\text{NaHCO}_3$  solution treatment was performed at room temperature. The SLA and machined Ti discs were assigned into three groups according to the difference in their chemical states, which were untreated (i.e., “untreated” group), treated with 1 M  $\text{NaHCO}_3$  solution (i.e., “ $\text{NaHCO}_3$ -treated” group), and treated with 1 M  $\text{NaHCO}_3$  solution and rinsed with Milli-Q water (Milli-Q Advantage, Millipore, France) for three times (i.e., “rinsed” group). Specimens in the untreated group maintain their original properties for further comparison. All specimens were then blow-dried in a nitrogen stream shortly before being measured.

**2.3. Surface Hydrophilicity Assessment.** The hydrophilicity of SLA and machined Ti discs in the untreated,

$\text{NaHCO}_3$ -treated and rinsed group was examined both quantitatively and qualitatively by water contact angle (WCA) test, which is formed by a 10  $\mu\text{L}$  drop of distilled water on the Ti surfaces. The measurement was performed by a contact angle system (OCA20, Dataphysics, Germany). All of the WCA data were obtained by ellipse methods. In this measurement process, specimens from both  $\text{NaHCO}_3$ -treated and rinsed group were further divided into 4 subgroups, each being soaked in  $\text{NaHCO}_3$  solution for 30 s, 1 min, 3 min, or 5 min, respectively. The average WCAs of the 4 samples in each subgroup were evaluated and then compared with each other and the ones in the untreated group. The subgroups were set up in order to observe the effects of soaking time on wetting behavior.

**2.4. Surface Microstructure Characterization.** In order to observe the microstructure of SLA and machined discs and to analyze what influences  $\text{NaHCO}_3$  treatment had on materials’ topography change, a scanning electron microscope (SEM) (S-3000N, Hitachi, Japan) and a three-dimensional (3D) optical microscope (Contour GT, Bruker, US) were utilized to analyze the specimens before and after a 3 min  $\text{NaHCO}_3$  treatment. A period of 3 minutes can be a suitable treatment time according to the results of the hydrophilicity assessment experiment (see Section 3.1 for details).

The SEM scanned specimens coated with gold at 15.0 kV and a magnification of 2000x. Surface roughness data and 3D images of the specimens were acquired by the 3D optical microscopy. Roughness data were then analyzed with Vision64 software. Four specimens from each group were evaluated by observing four random spots on each of them. The average values of their roughness average ( $R_a$ ), maximum peak height ( $R_p$ ), root mean square roughness ( $R_q$ ), and maximum height of the profile ( $R_t$ ) were hence calculated.

**2.5. Surfaces’ Elemental Composition.** An X-ray photoelectron spectroscopy (XPS) (ESCALAB 250 Xi, Thermo Scientific, US) that uses monochromatic  $\text{AlK}_\alpha$  radiation was employed to analyze surface elemental composition of the SLA specimens in three groups. Survey (wide-scan) spectra were recorded with a pass energy level of 100 eV and a resolution of 1.000 eV, while high-resolution (narrow-scan) spectra were obtained with a pass energy level of 30 eV and a resolution of 0.050 eV for C1 and O1. In each specimen group, three discs were tested. According to the methods suggested by McCafferty and Wightman, peak attribution and selection of full width at half maximum values were then executed to fit the high-resolution spectra [23]. All binding energies were checked in reference to the carbon C-H photopeak at 285.0 eV. High-resolution spectra for C1 and O1 were further analyzed using XPSPEAK 4.1 software.

**2.6. Protein Adsorption.** SLA specimens in both untreated and  $\text{NaHCO}_3$ -treated groups participated in this section. The  $\text{NaHCO}_3$ -treated specimens were immersed in the solution for 3 min. The treated specimens were carefully cleaned by a lint-free cleaning wipe to remove any residual solution and then blow-dried in a nitrogen stream.

TABLE 1: WCAs ( $^{\circ}$ ) after different treatment time for both SLA and machined specimens from three test groups: untreated,  $\text{NaHCO}_3$ -treated, and rinsed ( $n = 4$ , mean  $\pm$  SD).

	Untreated	$\text{NaHCO}_3$ -treated				Rinsed			
		30 s	1 min	3 min	5 min	30 s	1 min	3 min	5 min
SLA	$129.9 \pm 7.1$	$17.6 \pm 4.5$	$0.0 \pm 0.0$	$0.0 \pm 0.0$	$0.0 \pm 0.0$	$63.0 \pm 5.9$	$3.3 \pm 4.0$	$2.0 \pm 4.0$	$0.0 \pm 0.0$
Machined	$86.0 \pm 6.7$	$55.0 \pm 11.4$	$45.3 \pm 7.1$	$37.5 \pm 3.4$	$34.4 \pm 12.5$	$81.4 \pm 7.2$	$59.1 \pm 17.7$	$53.1 \pm 19.1$	$52.9 \pm 18.1$

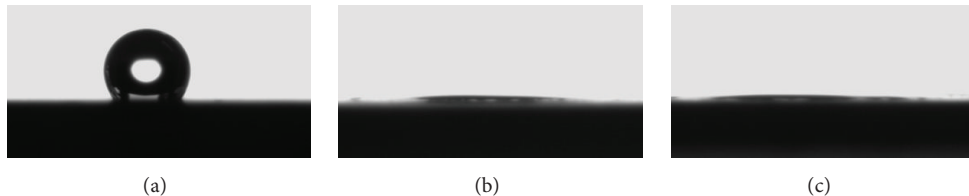


FIGURE 1: Image of a  $10 \mu\text{L}$  distilled water drop on (a) untreated, (b)  $\text{NaHCO}_3$ -treated (3 min), and (c) rinsed SLA discs. Untreated SLA disc (a) was hydrophobic, while  $\text{NaHCO}_3$ -treated SLA disc (b) was superhydrophilic as the observed WCA was close to 0. Rinsed SLA disc (c) maintained superhydrophilicity.

$1 \mu\text{M}$  fibronectin (HiLyte Fluor 488 labeled) solution was prepared in  $20 \text{ mM}$   $\text{NaCl}$ -buffer according to the instructions from HiLyte and was then directly applied in the experiments. Protein adsorption tests were executed with sandwich assay.  $10 \mu\text{L}$  of the protein solution was incubated between an SLA disk and a round-shaped microscopy glass cover slip with a diameter of  $12 \text{ mm}$  for  $5 \text{ min}$ . The process was carried out in a dark environment with saturated humidity at room temperature. Afterwards, the specimens were rinsed with  $20 \text{ mM}$   $\text{NaCl}$ -buffer for  $3$  times ( $5 \text{ min}$  each time) to remove loosely bound fibronectin on the SLA surfaces. Finally, specimens were analyzed using a confocal microscopy (LSM710, Zeiss, Germany) with an excitation wavelength of  $488 \text{ nm}$  and a cut off filter of  $505\text{--}550 \text{ nm}$  for detection. The adsorption of protein on the specimens was evaluated by measuring relative fluorescence intensity with the help from ImageJ (NIH, Bethesda, MD, USA) software.

**2.7. Statistical Analysis.** All data presented in this study are expressed as “mean  $\pm$  standard deviation (SD).” Data were subjected to an independent samples  $t$ -test or one-way ANOVA using SPSS 22.0 software for Mac. For analysis in this paper, significant differences were ones with a  $P < 0.05$ .

### 3. Results

**3.1. Surface Hydrophilicity Assessment.** The effects of surface energy changes were analyzed by measuring the WCAs on SLA and machined Ti surfaces. The rinsed group was arranged to clarify if the increased hydrophilicity of  $\text{NaHCO}_3$ -treated specimens was just temporary because of the adhesion of  $\text{Na}^+$  and negative ions ( $\text{OH}^-$ ,  $\text{HCO}_3^-$ ,  $\text{CO}_3^{2-}$ , etc.) on the specimen surfaces.

Figure 1 shows the WCAs of SLA surfaces under three states: untreated,  $\text{NaHCO}_3$ -treated for  $3 \text{ min}$ , and rinsed. According to Figure 1, the WCA of untreated SLA disc was obtuse. After  $\text{NaHCO}_3$  treatment, WCA was nearly 0. This angle was maintained after the disc being rinsed. Table 1 and

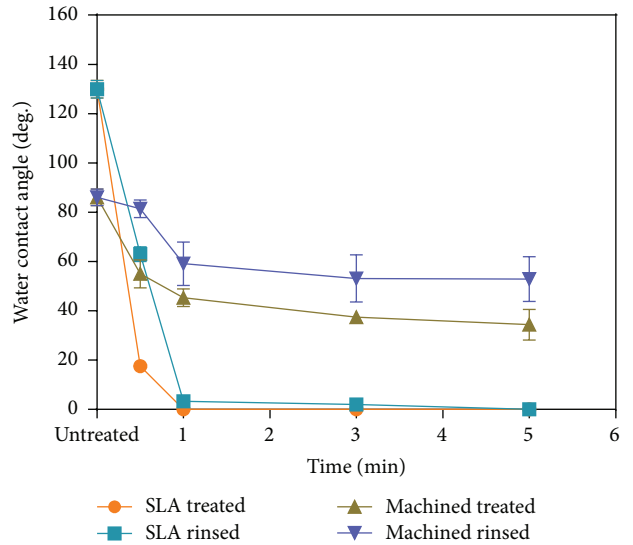


FIGURE 2: A plot of WCA ( $^{\circ}$ ) on both SLA and machined specimens  $\text{NaHCO}_3$ -treated at different time points with or without being rinsed. The WCAs of both SLA and machined specimens decreased with increasing treatment time. The WCAs of SLA specimens showed rapid decline. After  $1 \text{ min}$ , the WCAs of the  $\text{NaHCO}_3$ -treated and rinsed SLA specimens decreased to almost zero. The WCAs of machined surfaces displayed a relatively small decrement after  $\text{NaHCO}_3$  treatment and a slight increment after being rinsed.

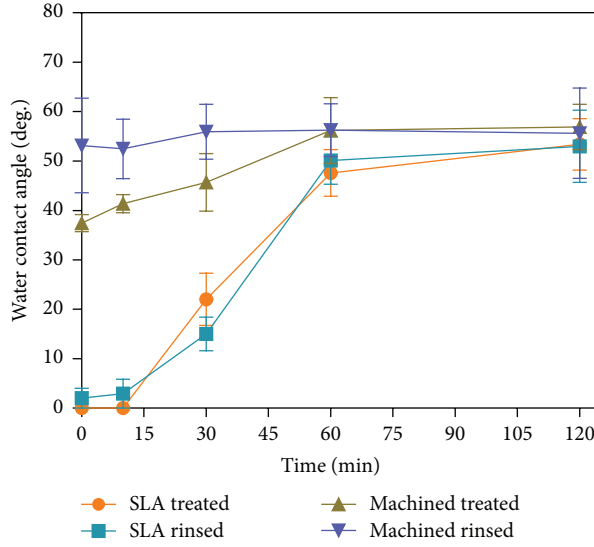
Figure 2 shows the WCAs of the SLA and machined specimens from three test groups with different chemical states. As evidenced by Table 1, the WCAs of untreated Ti specimens increased from  $86^{\circ}$  on the smooth machined surfaces to  $130^{\circ}$  on the SLA specimens. Therefore, untreated SLA specimens could be classified as hydrophobic. Also, it could be seen that the WCAs of both SLA and machined specimens decreased with increasing treatment time. However, while the machined surfaces had only displayed a relatively small decrement, data of SLA surfaces showed rapid decline, for a treatment time

TABLE 2: WCAs of SLA and machined specimens from three test groups, 0, 10, 30, 60, and 120 min of exposure in the air ( $n = 4$ , mean  $\pm$  SD).

Modification	0 min	10 min	30 min	60 min	120 min
SLA NaHCO <sub>3</sub> -treated	0.0 $\pm$ 0.0	0.0 $\pm$ 0.0	22.0 $\pm$ 10.6	47.6 $\pm$ 9.5	54.4 $\pm$ 10.4
SLA rinsed	2.0 $\pm$ 4.0	2.9 $\pm$ 5.8	15.0 $\pm$ 6.8	50.1 $\pm$ 9.6	53.0 $\pm$ 14.6
Machined NaHCO <sub>3</sub> -treated	37.5 $\pm$ 3.4	41.4 $\pm$ 3.7	45.7 $\pm$ 11.6	56.2 $\pm$ 13.3	56.9 $\pm$ 9.2
Machined rinsed	53.1 $\pm$ 19.1	52.5 $\pm$ 12.0	55.9 $\pm$ 11.1	56.3 $\pm$ 10.7	55.6 $\pm$ 18.3

TABLE 3: Roughness measurements of the untreated and NaHCO<sub>3</sub>-treated machined and SLA surfaces (mean  $\pm$  SD,  $n = 4$ ,  $\mu\text{m}$ ).

Modification	Machined				SLA			
	$R_a$	$R_p$	$R_q$	$R_t$	$R_a$	$R_p$	$R_q$	$R_t$
Untreated	0.15 $\pm$ 0.02	1.37 $\pm$ 0.19	0.20 $\pm$ 0.02	2.39 $\pm$ 0.29	2.04 $\pm$ 0.16	9.16 $\pm$ 1.33	2.58 $\pm$ 0.18	21.91 $\pm$ 3.55
NaHCO <sub>3</sub> -treated	0.14 $\pm$ 0.02	1.27 $\pm$ 0.15	0.19 $\pm$ 0.02	2.48 $\pm$ 0.26	2.09 $\pm$ 0.14	9.96 $\pm$ 1.66	2.65 $\pm$ 0.16	23.38 $\pm$ 3.57
$P$ values	0.108	0.123	0.258	0.356	0.335	0.145	0.264	0.249

FIGURE 3: Plot of WCA (°) on SLA and machined specimens from both the NaHCO<sub>3</sub>-treated and rinsed groups after different time exposed in the air. The value of WCAs increased with longer exposure time.

more than 1 min, and the WCAs of the NaHCO<sub>3</sub>-treated SLA specimens were recorded to be extremely close to zero. This change in hydrophilicity upon NaHCO<sub>3</sub> treatment shifted the SLA specimens from hydrophobic to superhydrophilic. Also, notice that by comparing the NaHCO<sub>3</sub>-treated and rinsed groups, it could be argued that the superhydrophilicity of NaHCO<sub>3</sub>-treated SLA specimens could be fully preserved after rinsing.

After 3 minutes of NaHCO<sub>3</sub> treatment and rinsing, the SLA and machined specimens were exposed in the air for 120 min, within which WCAs were measured again at different time points. Table 2 and Figure 3 show that the value of WCAs increased with longer exposure time. From the shown data, it can be concluded that the SLA specimens can remain superhydrophilic for at least 10 min.

**3.2. Surface Microstructure Characterization.** The SEM micrograph in Figure 4(a) illustrates the complex microstructure of an untreated SLA surface. Sand-blasting and acid-etching produced cavities and micropits were observed. Moreover, Figure 4(c) displays the profile of an untreated machined surface that exhibits less roughness. By comparing the SEM results of the untreated surfaces (Figures 4(a) and 4(c)) and the NaHCO<sub>3</sub>-treated surfaces (Figures 4(b) and 4(d)), it can be seen that both the SLA and machined Ti surfaces experienced no significant morphological differences before and after the NaHCO<sub>3</sub> treatment.

The 3D images in Figure 5 and the roughness data in Table 3 were both output from the 3D optical microscopy. 3D images display no apparent discrepancy between the untreated and NaHCO<sub>3</sub>-treated surfaces of both SLA and machined specimens. Similarly, the roughness measurements of the two surfaces before and after 3 min NaHCO<sub>3</sub> treatment in Table 3 demonstrate a more quantifiable version of this statement. A comparison can be made by observing Table 3. Mean  $R_a$  was 0.15  $\mu\text{m}$  for the untreated machined surfaces and 0.14  $\mu\text{m}$  for the NaHCO<sub>3</sub>-treated ones, while for the SLA surfaces mean  $R_a$  was 2.04  $\mu\text{m}$  before the treatment and 2.09  $\mu\text{m}$  after it.  $P$  values for both surfaces are larger than 0.05. Therefore, a conclusion can be reached that being treated with NaHCO<sub>3</sub> solution does not produce significant difference in the roughness of both machined and SLA specimens.

**3.3. Surface Elemental Composition Analysis.** Utilizing the XPS software, initially, the survey spectra were analyzed. Figures 6(a), 6(b), and 6(c) show the survey spectra of untreated, NaHCO<sub>3</sub>-treated, and rinsed SLA Ti surfaces, respectively. According to Figure 6(a), the survey spectra of the untreated SLA specimens consist of titanium (Ti), oxygen (O), and carbon (C) as main elements. While it is apparent in Figure 6(b) that, after NaHCO<sub>3</sub> treatment, sodium (Na) signal was detected as another main element, the other three main elements, O, C and Ti, all had a change in their substance amount rate (counts/s). However, Figure 6(c) does not

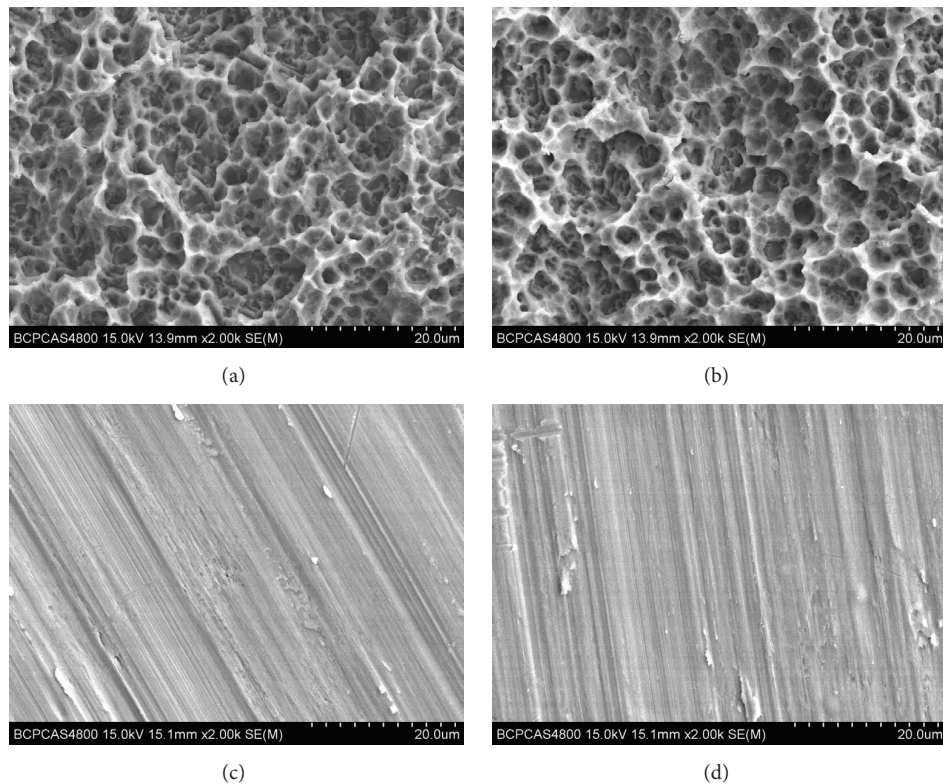


FIGURE 4: SEM of an SLA and a machined Ti surface in different chemical states: untreated SLA surface (a), NaHCO<sub>3</sub>-treated SLA surface (b), untreated machined surface (c), and NaHCO<sub>3</sub>-treated machined surface (d). (a) The microrough structure of an untreated SLA surface caused by sand-blasting and acid-etching and (b) the microstructure of the smooth surface of a machined Ti disc. By comparing the SEM results in (a, b) and (c, d), no significant morphological change of SLA and machined Ti surfaces could be observed before and after the NaHCO<sub>3</sub> treatment.

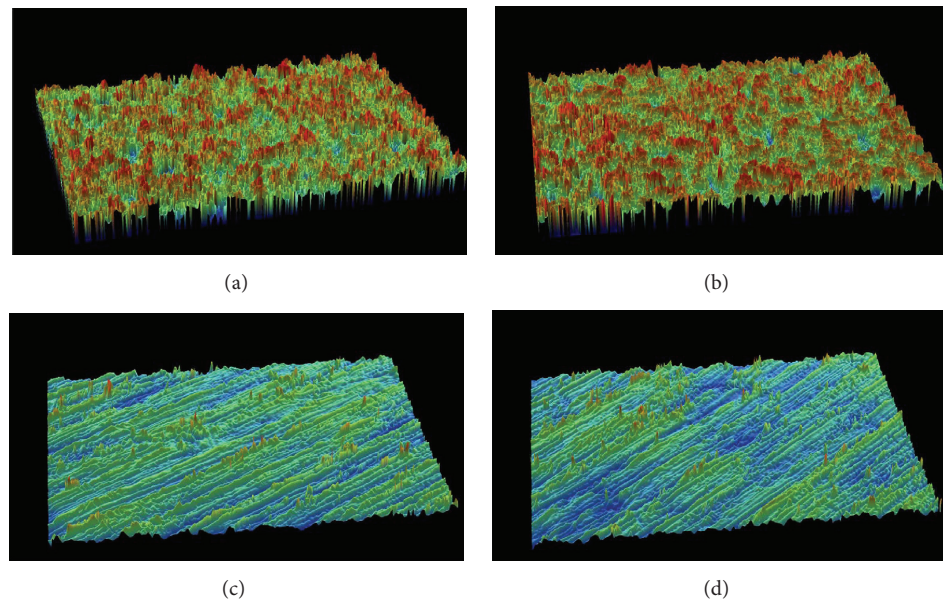


FIGURE 5: 3D images of an SLA and a machined surface generated by 3D optical microscopy in different chemical states: untreated SLA surface (a), NaHCO<sub>3</sub>-treated SLA surface (b), untreated machined surface (c), and NaHCO<sub>3</sub>-treated machined surface (d).

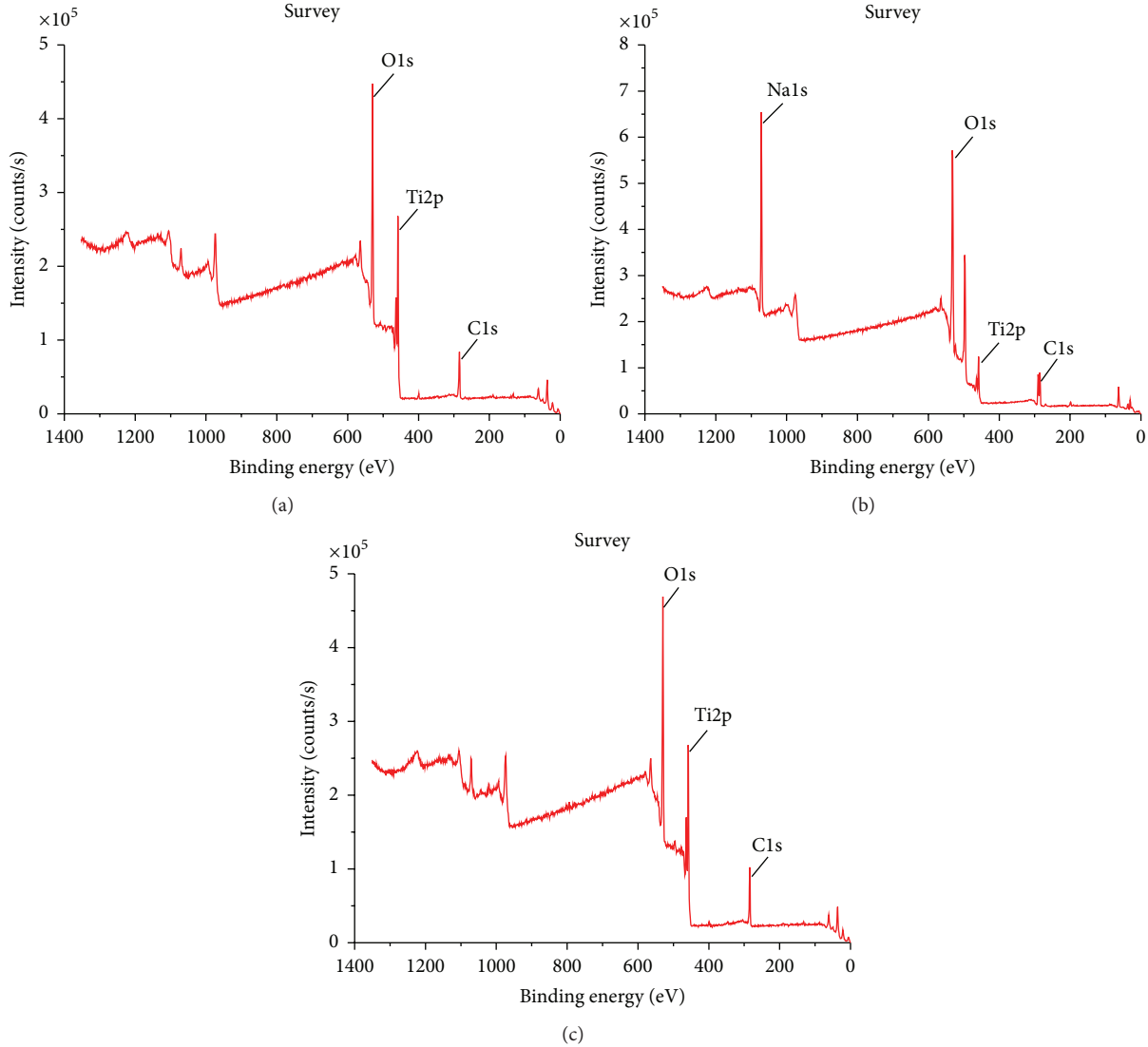


FIGURE 6: Survey spectra of untreated (a),  $\text{NaHCO}_3$ -treated (b), and rinsed (c) SLA specimens. (a) Titanium (Ti), oxygen (O), and carbon (C) were the main elements of untreated SLA specimens. From (b), sodium (Na) was detected as another main element on the tested specimens after  $\text{NaHCO}_3$  treatment. Compared with (a), (c) does not reflect any significant differences in elemental composition.

TABLE 4: Relative elemental compositions of untreated,  $\text{NaHCO}_3$ -treated, and rinsed SLA specimens, obtained from the survey spectra (%).

Modification	C	Ti	O	Na
Untreated	$33.2 \pm 3.9\%$	$19.4 \pm 1.8\%$	$47.2 \pm 2.1\%$	n.d.
$\text{NaHCO}_3$ -treated	$25.2 \pm 1.9\%$	$2.7 \pm 2.3\%$	$51.4 \pm 1.5\%$	$20.7 \pm 3.2\%$
Rinsed	$35.0 \pm 5.8\%$	$17.4 \pm 3.6\%$	$43.8 \pm 3.2\%$	$3.9 \pm 1.5\%$

reflect any significant differences in elemental composition between data of the untreated and rinsed groups. Based on the survey spectra, detailed elemental compositions of the surfaces are derived and recorded in Tables 4, 5, and 6.

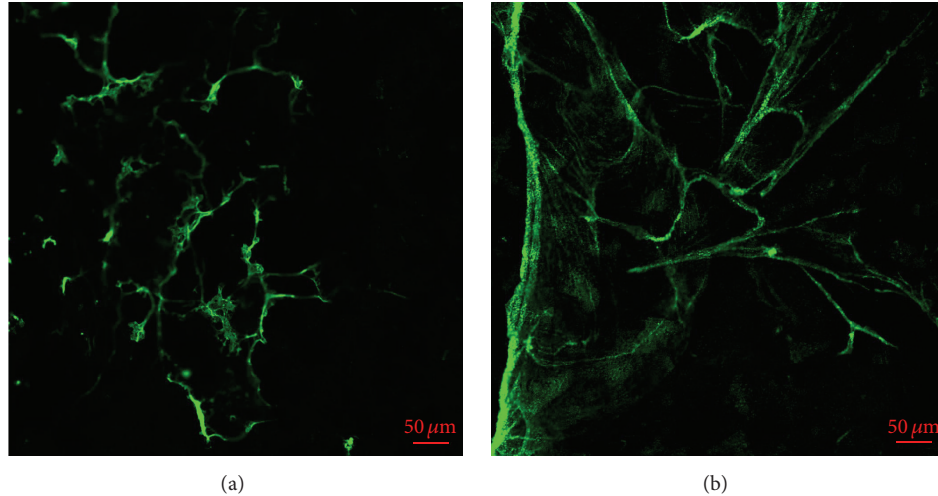
Table 4 represents the relative elemental compositions of three SLA surfaces groups. It was shown that the untreated group displayed an O/C ratio of 1.42 and a relative C content

TABLE 5: Relative elemental contributions to the C1s signal for untreated,  $\text{NaHCO}_3$ -treated, and rinsed SLA Ti specimens.

Modification	C-C	CO	$\text{CO}_2$ & $\text{CO}_3$
Untreated	$75.4 \pm 5.3\%$	$16.4 \pm 4.6\%$	$9.1 \pm 1.5\%$
$\text{NaHCO}_3$ -treated	$42.5 \pm 10.5\%$	$9.5 \pm 1.0\%$	$48.0 \pm 10.8\%$
Rinsed	$77.5 \pm 1.9\%$	$16.7 \pm 0.7\%$	$5.9 \pm 1.9\%$

TABLE 6: Relative elemental contributions to the O1s signal for untreated, NaHCO<sub>3</sub>-treated, and rinsed SLA Ti specimens.

Modification	TiO	C-O-C	OH	CO <sub>x</sub> /H <sub>2</sub> O
Untreated	69.7 ± 5.6%	9.3 ± 3.5%	18.0 ± 1.9%	2.9 ± 0.9%
NaHCO <sub>3</sub> -treated	20.1 ± 8.0%	17.0 ± 7.1%	45.2 ± 7.4%	17.7 ± 2.8%
Rinsed	76.0 ± 7.7%	9.5 ± 8.3%	11.3 ± 3.8%	3.2 ± 1.1%

FIGURE 7: Fluorescence micrograph of untreated (a) and NaHCO<sub>3</sub>-treated (b) SLA Ti discs after incubation in a 1 μM fibronectin for 5 min and subsequent washing steps. A larger amount of more uniformly distributed protein is showed in (b).

of 33.2%. After the NaHCO<sub>3</sub> treatment, the proportion of C content had decreased to 25.2% and the O/C ratio had increased to 2.04 as the proportion of O content had an increase of 4%. Data from the rinsed group showed no statistical difference compared to the ones from the untreated group.

CIs signals were considered to be contributed by aliphatic (C-C), ether and alcohol bound (CO), and carboxylate and carbonate bound (CO<sub>2</sub> and CO<sub>3</sub>) C. After these contributors were allocated, their contribution to the total C substance amount was derived and presented in Table 5. On the untreated SLA specimens, 75.4% of total C content was contributed by aliphatic, 16.4% by CO bound, and 9.1% by CO<sub>2</sub> or CO<sub>3</sub> bound C. In contrast, these data had, respectively, become 42.5% by aliphatic, 9.5% by CO bound, and 48.0% by CO<sub>2</sub> and CO<sub>3</sub> bound C after the NaHCO<sub>3</sub> treatment, demonstrating decrements in aliphatic, ether, and alcohol bound C but increments in CO<sub>2</sub> and CO<sub>3</sub> bound C. Data from the rinsed group and the untreated group again showed similarity.

On the other hand, O1s signals were provided by Ti bound O<sup>2-</sup> (TiO), oxygen bound to multiple carbon atoms (C-O-C), TiO<sub>2-x</sub> bound OH and OH<sup>-</sup> ions (OH), and also oxygen atoms multiple-bound to carbon and H<sub>2</sub>O (CO<sub>x</sub>/H<sub>2</sub>O). Notice that contributions from CO<sub>x</sub> and H<sub>2</sub>O were unable to be measured individually. Table 6 shows that 69.7% TiO<sub>2-x</sub> bound, 9.3% CO bound, 18.0% OH bound, and 2.9% CO<sub>x</sub> bound O were detected on the untreated SLA specimens while after the NaHCO<sub>3</sub> treatment, 20.1% TiO<sub>2-x</sub> bound,

17.0% CO bound, 45.2% OH bound, and 17.7% CO<sub>x</sub> bound O were recorded. In a word, the contribution from TiO<sub>2-x</sub> bound O was decreasing and, meanwhile, increments were discovered in the contribution of CO bound, OH bound, and CO<sub>x</sub> bound O.

**3.4. Protein Adsorption.** The differences of protein adsorption between untreated and NaHCO<sub>3</sub>-treated SLA Ti discs are showed in Figures 7 and 8. Figure 7 shows the fluorescence micrograph of the untreated and NaHCO<sub>3</sub>-treated SLA Ti discs after incubation in a 1 μM fibronectin for 5 min and subsequent washing steps. More protein adsorption was found in NaHCO<sub>3</sub>-treated SLA Ti disc compared to untreated group. Moreover, the protein adsorbed on NaHCO<sub>3</sub>-treated SLA disc was well-distributed. Fluorescence intensity can represent the relative amount of proteins adsorbed on Ti discs. From Figure 8, the fluorescence intensity of NaHCO<sub>3</sub>-treated SLA Ti discs was stronger than that of untreated group (mean fluorescence intensity of 0.122 compared with 0.065, resp.;  $P = 0.012$ ).

## 4. Discussion

**4.1. Influence of Superhydrophilicity on Osseointegration.** Titanium surfaces with WCA above 90° are considered as hydrophobic. On the contrary, WCAs lower than 90° categorize surfaces as hydrophilic, while WCAs too small to be almost neglected describe surfaces as having a superhydrophilic attribute [3]. As stated above, after 3 min of

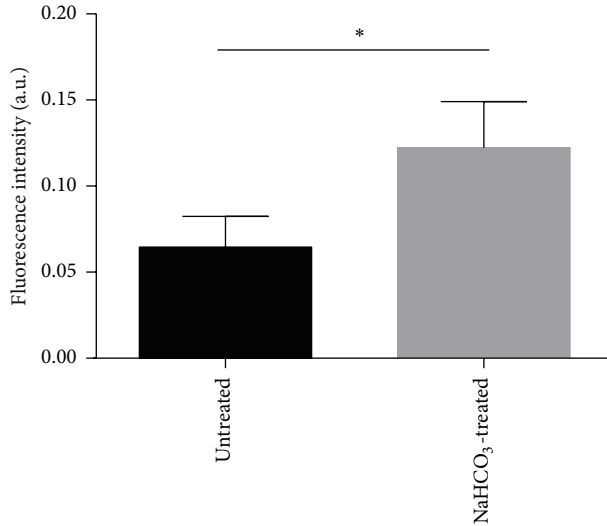


FIGURE 8: Average fluorescence intensity (a.u.) of adsorbed fibronectin on untreated and NaHCO<sub>3</sub>-treated SLA Ti surfaces. Fluorescence intensity of NaHCO<sub>3</sub>-treated SLA Ti discs was stronger than that of untreated group.

NaHCO<sub>3</sub> treatment, the WCAs of SLA discs were nearly 0° in this study, which subsequently transformed the material surface into superhydrophilic state.

Dental implants can be benefited by enhanced hydrophilic characteristic of surfaces due to better osseointegration performance. Ti implants with superhydrophilic surfaces were examined to have superb osseointegrative potential and raised much attention recently [24]. Early phases of osseointegration require osteogenic cells to primarily adhere to the implant surfaces and to further proliferate and differentiate into mature osteoblasts [25]. Hydrophilic surfaces support this process by promoting titanium to interact with cells, biological fluids, and tissues [8, 26]. For instance, cluster formation of osteoblasts as well as the expression of osteogenic genes can be enhanced by hydrophilic surfaces [17, 25, 27]. Superhydrophilic implants can optimize the osseointegration even more as they have proved useful to magnifying the area of bone-to-implant contact and strengthen mechanical fixation in the early healing processes of at least the first 4 weeks after implantation [8]. In this study, the NaHCO<sub>3</sub>-treated SLA discs had developed superhydrophilicity and been able to maintain it for 10 min. This characteristic indicates that, to apply NaHCO<sub>3</sub> treatment to the implants in clinic, there should be adequate time for clinicians to insert implants.

**4.2. Regime Behind the Development of Superhydrophilicity.** Wennerberg and Albrektsson stated that surfaces with smooth ( $S_a < 0.5 \mu\text{m}$ ) and minimal roughness ( $S_a 0.5\text{--}1 \mu\text{m}$ ) showed less strong bone responses than surfaces with higher roughness. Meanwhile, surfaces with moderate roughness ( $S_a 1\text{--}2 \mu\text{m}$ ) showed stronger bone responses than surfaces with high roughness ( $S_a > 2 \mu\text{m}$ ) in some studies [28]. In the presented experiment,  $R_a$  values were calculated for both SLA and machined surfaces to attempt to discover potential

influences of surface topography on hydrophilicity. The SLA surfaces showed a mean  $R_a$  value of about  $2 \mu\text{m}$ , which should be considered to be moderately rough.

It was claimed that microrough Ti surfaces induce more advanced initial hydrophobicity compared with Ti surfaces without microroughness [29]. The same results were discovered in this study. The mean WCAs of untreated SLA and machined specimens were 130° and 86°. On the other hand, on microrough titanium implant surfaces, which were not treated with any alkali, high WCAs are most likely to be caused by air entrapped in the micropores underneath the water droplets, according to the Cassie-Baxter regime [3]. However, for alkali treated microrough Ti specimens, the wetting behaviors were assumed by Tugulu et al. to be caused by a film regime [16]. The cavities of the microrough Ti specimens are supposed to be filled with wetting liquid due to capillary forces. Thus, this film regime is believed to be able to explain the low WCAs on NaHCO<sub>3</sub>-treated and rinsed SLA specimens.

Moreover, without any specific storage conditions, a thin passivation layer of TiO<sub>2-x</sub> is formed on untreated native Ti surfaces. However, this TiO<sub>2-x</sub> layer is observed to be rapidly contaminated by the hydrocarbons adsorption from the environment, which result in the hydrophobicity of Ti specimens and the repelling behaviors to water or biological fluids from tissues. The adsorption of hydrocarbons is considered to be able to change the osseointegrative potential of Ti implants [8, 11, 26]. Attempting to prevent this contamination, Rupp et al. have discovered that storing freshly prepared SLA Ti specimens in sodium chloride solution could significantly reduce the carbon contents on these superhydrophilic specimens to as low as 15%, while 35% of carbon was recorded on the hydrophobic SLA specimens which was stored normally [11]. The findings from these reports agree with the XPS results shown in this study. The reduction of carbon contents on NaHCO<sub>3</sub>-treated SLA surfaces may be regarded as a possible cause to explain the obtained hydrophilicity of NaHCO<sub>3</sub>-treated SLA Ti surfaces. However, this regime can yet explain the increased hydrophilicity of the rinsed group specimens whose carbon contents were at a rather high level with no difference with the untreated group.

According to high-resolution O1s signal of the NaHCO<sub>3</sub>-treated Ti specimens, TiO<sub>2-x</sub> bound OH and OH<sup>-</sup> ions were significantly increased after the treating process. It can be reasonably assumed that the existence of NaHCO<sub>3</sub> was the source of the OH<sup>-</sup> ions in the solution. Researchers had claimed the relationship between superhydrophilicity and the amount of these negative charged ions. For instance, superhydrophilicity of NaOH-treated SLA surfaces was indicated to be led by deprotonation and ion exchange of hydroxyl-groups on the TiO<sub>2-x</sub> surfaces [16]. Moreover, many studies demonstrated that the improvement of surface hydrophilicity was caused by forming of new oxygen-containing groups on the surface, such as -OH and -OOH, for these groups are hydrophilic [30]. Therefore, by concluding from comparing this study with other related literatures while taking the mild conditions of NaHCO<sub>3</sub> treatment protocol into account, one might assume that the formation of TiO<sub>2-x</sub> bound OH and OH<sup>-</sup> ions on Ti surfaces is one of the major chemical

transformations for the presented  $\text{NaHCO}_3$  treatment of Ti specimens. Also, it should be noticed that the results of SEM and roughness measurement in this study showed that there was no physical change in microstructure of the Ti specimens after  $\text{NaHCO}_3$  treatment.

**4.3. Protein Adsorption.** Fibronectin was tested in this study. Generally, fibronectin exists as a protein dimer and it can be discovered in 2 fundamental forms: soluble (component of blood plasma and other fluids) and insoluble (component of the extracellular matrix of various tissues) [31]. As a major adhesion protein of the extracellular matrix, it binds to membrane-spanning receptors (i.e., integrin) and to extracellular components [32]. Among many extracellular matrix proteins, fibronectin is an important protein that can contribute some insight into osteoblast cell differentiation, cell-cell interactions, and cell-matrix interactions [33]. Therefore, this protein was chosen to be involved in this study.

An osteoblast adhesion process consists of protein adsorption, cell interaction with the adsorbed proteins, cell attachment, and spreading on implant surfaces. This process plays an essential part of osseointegration [34].

Observing from Figure 8, the fluorescence intensity of  $\text{NaHCO}_3$ -treated specimens was significantly higher than untreated specimens, indicating that more fibronectin was adsorbed on hydrophilic  $\text{NaHCO}_3$ -treated specimens. This result agrees with some previous researches, which showed increased protein adsorption on hydrophilic specimens [35–37]. Protivínský et al. described continuously increasing fibronectin adsorption on highly hydrophilic surfaces treated by a high-temperature and high-concentration  $\text{NaOH}$  solution [35]. Milleret et al. found  $\text{NaOH}$  treated SLA Ti surfaces to partially heparinize whole human blood. Unstructured and discontinuous fibrinogen aggregates were observed on untreated group in their study, while a much denser mesh of fibrin fibers was recorded on  $\text{NaOH}$  treated group [15]. The initial binding of proteins relies on the physicochemical features of a surface, such as roughness, surface energy, and chemical composition [36, 38, 39]. The topographic features of the surfaces have particular consequences in terms of hydrophilicity. Before  $\text{NaHCO}_3$  treatment, microrough SLA Ti discs were hydrophobic. According to the Cassie-Baxter regime [3], the presence of air entrapment in the micropores on hydrophobic surfaces resists the contact of the solution which could have a negative effect of the surface contact area in the rough surfaces, inhibiting protein adsorption [39]. After  $\text{NaHCO}_3$  treatment, superhydrophilic SLA Ti surfaces were supposed to be filled with protein solution, which can increase the surface-protein contact area. Moreover, it is assumed by Rupp et al. that a higher surface free energy initiates the adsorption of proteins [11]. Supporting this assumption, studies have proved that SLA Ti specimens stored freshly in sodium chloride solution, as mentioned above, which exhibits a higher surface free energy, do significantly increase human plasma fibronectin adsorption [37]. Therefore, it is reasonable to consider that, after  $\text{NaHCO}_3$  treatment, higher surface free energy of SLA Ti surfaces also facilitated the adsorption of fibronectin.

However, some previous studies showed that proteins tended to be adsorbed more extensively on hydrophobic surfaces [40, 41]. This disagreement between the protein adsorption results from different studies may be caused by the usage of a variety of proteins with different molecular properties and surfaces with different topographic features, while it still needs further research to investigate how protein types, surface roughness, and wettability affect protein adsorption.

The distribution feature of fibronectin on untreated and  $\text{NaHCO}_3$ -treated surfaces was revealed with a significant difference in this study. The reasons behind this difference were also worth discussion. It is claimed that ionic strength of local environment takes active part in determining fibronectin's molecular shape. That is to say, with increased ionic strength, fibronectin may display a more stretched distribution form [38]. In this study, the fibronectin spread to a more extended form on  $\text{NaHCO}_3$  discs, which were supposed to possess a higher ionic strength compared to untreated discs.

The adsorption of proteins on implant surfaces is essential because it can affect the early biological response of the surrounding microenvironment, which has an effect on the healing process as well as the final clinical outcomes of implants [42, 43]. Rivera-Chacon et al. proved this point by finding that increased cell attachment and proliferative capacity occurred on titanium surfaces with more fibronectin adsorption [44]. It was also evidenced that the alkali-treated implants on acid-etched surfaces are able to promote secondary stability in an earlier phases of implant site healing in dog experiments compared with the untreated implants [45]. Moreover, Held et al. recorded the results of alkali treated blasted and acid-etched implants in a series of clinical cases [46]. In their study, a number of blasted and acid-etched implants were placed in a group of patients with compromised bone density. Concluding from these experiments, the implants exhibited good stability quotient as well as vertical bone volume for at least 1 year after loading.

**4.4. General Discussion on Modification of Ti Surface by Alkali Treatment.** As  $\text{NaHCO}_3$  solution is weakly alkaline, Ti surfaces treated with  $\text{NaHCO}_3$  solution are expected to be able to generate similar effects to ones treated with  $\text{NaOH}$  solution. The results of hydrophilicity and physicochemical changes in this study were similar to those treated with  $\text{NaOH}$  solution [16]. However, some reports claimed that osteogenic differentiation of osteoprogenitor cells could be affected adversely by excessive alkalinization in the microenvironment of tissue-engineered constructs. Monfoulet et al. measured the range of usable pH values for alkalis with culture of bone marrow-derived mesenchymal stem cells (hBMSC). They have observed that there was no cell proliferation at pH 8.85 and there were dead cells at pH 9.37. In contrast, cell proliferation was uninfluenced by alkaline that has a pH less than 8.27 [47]. Compared to 0.05 M  $\text{NaOH}$  (pH 12.7), 1 M  $\text{NaHCO}_3$  solution (pH 8.1) has a pH value closer to the one of human body fluid (pH 7.35–7.45). In addition,  $\text{HCO}_3^-$  is one of the buffer components in blood and body fluid.  $\text{NaHCO}_3$  is considered to be more suitable for this application because of its relatively weak alkalinity and ease

of preparation. Thus, the authors proposed an assumption that  $\text{NaHCO}_3$  solution may be a more optimized alternative to  $\text{NaOH}$  solution for the application of dental implants. To examine this hypothesis, future efforts are required.

Further researches should be proposed to firstly evaluate other characteristics of  $\text{NaHCO}_3$ -treated SLA Ti surfaces, such as blood component adhesion, cell adhesion, osseointegrative potential, and influences on bone formation. Further, as stated above, differences in the biocompatibility of  $\text{NaHCO}_3$  and  $\text{NaOH}$  solution should be evaluated. Lastly, the authors believe it is also worth to examine that, apart from  $\text{NaOH}$  and  $\text{NaHCO}_3$  solution, whether other kinds of alkaline solution are suitable for being applied in similar Ti surface treatments.

## 5. Conclusions

This study describes and evaluates a novel, simple, and convenient method to enhance hydrophilicity of Ti surfaces with  $\text{NaHCO}_3$  solution. It was discovered that superhydrophilicity of SLA Ti surfaces can be obtained by reversible deprotonation and ion exchange processes. In addition, increased protein adsorption on  $\text{NaHCO}_3$ -treated specimens was also observed and evaluated. In conclusion, this  $\text{NaHCO}_3$  treatment is a reliable method for enhancing the hydrophilicity and protein adsorption of SLA Ti surfaces. It was also proposed that due to the simplicity and biocompatibility of  $\text{NaHCO}_3$ ,  $\text{NaHCO}_3$  treatment might be considered as a clinically viable strategy to render superhydrophilicity to Ti specimens in the site of implantation without requirements for modifying manufacturing or storage methods of the implants. The influences on a Ti surface's cell adhesion, cell proliferation, differentiation, and so forth after  $\text{NaHCO}_3$ -treated will be addressed in our following studies. Moreover, the effects of  $\text{NaHCO}_3$  treatment on osseointegration should also be evaluated in future researches.

## Conflict of Interests

The authors claim no conflict of interests.

## Authors' Contribution

Shengnan Jia and Yu Zhang contributed equally to this work.

## Acknowledgments

This study was supported by a grant from the National Basic Research Program of China (973 Program, 2012CB933900). Titanium specimens were provided by Wego (Wego Jericom Biomaterials Co., Weihai, China). Technical assistance of engineer Mr. Jishu Yin (Wego Jericom Biomaterials Co., Weihai, China) is gratefully acknowledged.

## References

- [1] F. J. Gil, N. Manzanares, A. Badet, C. Aparicio, and M.-P. Ginebra, "Biomimetic treatment on dental implants for short-term bone regeneration," *Clinical Oral Investigations*, vol. 18, no. 1, pp. 59–66, 2014.
- [2] Y. Förster, C. Rentsch, W. Schneiders et al., "Surface modification of implants in long bone," *Biomatter*, vol. 2, no. 3, pp. 149–157, 2012.
- [3] F. Rupp, R. A. Gittens, L. Scheideler et al., "A review on the wettability of dental implant surfaces I: theoretical and experimental aspects," *Acta Biomaterialia*, vol. 10, no. 7, pp. 2894–2906, 2014.
- [4] K. Anselme, M. Bigerelle, B. Nol, A. Iost, and P. Hardouin, "Effect of grooved titanium substratum on human osteoblastic cell growth," *Journal of Biomedical Materials Research*, vol. 60, no. 4, pp. 529–540, 2002.
- [5] A. Canabarro, C. G. Paiva, H. T. Ferreira et al., "Short-term response of human osteoblast-like cells on titanium surfaces with micro- and nano-sized features," *Scanning*, vol. 34, no. 6, pp. 378–386, 2012.
- [6] J. H. Park, C. E. Wasilewski, N. Almodovar et al., "The responses to surface wettability gradients induced by chitosan nanofilms on microtextured titanium mediated by specific integrin receptors," *Biomaterials*, vol. 33, no. 30, pp. 7386–7393, 2012.
- [7] R. A. Gittens, R. Olivares-Navarrete, A. Cheng et al., "The roles of titanium surface micro/nanotopography and wettability on the differential response of human osteoblast lineage cells," *Acta Biomaterialia*, vol. 9, no. 4, pp. 6268–6277, 2013.
- [8] D. Buser, N. Broggini, M. Wieland et al., "Enhanced bone apposition to a chemically modified SLA titanium surface," *Journal of Dental Research*, vol. 83, no. 7, pp. 529–533, 2004.
- [9] C. Eriksson, H. Nygren, and K. Ohlson, "Implantation of hydrophilic and hydrophobic titanium discs in rat tibia: cellular reactions on the surfaces during the first 3 weeks in bone," *Biomaterials*, vol. 25, no. 19, pp. 4759–4766, 2004.
- [10] M. M. Bornstein, P. Valderrama, A. A. Jones, T. G. Wilson, R. Seibl, and D. L. Cochran, "Bone apposition around two different sandblasted and acid-etched titanium implant surfaces: a histomorphometric study in canine mandibles," *Clinical Oral Implants Research*, vol. 19, no. 3, pp. 233–241, 2008.
- [11] F. Rupp, L. Scheideler, N. Olshanska, M. de Wild, M. Wieland, and J. Geis-Gerstorfer, "Enhancing surface free energy and hydrophilicity through chemical modification of microstructured titanium implant surfaces," *Journal of Biomedical Materials Research Part A*, vol. 76, no. 2, pp. 323–334, 2006.
- [12] H. Aita, N. Hori, M. Takeuchi et al., "The effect of ultraviolet functionalization of titanium on integration with bone," *Biomaterials*, vol. 30, no. 6, pp. 1015–1025, 2009.
- [13] B. Feng, J. Weng, B. C. Yang, S. X. Qu, and X. D. Zhang, "Characterization of surface oxide films on titanium and adhesion of osteoblast," *Biomaterials*, vol. 24, no. 25, pp. 4663–4670, 2003.
- [14] K. Duske, I. Koban, E. Kindel et al., "Atmospheric plasma enhances wettability and cell spreading on dental implant metals," *Journal of Clinical Periodontology*, vol. 39, no. 4, pp. 400–407, 2012.
- [15] V. Milleret, S. Tugulu, F. Schlottig, and H. Hall, "Alkali treatment of microrough titanium surfaces affects macrophage/monocyte adhesion, platelet activation and architecture of blood clot

- formation," *European Cells and Materials*, vol. 21, pp. 430–444, 2011.
- [16] S. Tugulu, K. Löwe, D. Scharnweber, and F. Schlottig, "Preparation of superhydrophilic microrough titanium implant surfaces by alkali treatment," *Journal of Materials Science: Materials in Medicine*, vol. 21, no. 10, pp. 2751–2763, 2010.
- [17] S. Hamlet, M. Alfarsi, R. George, and S. Ivanovski, "The effect of hydrophilic titanium surface modification on macrophage inflammatory cytokine gene expression," *Clinical Oral Implants Research*, vol. 23, no. 5, pp. 584–590, 2012.
- [18] M. Al Mustafa, H. Agis, H. D. Muller, G. Watzek, and R. Gruber, "In vitro adhesion of fibroblastic cells to titanium alloy discs treated with sodium hydroxide," *Clinical Oral Implants Research*, vol. 26, no. 1, pp. 15–19, 2015.
- [19] J. L. Calvo-Guirado, A. J. Ortiz-Ruiz, B. Negri, L. López-Marí, C. Rodriguez-Barba, and F. Schlottig, "Histological and histomorphometric evaluation of immediate implant placement on a dog model with a new implant surface treatment," *Clinical Oral Implants Research*, vol. 21, no. 3, pp. 308–315, 2010.
- [20] B. Stadlinger, S. J. Ferguson, U. Eckelt et al., "Biomechanical evaluation of a titanium implant surface conditioned by a hydroxide ion solution," *British Journal of Oral and Maxillofacial Surgery*, vol. 50, no. 1, pp. 74–79, 2012.
- [21] J. Pratten, J. Wiecek, N. Mordan et al., "Physical disruption of oral biofilms by sodium bicarbonate: an *in vitro* study," *International Journal of Dental Hygiene*, 2015.
- [22] T. Ma, X. Ge, S. Jia, X. Jiang, Y. Zhang, and Y. Lin, "The influence of titanium surfaces treated by alkalis on macrophage and osteoblast-like cell adhesion and gene expression *in vitro*," *RSC Advances*, vol. 5, no. 99, pp. 81378–81387, 2015.
- [23] E. McCafferty and J. P. Wightman, "Determination of the concentration of surface hydroxyl groups on metal oxide films by a quantitative XPS method," *Surface and Interface Analysis*, vol. 26, no. 8, pp. 549–564, 1998.
- [24] F. Schwarz, M. Wieland, Z. Schwartz et al., "Potential of chemically modified hydrophilic surface characteristics to support tissue integration of titanium dental implants," *Journal of Biomedical Materials Research Part B: Applied Biomaterials*, vol. 88, no. 2, pp. 544–557, 2009.
- [25] Z. Qu, X. Rausch-Fan, M. Wieland, M. Matejka, and A. Schedle, "The initial attachment and subsequent behavior regulation of osteoblasts by dental implant surface modification," *Journal of Biomedical Materials Research Part A*, vol. 82, no. 3, pp. 658–668, 2007.
- [26] G. Zhao, Z. Schwartz, M. Wieland et al., "High surface energy enhances cell response to titanium substrate microstructure," *Journal of Biomedical Materials Research Part A*, vol. 74, no. 1, pp. 49–58, 2005.
- [27] J. Vlacic-Zischke, S. M. Hamlet, T. Friis, M. S. Tonetti, and S. Ivanovski, "The influence of surface microroughness and hydrophilicity of titanium on the up-regulation of TGF $\beta$ /BMP signalling in osteoblasts," *Biomaterials*, vol. 32, no. 3, pp. 665–671, 2011.
- [28] A. Wennerberg and T. Albrektsson, "Effects of titanium surface topography on bone integration: a systematic review," *Clinical Oral Implants Research*, vol. 20, supplement 4, pp. 172–184, 2009.
- [29] F. Rupp, L. Scheideler, D. Rehbein, D. Axmann, and J. Geis-Gerstorfer, "Roughness induced dynamic changes of wettability of acid etched titanium implant modifications," *Biomaterials*, vol. 25, no. 7–8, pp. 1429–1438, 2004.
- [30] J. Lai, B. Sunderland, J. Xue et al., "Study on hydrophilicity of polymer surfaces improved by plasma treatment," *Applied Surface Science*, vol. 252, no. 10, pp. 3375–3379, 2006.
- [31] S. Cei, D. Karapetsa, E. Aleo, and F. Graziani, "Protein adsorption on a laser-modified titanium implant surface," *Implant Dentistry*, vol. 24, pp. 134–141, 2015.
- [32] M. Gorbahn, M. O. Klein, M. Lehner et al., "Promotion of osteogenic cell response using quasicovalent immobilized fibronectin on titanium surfaces: introduction of a novel biomimetic layer system," *Journal of Oral and Maxillofacial Surgery*, vol. 70, no. 8, pp. 1827–1834, 2012.
- [33] A. M. Moursi, C. H. Damsky, J. Lull et al., "Fibronectin regulates calvarial osteoblast differentiation," *Journal of Cell Science*, vol. 109, part 6, pp. 1369–1380, 1996.
- [34] K. Anselme, "Osteoblast adhesion on biomaterials," *Biomaterials*, vol. 21, no. 7, pp. 667–681, 2000.
- [35] J. Protivinský, M. Appleford, J. Strnad, A. Helebrant, and J. L. Ong, "Effect of chemically modified titanium surfaces on protein adsorption and osteoblast precursor cell behavior," *International Journal of Oral and Maxillofacial Implants*, vol. 22, no. 4, pp. 542–550, 2007.
- [36] N. Hori, T. Ueno, H. Minamikawa et al., "Electrostatic control of protein adsorption on UV-photofunctionalized titanium," *Acta Biomaterialia*, vol. 6, no. 10, pp. 4175–4180, 2010.
- [37] L. Scheideler, F. Rupp, M. Wieland, and J. Geis-Gerstorfer, "Storage conditions of titanium implants influence molecular and cellular interactions," Scientific Poster, 2005.
- [38] D. E. MacDonald, B. Markovic, M. Allen, P. Somasundaran, and A. L. Boskey, "Surface analysis of human plasma fibronectin adsorbed to commercially pure titanium materials," *Journal of Biomedical Materials Research*, vol. 41, no. 1, pp. 120–130, 1998.
- [39] W. Song and J. F. Mano, "Interactions between cells or proteins and surfaces exhibiting extreme wettabilities," *Soft Matter*, vol. 9, no. 11, pp. 2985–2999, 2013.
- [40] P. Roach, N. J. Shirtcliffe, D. Farrar, and C. C. Perry, "Quantification of surface-bound proteins by fluorometric assay: comparison with quartz crystal microbalance and amido black assay," *The Journal of Physical Chemistry B*, vol. 110, no. 41, pp. 20572–20579, 2006.
- [41] J. Zimmermann, M. Rabe, D. Verdes, and S. Seeger, "Functionalized silicone nanofilaments: a novel material for selective protein enrichment," *Langmuir*, vol. 24, no. 3, pp. 1053–1057, 2008.
- [42] A. Mata, X. Su, A. J. Fleischman et al., "Osteoblast attachment to a textured surface in the absence of exogenous adhesion proteins," *IEEE Transactions on Nanobioscience*, vol. 2, no. 4, pp. 287–294, 2003.
- [43] V. Grigoriou, I. M. Shapiro, E. A. Cavalcanti-Adam, R. J. Composto, P. Ducheyne, and C. S. Adams, "Apoptosis and survival of osteoblast-like cells are regulated by surface attachment," *Journal of Biological Chemistry*, vol. 280, no. 3, pp. 1733–1739, 2005.
- [44] D. M. Rivera-Chacon, M. Alvarado-Velez, C. Y. Acevedo-Morantes et al., "Fibronectin and vitronectin promote human fetal osteoblast cell attachment and proliferation on nanoporous titanium surfaces," *Journal of Biomedical Nanotechnology*, vol. 9, no. 6, pp. 1092–1097, 2013.
- [45] J. Strnad, K. Urban, C. Povysil, and Z. Strnad, "Secondary stability assessment of titanium implants with an alkali-etched

- surface: a resonance frequency analysis study in beagle dogs,” *International Journal of Oral and Maxillofacial Implants*, vol. 23, no. 3, pp. 502–512, 2008.
- [46] U. Held, D. Rohner, and D. Rothamel, “Early loading of hydrophilic titanium implants inserted in low-mineralized (D3 and D4) bone: one year results of a prospective clinical trial,” *Head and Face Medicine*, vol. 9, article 37, 2013.
- [47] L.-E. Monfoulet, P. Becquart, D. Marchat et al., “The pH in the microenvironment of human mesenchymal stem cells is a critical factor for optimal osteogenesis in tissue-engineered constructs,” *Tissue Engineering Part A*, vol. 20, no. 13-14, pp. 1827–1840, 2014.

## Research Article

# UV Photocatalysis of Bone Marrow-Derived Macrophages on TiO<sub>2</sub> Nanotubes Mediates Intracellular Ca<sup>2+</sup> Influx via Voltage-Gated Ca<sup>2+</sup> Channels

Seunghan Oh,<sup>1</sup> Eun-Joo Choi,<sup>2</sup> Munkhsoyol Erkhembaatar,<sup>3</sup> and Min Seuk Kim<sup>3</sup>

<sup>1</sup>Department of Dental Biomaterials and Institute of Biomaterials-Implant, College of Dentistry, Wonkwang University, Iksan, Jeonbuk 570-749, Republic of Korea

<sup>2</sup>Department of Oral and Maxillofacial Surgery, College of Dentistry, Wonkwang University, Iksan, Jeonbuk 570-749, Republic of Korea

<sup>3</sup>Department of Oral Physiology and Institute of Biomaterial-Implant, College of Dentistry, Wonkwang University, Iksan, Jeonbuk 570-749, Republic of Korea

Correspondence should be addressed to Min Seuk Kim; happy1487@wku.ac.kr

Received 1 April 2015; Revised 18 May 2015; Accepted 18 May 2015

Academic Editor: Ramaswamy Narayanan

Copyright © 2015 Seunghan Oh et al. This is an open access article distributed under the Creative Commons Attribution License, which permits unrestricted use, distribution, and reproduction in any medium, provided the original work is properly cited.

Titanium (Ti) possesses excellent properties for use in dental implants but has low osteogenic surface properties that result in limiting rapid osseointegration. The physiological interaction between the surface of the implant material and bone cells, especially osteoclasts, is a crucial factor in determining successful osseointegration. However, the details of such an interaction remain elusive. Here, we demonstrated that nanotopography on the Ti surface is a crucial factor for modulating intracellular signal transduction in bone marrow-derived macrophages (BMMs). To define this, intracellular Ca<sup>2+</sup> and ROS were simultaneously measured in BMMs that were seeded on polished Ti and TiO<sub>2</sub> nanotubes. We found that UV photocatalysis of TiO<sub>2</sub> immediately elicits intracellular calcium concentration ([Ca<sup>2+</sup>]<sub>i</sub>) increase and intracellular reactive oxygen species concentration ([ROS]<sub>i</sub>) reduction in cells on TiO<sub>2</sub> nanotubes. UV photocatalysis-mediated [Ca<sup>2+</sup>]<sub>i</sub> increase is dependent on extracellular and intracellular ROS generation. Furthermore, extracellular Ca<sup>2+</sup> influx through voltage-gated calcium channels (VGCCs) is critical for the UV photocatalysis-mediated [Ca<sup>2+</sup>]<sub>i</sub> increase, while phospholipase C (PLC) activation is not required. Considering the physiological roles of Ca<sup>2+</sup> signaling in BMMs and osteoclastogenesis, nanotopography on the Ti surface should be considered an important factor that can influence successful dental implantation.

## 1. Introduction

Titanium (Ti) and its alloys are well known to be one of primary metallic biomaterials used in dental and orthopedic implants requiring load-bearing capacity and feature excellent chemical resistance and considerable strength. However, due to the strong chemical stability of Ti and Ti alloys resulting in excellent biocompatibility, they have limited chemical and biological responses, which can react directly with bone forming related cells and is required for rapid osseointegration and strong fixation in the patient [1, 2]. Many researchers have sought to develop various surface treatment of Ti implant in order to create an excellent chemical and biological reactivity to the surface of Ti [3–6].

Osseointegration is determined by numerous factors linked to the host (bone remodeling) and to the implant materials (surface properties). The former is mainly regulated by cell-to-cell interactions between osteoblasts, which deposit bone matrix, and osteoclasts, which resorb bone tissue [7]. In particular, modified osteoclastogenesis or activities of mature osteoclasts cause severe bone disorders and result in poor osseointegration [7]. In the latter case, the surface topography of the implant plays a critical role in the clinical success of bone-anchored implants [8]. Surface physicochemical treatments modifying implant surface chemistry and topography are commonly employed to improve osseointegration of the implant [9–11]. Many studies about biochemical surface modification of Ti report enhanced osseointegration of the Ti

surface, depending on surface roughness, bioactive coating, and varied mixture methods. Particularly, many researchers have analyzed that micro surface roughness and morphology were related to the bone contact, primary stability, and intermittent load bearing *in vitro* and *in vivo* [12–18].

Nanotopography, as well as microstructures, has been of great interest in the implant field due to the high surface-to-volume ratio, excellent bone cell behavior, and osseointegration capabilities [19–21]. In the field of *in vitro* molecular biology, it was reported that cellular behavior and functionality were affected by the size of topographical environment [22–25]. Titania ( $\text{TiO}_2$ ) nanotubes have been widely studied in the fields of photocatalysis/photoelectrolysis [26–30], water purification [31, 32], solar cells [33–37], and biomedical engineering [38–42]. In particular, the surface structure on vertically aligned  $\text{TiO}_2$  nanotubes had an important effect on improving the *in vitro* proliferation and mineralization of osteoblasts [43–45], reducing immune response [46], and upregulating *in vivo* osseointegration [20, 43]. In this study, we demonstrate that altered UV photocatalytic activity by surface modification of Ti resulted in the transmission of intracellular signals by mobilizing secondary messengers such as  $\text{Ca}^{2+}$  and ROS in BMMs.

## 2. Materials and Methods

**2.1. Cell Culture and Reagents.** Primary bone marrow-derived macrophages (BMMs) were cultured in alpha-modified minimum essential medium ( $\alpha$ -MEM; Sigma-Aldrich, MO, USA) supplemented with 10% fetal bovine serum (FBS) and M-CSF (30 ng/mL). Soluble recombinant mouse receptor activator of nuclear factor kappa-beta ligand (RANKL) and macrophage colony-stimulating factor (M-CSF) were purchased from KOMA Biotech (Seoul, Korea). N-Acetyl-L-cysteine (NAC), U73122, nicardipine, Fura-2-acetoxymethyl ester (Fura-2/AM) and 5-(and-6)-chloromethyl-2',7'-dichlorodihydrofluorescein diacetate, and acetyl ester (CM-H<sub>2</sub>DCFDA) were purchased from Sigma Aldrich (MO, USA).

**2.2. Fabrication of  $\text{TiO}_2$  Nanotubes.**  $\text{TiO}_2$  nanotubes were prepared by anodization, as described previously [47]. Briefly, a machined Ti sheet was electropolished under perchloric acid (Sigma, MO, USA) solution mixed with buoxy ethylene glycol (Junsei Co., Japan) and methanol (Sigma, MO, USA) at  $-40^\circ\text{C}$  for 30 min. The nanotubes were formed on an electropolished Ti sheet (Alfa-Aesar; 0.25 mm thick, 99.5%) by using a mixture of 0.5 wt% hydrofluoric acid (EM Science; 48%) and acetic acid (Fisher; 98%, volumetric ratio = 7 : 1) at 15 V for 30 min. A platinum electrode (Alfa-Aesar; 99.9%) served as the cathode. The specimen was rinsed with deionized water, dried at  $80^\circ\text{C}$ , and heat treated at  $500^\circ\text{C}$  for 2 h to transform the as-anodized amorphous  $\text{TiO}_2$  nanotubes into the crystalline phase. The specimens ( $1.27 \times 1.27 \text{ cm}^2$  area) used for all experiments were sterilized by autoclaving before use. An identically sized flat Ti sample was used as a control after being cleaned with acetone and isopropyl alcohol, dried, and autoclaved.

**2.3. Scanning Electron Microscopy (SEM).** Machined, polished, and fabricated  $\text{TiO}_2$  nanotubes were sputter-coated with very thin gold for examination by scanning electron microscopy (SEM). The morphology of the  $\text{TiO}_2$  nanotubes was observed using SEM (XL30, FEI Corporation).

**2.4. Simultaneous Measurement of  $[\text{Ca}^{2+}]_i$  and  $[\text{ROS}]_i$ .**  $[\text{Ca}^{2+}]_i$  and  $[\text{ROS}]_i$  levels were determined as previously described by using the  $\text{Ca}^{2+}$ -sensitive fluorescent dye Fura-2/AM or the ROS-sensitive fluorescent dye CM-H2DCFDA, respectively [48]. Briefly, isolated BMMs were seeded on the designated plate (Ti sheet or cover glass) at approximately 80% confluence ( $6 \times 10^5$  cells/35-mm dish) and cultured in  $\alpha$ MEM medium supplemented with 10% FBS and M-CSF (30 ng/mL). The following day, cells were loaded with Fura-2/AM and CM-H2DCFDA for 50 min at room temperature. The plate containing cells was placed in a perfusion chamber and then connected to a perfusion system. Cells were briefly washed out with regular HEPES buffer (10 mmol/L HEPES, 140 mmol/L NaCl, 5 mmol/L KCl, 1 mmol/L  $\text{MgCl}_2$ , 1 mmol/L  $\text{CaCl}_2$ , and 10 mmol/L glucose, adjusted to pH 7.4 and 310 mOsm). Each of the indicated compounds was diluted in regular HEPES buffer or  $\text{Ca}^{2+}$  free HEPES buffer (10 mmol/L HEPES, 140 mmol/L NaCl, 5 mmol/L KCl, 1 mmol/L  $\text{MgCl}_2$ , 1 mmol/L EGTA, and 10 mmol/L glucose, adjusted to pH 7.4 and 310 mOsm) and perfused for a designated length of time. Under continuous perfusion with regular HEPES buffer ( $37^\circ\text{C}$ ), titanium plates containing BMMs were sequentially exposed to specific wavelengths of light (340, 380, and 488 nm), and emitted fluorescence (510 nm) was captured using a CCD camera. Captured images were digitized and analyzed using MetaFluor software.  $[\text{Ca}^{2+}]_i$  data were expressed as ratio of fluorescence intensities ( $F_{340}/F_{380}$ ), and intensity of ROS ( $F_{488}$ ) was normalized and expressed as the relative value of initial intensity.

**2.5. Statistical Analysis.** Results were analyzed using Student's two-tailed *t*-test and the data are presented as mean  $\pm$  SEM of the stated number of observations obtained from the indicated number of independent experiments. *P* values less than 0.05 were considered statistically significant \*\* *P* < 0.01.

## 3. Results and Discussion

**3.1. UV Exposure of  $\text{TiO}_2$  Nanotubes Mediates  $[\text{ROS}]_i$  Reduction and  $[\text{Ca}^{2+}]_i$  Increase in BMMs.** We previously reported that modification of the Ti surface, such as by fabrication of nanotubes, dictates cellular fate [49], and aligned  $\text{TiO}_2$  nanotubes significantly accelerate the growth of osteoblasts [47]. This is a critical factor in determining osseointegration. In the process of bone remodeling, the osteoclast is also responsible for enhancing osseointegration by resorbing bone on the border between the implant and bone tissue, which triggers the deposition of bone matrix [50]. This evidence raised a question as to whether or not topographical modification of Ti can affect the cellular response of osteoclasts.

Free  $\text{Ca}^{2+}$  ions act as secondary messengers that mediate diverse cellular responses such as differentiation, motility,

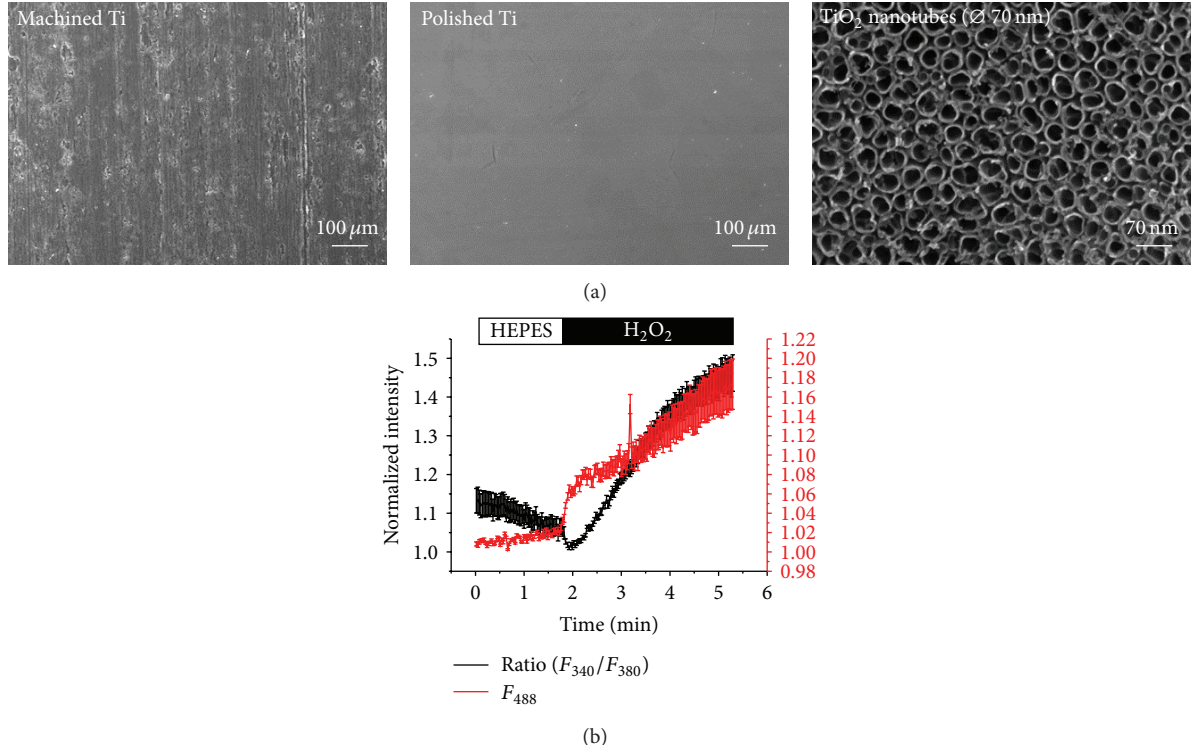


FIGURE 1: SEM micrographs of self-aligned TiO<sub>2</sub> nanotubes and simultaneous measurement of intracellular Ca<sup>2+</sup> and ROS levels. (a) The self-assembly layers were generated by anodizing Ti sheets (scale bar, 70 nm). Machined and polished Ti sheets were presented as negative control (scale bar, 100 μm). (b) As control experiment, isolated BMMs were seeded on the cover glass and maintained for 24 h. H<sub>2</sub>O<sub>2</sub> (1 mM) diluted in regular HEPES buffer was acutely treated and [Ca<sup>2+</sup>]<sub>i</sub> and [ROS]<sub>i</sub> levels in the same cell were simultaneously measured. [Ca<sup>2+</sup>]<sub>i</sub> and [ROS]<sub>i</sub> levels were normalized and presented as a ratio ( $F_{340}/F_{380}$ ; black line) and a relative value ( $F_{488}$ ; red line) compared to initial intensity.

and apoptosis [51]. Importantly, our previous report indicates that stimulation of BMMs (the precursors of osteoclasts) with RANKL induces ROS generation, which is essential for differentiation of BMMs into osteoclasts [48]. Considering that Ti is immediately oxidized upon exposure to air, forming titanium dioxide (TiO<sub>2</sub>, titania), and TiO<sub>2</sub> generates ROS under UV light exposure, characterizing the correlation between intracellular Ca<sup>2+</sup> signaling in BMMs and TiO<sub>2</sub>-originated ROS is crucial for understanding the interaction between osteoclasts and implant materials, especially Ti. This led us to examine how UV photocatalysis of TiO<sub>2</sub> nanotubes affects intracellular Ca<sup>2+</sup> responses in BMMs.

As shown in Figure 1(a), self-aligned TiO<sub>2</sub> nanotubes were synthesized by anodization. The nanotubes were fabricated with an electropolished Ti sheet in order to remove unwanted foreign materials deposited on the Ti sheets and to improve the uniformity of the nanotubes. We subsequently measured [Ca<sup>2+</sup>]<sub>i</sub> and [ROS]<sub>i</sub> in cells seeded on a cover glass as a pilot experiment and confirmed whether [Ca<sup>2+</sup>]<sub>i</sub> and [ROS]<sub>i</sub> levels can be measured in the same cell. Cells were then exposed to 340 nm, 380 nm, and 488 nm wavelength lights, in sequence, to measure [Ca<sup>2+</sup>]<sub>i</sub> and [ROS]<sub>i</sub> levels simultaneously. Each emitted fluorescence signal was collected at 510 nm and presented as described in Section 2. H<sub>2</sub>O<sub>2</sub> treatment of macrophage cells is known to elicit an acute [Ca<sup>2+</sup>]<sub>i</sub> increase [52]. As expected, [Ca<sup>2+</sup>]<sub>i</sub> and [ROS]<sub>i</sub> increased in response to H<sub>2</sub>O<sub>2</sub> (Figure 1(b)).

Next, BMMs seeded on polished Ti and TiO<sub>2</sub> nanotubes were loaded with both fluorescent dyes and [Ca<sup>2+</sup>]<sub>i</sub> and [ROS]<sub>i</sub> levels were measured simultaneously. Interestingly, cells on polished Ti showed no change in [Ca<sup>2+</sup>]<sub>i</sub> levels and a small reduction was observed in [ROS]<sub>i</sub> levels, whereas cells on TiO<sub>2</sub> nanotubes showed an acute and large [Ca<sup>2+</sup>]<sub>i</sub> increase and significant [ROS]<sub>i</sub> reduction in response to UV exposure (Figures 2(a) and 2(b)). To define whether [Ca<sup>2+</sup>]<sub>i</sub> increase in cells on TiO<sub>2</sub> nanotubes results from ROS generation by the Ti surface, UV-mediated [Ca<sup>2+</sup>]<sub>i</sub> increase was measured in the presence of NAC (10 mM). Figures 2(d) and 2(e) clearly show that removal of extracellular and intracellular ROS abolishes [Ca<sup>2+</sup>]<sub>i</sub> increase in cells on TiO<sub>2</sub> nanotubes. This suggests that ROS generated from TiO<sub>2</sub> nanotubes are responsible for UV-mediated [Ca<sup>2+</sup>]<sub>i</sub> increase in cells grown on TiO<sub>2</sub>.

**3.2. Nicardipine Significantly Attenuates UV Photocatalysis-Mediated [Ca<sup>2+</sup>]<sub>i</sub> Increase but Does Not Attenuate [ROS]<sub>i</sub> Reduction.** Considering these results, we next aimed to determine how UV photocatalysis of TiO<sub>2</sub> elicits a [Ca<sup>2+</sup>]<sub>i</sub> increase in BMMs. We first noted that UV photocatalysis of TiO<sub>2</sub> unexpectedly reduces [ROS]<sub>i</sub> even though UV photocatalysis is known to generate ROS on the surface of TiO<sub>2</sub>. We also noted that ROS scavenging by NAC abolished UV photocatalysis-mediated [Ca<sup>2+</sup>]<sub>i</sub>

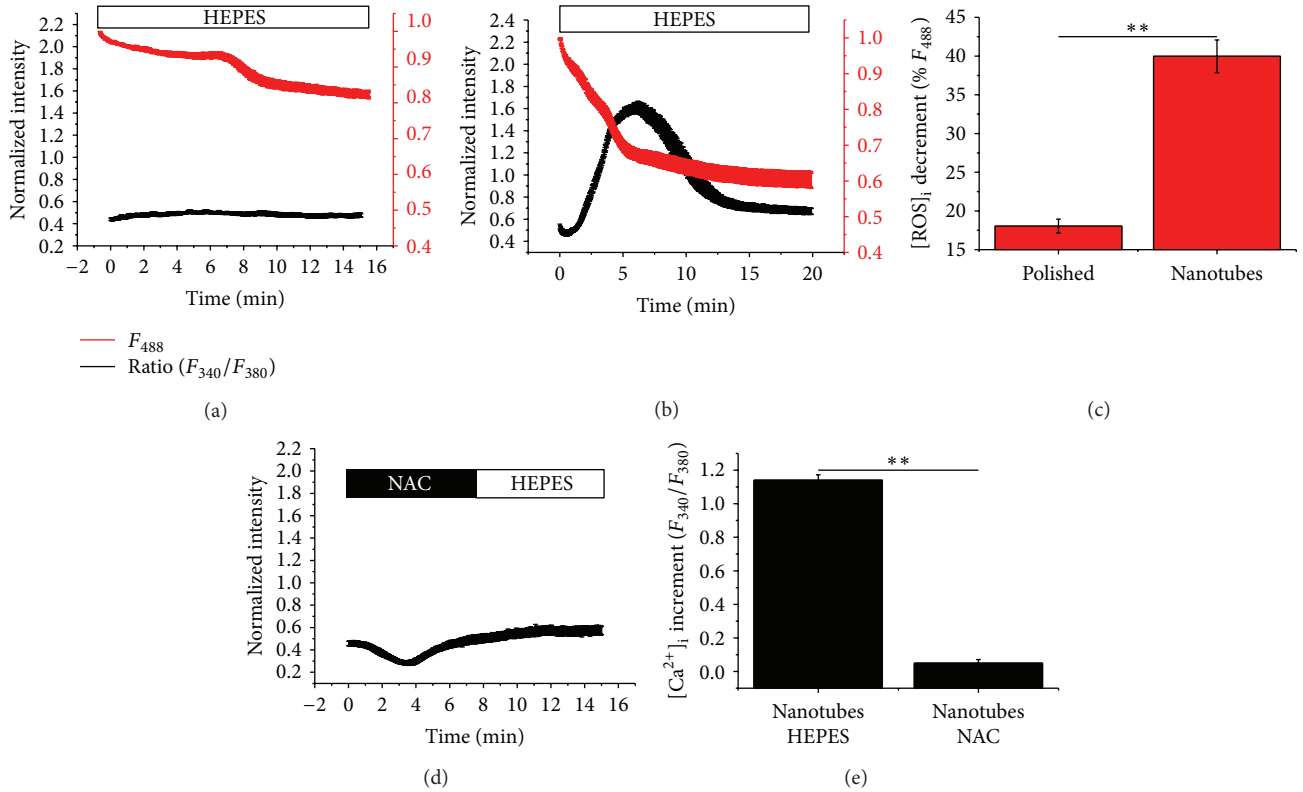


FIGURE 2: UV-mediated photocatalysis of  $\text{TiO}_2$  nanotubes elicits an increase in the concentration of cytosolic  $\text{Ca}^{2+}$  ( $[\text{Ca}^{2+}]_i$ ) and a decrease in the concentration of cytosolic reactive oxygen species ( $[\text{ROS}]_i$ ) in BMMs, both of which are abolished by N-acetyl-L-cysteine (NAC) treatment. (a, b) Under continuous perfusion with HEPES buffer, cells seeded on the (a) polished Ti and (b)  $\text{TiO}_2$  nanotubes were, respectively, exposed to UV light (wavelength = 340 nm and 380 nm). Following UV exposure,  $[\text{ROS}]_i$  (red line) and  $[\text{Ca}^{2+}]_i$  (black line) levels were simultaneously measured and presented as described in “Section 2”. (c) The columns show the percentage of  $[\text{ROS}]_i$  decrement compared to the initial intensity. (d)  $[\text{Ca}^{2+}]_i$  response in cells seeded on  $\text{TiO}_2$  nanotubes was measured in the presence of 10 mM of NAC. NAC diluted in regular HEPES buffer was treated for the indicated time and washed out with regular HEPES buffer. (e) The columns show  $[\text{Ca}^{2+}]_i$  increment ( $F_{340}/F_{380}$ ).

increase. Based on these key observations, we assumed that loss of  $[\text{ROS}]_i$  might change membrane potential and activate voltage-gated  $\text{Ca}^{2+}$  channels (VGCCs). A previous report indicates that it is possible that UV photocatalysis of  $\text{TiO}_2$  turns Ti into a semiconductor, allowing electrons-transfer reactions to occur [53]. To confirm this suspicion, we treated cells with nicardipine, an inhibitor of voltage-gated  $\text{Ca}^{2+}$  channels, and measured UV photocatalysis-mediated  $[\text{Ca}^{2+}]_i$  increase and  $[\text{ROS}]_i$  reduction. In Figures 3(a)–3(c), UV photocatalysis-mediated  $[\text{Ca}^{2+}]_i$  increase was significantly attenuated by inhibition of VGCCs. However, nicardipine did not affect  $[\text{ROS}]_i$ . These results support our hypothesis that UV photocatalysis activates VGCCs and elicits a  $[\text{Ca}^{2+}]_i$  increase and that  $[\text{ROS}]_i$  reduction by UV photocatalysis may be involved in VGCC activation and  $[\text{Ca}^{2+}]_i$  increase. Our previous study demonstrated that the Cacna1A and Cacna1D subunits, which are constituents of VGCCs, are the most highly expressed subunits. Further studies are necessary to determine how these molecules are involved in the effects observed after UV photocatalysis of  $\text{TiO}_2$ .

**3.3. Phospholipase C (PLC) Activity Is Not Involved in UV Photocatalysis-Mediated  $[\text{Ca}^{2+}]_i$  Increase and  $[\text{ROS}]_i$  Reduction.** ROS are highly reactive and can nonspecifically activate molecules in the plasma membrane or inside the cell. Diverse extracellular stimuli including hormones, neurotransmitters, and exogenous ROS function through PLC to mobilize  $\text{Ca}^{2+}$  from internal  $\text{Ca}^{2+}$  stores [54]. To determine whether UV photocatalysis-mediated  $[\text{Ca}^{2+}]_i$  increase is mediated by PLC activation, cells on  $\text{TiO}_2$  nanotubes were treated with U73122 to inhibit PLCs. When the cells on  $\text{TiO}_2$  nanotubes were exposed to UV in the presence of U73122 (10  $\mu\text{M}$ ),  $[\text{Ca}^{2+}]_i$  was not significantly increased compared to that in cells treated with HEPES buffer (Figures 4(a) and 4(b)). Moreover, inhibition of PLCs by U73122 did not affect UV photocatalysis-mediated  $[\text{ROS}]_i$  reduction compared to that observed in a control treated with HEPES buffer (Figure 4(c)). These results demonstrate that UV photocatalysis-mediated  $[\text{Ca}^{2+}]_i$  increase and  $[\text{ROS}]_i$  reduction are not related to PLC activation. Considering previous results that showed that UV photocatalysis of  $\text{TiO}_2$  mediates  $[\text{ROS}]_i$  reduction and had no

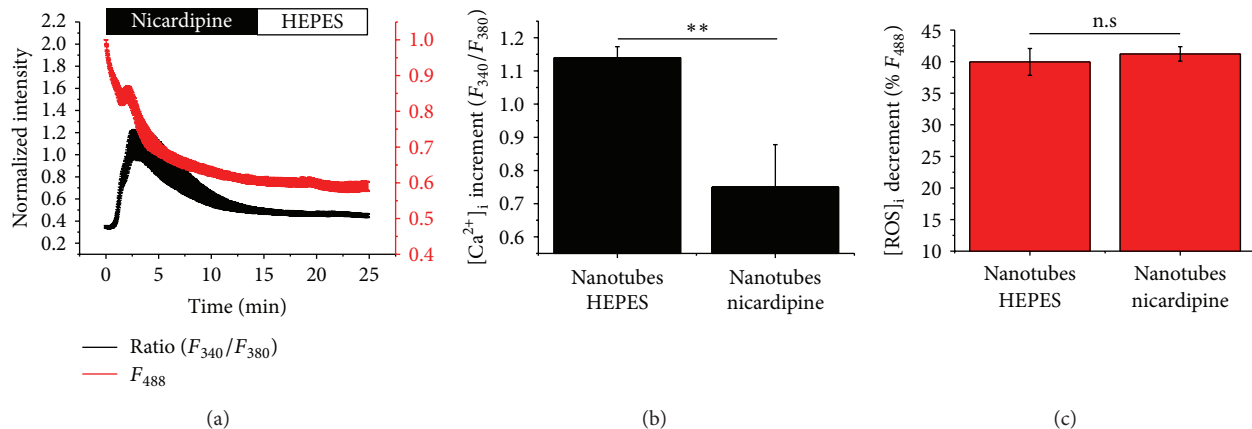


FIGURE 3: Nicardipine, an inhibitor of voltage-gated  $\text{Ca}^{2+}$  channel, attenuates UV photocatalysis-mediated  $[\text{Ca}^{2+}]_i$  increase but not  $[\text{ROS}]_i$  reduction. Isolated BMMs were seeded on polished Ti and  $\text{TiO}_2$  nanotubes and loaded with Fura-2/AM and CM-H2DCFDA. (a) UV photocatalysis-mediated  $[\text{Ca}^{2+}]_i$  increase in cells on  $\text{TiO}_2$  nanotubes was measured in the presence of nicardipine (10  $\mu\text{M}$ ) diluted in HEPES buffer. (b, c) The columns indicate  $[\text{Ca}^{2+}]_i$  increment and  $[\text{ROS}]_i$  decrement in BMMs.

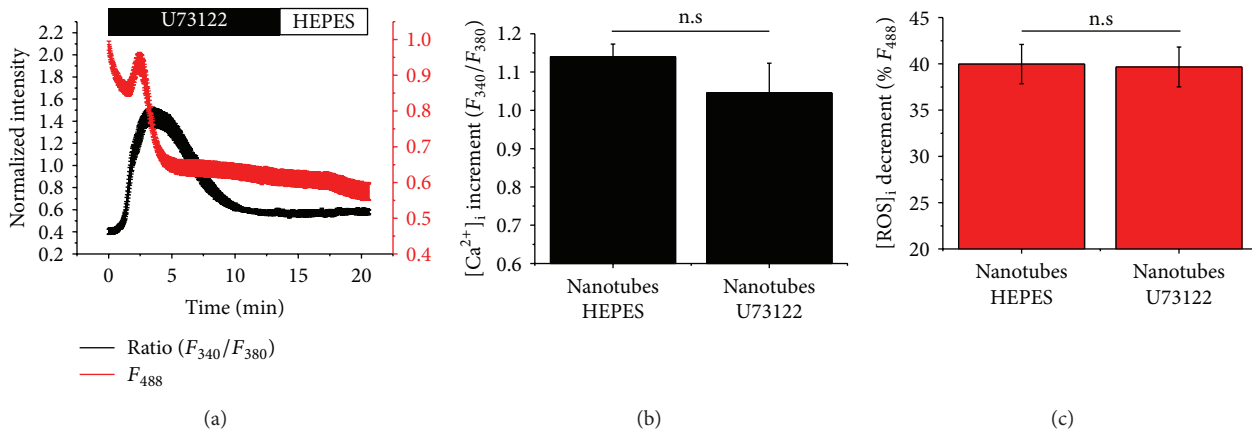


FIGURE 4: U73122, an inhibitor of Phospholipase C, has no effects on UV photocatalysis-mediated  $[\text{Ca}^{2+}]_i$  increase and  $[\text{ROS}]_i$  reduction. Isolated BMMs were seeded on polished Ti and  $\text{TiO}_2$  nanotubes and loaded with Fura-2/AM and CM-H2DCFDA. (a) UV photocatalysis-mediated  $[\text{Ca}^{2+}]_i$  increase in cells on  $\text{TiO}_2$  nanotubes was measured in the presence of U73122 (10  $\mu\text{M}$ ) diluted in HEPES buffer. (b, c) The columns indicate  $[\text{Ca}^{2+}]_i$  increment and  $[\text{ROS}]_i$  decrement in BMMs.

effects on PLC activity, we suggest that ROS generated by UV photocatalysis on  $\text{TiO}_2$  have no permeability.

#### 4. Conclusions

In summary, our study demonstrates that UV photocatalysis of  $\text{TiO}_2$  immediately elicits  $[\text{Ca}^{2+}]_i$  increase and  $[\text{ROS}]_i$  reduction in cells growing on  $\text{TiO}_2$  nanotubes. UV photocatalysis-mediated  $[\text{Ca}^{2+}]_i$  increase is dependent on extracellular and intracellular ROS generation. Furthermore, extracellular  $\text{Ca}^{2+}$  influx thorough VGCCs is critical for UV photocatalysis-mediated  $[\text{Ca}^{2+}]_i$  increase, while PLC activation is not. Considering the physiological roles of  $\text{Ca}^{2+}$  signaling in BMMs and osteoclastogenesis, nanotopography on the Ti surface should be considered an important factor that can influence successful dental implantation.

#### Conflict of Interests

The authors state that they have no conflict of interests.

#### Authors' Contribution

Seunghan Oh and Eun-Joo Choi contributed equally to this work.

#### Acknowledgment

This research was supported by Basic Science Research Program through the National Research Foundation of Korea (NRF) funded by the Ministry of Education, Science, and Technology (NRF-2012R1A1A1038381).

## References

- [1] D. Buser, T. Nydegger, T. Oxland et al., "Interface shear strength of titanium implants with a sandblasted and acid-etched surface: a biomechanical study in the maxilla of miniature pigs," *Journal of Biomedical Materials Research*, vol. 45, no. 2, pp. 75–83, 1999.
- [2] R. Adell, B. Eriksson, U. Lekholm, P. I. Bränemark, and T. Jemt, "Long-term follow-up study of osseointegrated implants in the treatment of totally edentulous jaws," *The International Journal of Oral & Maxillofacial Implants*, vol. 5, no. 4, pp. 347–359, 1990.
- [3] T. Albrektsson, P.-I. Branemark, H.-A. Hansson, and J. Lindstrom, "Osseointegrated titanium implants. Requirements for ensuring a long-lasting, direct bone-to-implant anchorage in man," *Acta Orthopaedica Scandinavica*, vol. 52, no. 2, pp. 155–170, 1981.
- [4] X. Y. Liu, P. K. Chu, and C. X. Ding, "Surface modification of titanium, titanium alloys, and related materials for biomedical applications," *Materials Science & Engineering R: Reports*, vol. 47, no. 3-4, pp. 49–121, 2004.
- [5] B. D. Boyan, T. W. Hummert, D. D. Dean, and Z. Schwartz, "Role of material surfaces in regulating bone and cartilage cell response," *Biomaterials*, vol. 17, no. 2, pp. 137–146, 1996.
- [6] L. Le Guéhenneuc, A. Soueidan, P. Layrolle, and Y. Amouriq, "Surface treatments of titanium dental implants for rapid osseointegration," *Dental Materials*, vol. 23, no. 7, pp. 844–854, 2007.
- [7] D. Chappard, "Bone modeling and remodeling during osseointegration," *Revue de Stomatologie, de Chirurgie Maxillo-faciale et de Chirurgie Orale*, vol. 114, no. 3, pp. 159–165, 2013.
- [8] J. Hilborn and L. M. Bjursten, "A new and evolving paradigm for biocompatibility," *Journal of Tissue Engineering and Regenerative Medicine*, vol. 1, no. 2, pp. 110–119, 2007.
- [9] C. Eriksson, J. Lausmaa, and H. Nygren, "Interactions between human whole blood and modified TiO<sub>2</sub>-surfaces: Influence of surface topography and oxide thickness on leukocyte adhesion and activation," *Biomaterials*, vol. 22, no. 14, pp. 1987–1996, 2001.
- [10] C. Larsson, P. Thomsen, B.-O. Aronsson et al., "Bone response to surface modified titanium implants: studies on the early tissue response to machined and electropolished implants with different oxide thicknesses," *Biomaterials*, vol. 17, no. 6, pp. 605–616, 1996.
- [11] K. Bordji, J.-Y. Jouzeau, D. Mainard, E. Payan, J.-P. Delagoutte, and P. Netter, "Evaluation of the effect of three surface treatments on the biocompatibility of 316L stainless steel using human differentiated cells," *Biomaterials*, vol. 17, no. 5, pp. 491–500, 1996.
- [12] S. Imade, R. Mori, Y. Uchio, and S. Furuya, "Effect of implant surface roughness on bone fixation: the differences between bone and metal pegs," *Journal of Orthopaedic Science*, vol. 14, no. 5, pp. 652–657, 2009.
- [13] A. Tabassum, G. J. Meijer, J. G. C. Wolke, and J. A. Jansen, "Influence of the surgical technique and surface roughness on the primary stability of an implant in artificial bone with a density equivalent to maxillary bone: a laboratory study," *Clinical Oral Implants Research*, vol. 20, no. 4, pp. 327–332, 2009.
- [14] H.-L. Huang, L.-J. Fuh, J.-T. Hsu, M.-G. Tu, Y.-W. Shen, and C.-L. Wu, "Effects of implant surface roughness and stiffness of grafted bone on an immediately loaded maxillary implant: a 3D numerical analysis," *Journal of Oral Rehabilitation*, vol. 35, no. 4, pp. 283–290, 2008.
- [15] J. Duyck, E. Slaets, K. Sasaguri, K. Vandamme, and I. Naert, "Effect of intermittent loading and surface roughness on peri-implant bone formation in a bone chamber model," *Journal of Clinical Periodontology*, vol. 34, no. 11, pp. 998–1006, 2007.
- [16] M. M. Shalabi, J. G. C. Wolke, and J. A. Jansen, "The effects of implant surface roughness and surgical technique on implant fixation in an in vitro model," *Clinical Oral Implants Research*, vol. 17, no. 2, pp. 172–178, 2006.
- [17] M. Marchisio, M. di Carmine, R. Pagone, A. Piattelli, and S. Mischia, "Implant surface roughness influences osteoclast proliferation and differentiation," *Journal of Biomedical Materials Research—Part B: Applied Biomaterials*, vol. 75, no. 2, pp. 251–256, 2005.
- [18] S. H. Chung, H.-K. Kim, W.-J. Shon, and Y.-S. Park, "Peri-implant bone formations around (Ti,Zr)O<sub>2</sub>-coated zirconia implants with different surface roughness," *Journal of Clinical Periodontology*, vol. 40, no. 4, pp. 404–411, 2013.
- [19] M. Bigerelle, K. Anselme, B. Noël, I. Ruderman, P. Hardouin, and A. Iost, "Improvement in the morphology of Ti-based surfaces: A new process to increase in vitro human osteoblast response," *Biomaterials*, vol. 23, no. 7, pp. 1563–1577, 2002.
- [20] C. G. Kang, Y. B. Park, H. Choi et al., "Osseointegration of implants surface treated with various diameters of TiO<sub>2</sub> nanotubes in rabbit," *Journal of Nanomaterials*, vol. 2015, Article ID 634650, 11 pages, 2015.
- [21] G. Mendonça, D. B. S. Mendonça, F. J. L. Aragão, and L. F. Cooper, "Advancing dental implant surface technology—from micron- to nanotopography," *Biomaterials*, vol. 29, no. 28, pp. 3822–3835, 2008.
- [22] S.-H. Oh, R. R. Finñes, C. Daraio, L.-H. Chen, and S. Jin, "Growth of nano-scale hydroxyapatite using chemically treated titanium oxide nanotubes," *Biomaterials*, vol. 26, no. 24, pp. 4938–4943, 2005.
- [23] A. S. G. Curtis, M. Dolby, and N. Gadegaard, "Cell signaling arising from nanotopography: implications for nanomedical devices," *Nanomedicine*, vol. 1, no. 1, pp. 67–72, 2006.
- [24] J. O. Gallagher, K. F. McGhee, C. D. W. Wilkinson, and M. O. Riehle, "Interaction of animal cells with ordered nanotopography," *IEEE Transactions on Nanobioscience*, vol. 1, no. 1, pp. 24–28, 2002.
- [25] J. Park, S. Bauer, K. von der Mark, and P. Schmuki, "Nanosize and vitality: TiO<sub>2</sub> nanotube diameter directs cell fate," *Nano Letters*, vol. 7, no. 6, pp. 1686–1691, 2007.
- [26] M. Niraula, S. Adhikari, D. Y. Lee et al., "Titania nanotube-silver phosphate hybrid heterostructure for improved visible light induced photocatalysis," *Chemical Physics Letters*, vol. 593, pp. 193–197, 2014.
- [27] N. Murakami, Y. Fujisawa, T. Tsubota, and T. Ohno, "Development of a visible-light-responsive titania nanotube photocatalyst by site-selective modification with hetero metal ions," *Applied Catalysis B: Environmental*, vol. 92, no. 1-2, pp. 56–60, 2009.
- [28] S. B. Abd Hamid, T. L. Tan, C. W. Lai, and E. M. Samsudin, "Multiwalled carbon nanotube/TiO<sub>2</sub> nanocomposite as a highly active photocatalyst for photodegradation of Reactive Black 5 dye," *Chinese Journal of Catalysis*, vol. 35, no. 12, pp. 2014–2019, 2014.
- [29] Ratnawati, J. Gunlazuardi, E. L. Dewi, and Slamet, "Effect of NaBF<sub>4</sub> addition on the anodic synthesis of TiO<sub>2</sub> nanotube arrays photocatalyst for production of hydrogen from glycerol-water solution," *International Journal of Hydrogen Energy*, vol. 39, no. 30, pp. 16927–16935, 2014.

- [30] X. Zhang, Y. Chai, L. Lin, K. Zhang, B. Zhao, and D. He, "An efficient photocatalyst: anodized TiO<sub>2</sub> nanotube arrays codoped with Gd-La," *Catalysis Letters*, vol. 144, no. 6, pp. 987–994, 2014.
- [31] R. X. Zhou, S. Z. Kang, X. Q. Li, L. Wang, L. X. Qin, and J. Mu, "An efficient photocatalyst used in a continuous flow system for hydrogen evolution from water: TiO<sub>2</sub> nanotube arrays fabricated on Ti meshes," *RSC Advances*, vol. 5, no. 9, pp. 6954–6961, 2015.
- [32] F. X. Fu, Y. Q. Gong, P. D. Sun, and Q. Xu, "Development of Fe<sub>2</sub>O<sub>3</sub>-modified TiO<sub>2</sub> nanotube array photoelectrode for water purification," *Abstracts of Papers of the American Chemical Society*, vol. 241, 2011.
- [33] M. Guo, K. Xie, X. Liu, Y. Wang, L. Zhou, and H. Huang, "A strategy to reduce the angular dependence of a dye-sensitized solar cell by coupling to a TiO<sub>2</sub> nanotube photonic crystal," *Nanoscale*, vol. 6, no. 21, pp. 13060–13067, 2014.
- [34] A. Lamberti, A. Sacco, S. Bianco et al., "Charge transport improvement employing TiO<sub>2</sub> nanotube arrays as front-side illuminated dye-sensitized solar cell photoanodes," *Physical Chemistry Chemical Physics*, vol. 15, no. 7, pp. 2596–2602, 2013.
- [35] W. Guo, X. Xue, S. Wang, C. Lin, and Z. L. Wang, "An integrated power pack of dye-sensitized solar cell and Li battery based on double-sided TiO<sub>2</sub> nanotube arrays," *Nano Letters*, vol. 12, no. 5, pp. 2520–2523, 2012.
- [36] Z. Lv, J. Yu, H. Wu et al., "Highly efficient and completely flexible fiber-shaped dye-sensitized solar cell based on TiO<sub>2</sub> nanotube array," *Nanoscale*, vol. 4, no. 4, pp. 1248–1253, 2012.
- [37] C. T. Yip, H. Huang, L. Zhou et al., "Direct and seamless coupling of TiO<sub>2</sub> nanotube photonic crystal to dye-sensitized solar cell: a single-step approach," *Advanced Materials*, vol. 23, no. 47, pp. 5624–5628, 2011.
- [38] E. Zalnezhad, A. Hamouda, G. Faraji, and S. Shamshirband, "TiO<sub>2</sub> nanotube coating on stainless steel 304 for biomedical applications," *Ceramics International*, vol. 41, no. 2, pp. 2785–2793, 2015.
- [39] K. F. Huo, B. Gao, J. J. Fu, L. Z. Zhao, and P. K. Chu, "Fabrication, modification, and biomedical applications of anodized TiO<sub>2</sub> nanotube arrays," *RSC Advances*, vol. 4, no. 33, pp. 17300–17324, 2014.
- [40] Y. K. Lai, L. X. Lin, F. Pan et al., "Bioinspired patterning with extreme wettability contrast on TiO<sub>2</sub> nanotube array surface: a versatile platform for biomedical applications," *Small*, vol. 9, no. 17, pp. 2945–2953, 2013.
- [41] A. Roguska, M. Pisarek, M. Andrzejczuk, M. Lewandowska, K. J. Kurzydlowski, and M. Janik-Czachor, "Surface characterization of Ca-P/Ag/TiO<sub>2</sub> nanotube composite layers on Ti intended for biomedical applications," *Journal of Biomedical Materials Research—Part A*, vol. 100, no. 8, pp. 1954–1962, 2012.
- [42] A. Roguska, M. Pisarek, M. Andrzejczuk, M. Dolata, M. Lewandowska, and M. Janik-Czachor, "Characterization of a calcium phosphate-TiO<sub>2</sub> nanotube composite layer for biomedical applications," *Materials Science and Engineering C: Materials for Biological Applications*, vol. 31, no. 5, pp. 906–914, 2011.
- [43] Y. Li, W. Xiong, C. Zhang et al., "Enhanced osseointegration and antibacterial action of zinc-loaded titania-nanotube-coated titanium substrates: in vitro and in vivo studies," *Journal of Biomedical Materials Research Part A*, vol. 102, no. 11, pp. 3939–3950, 2014.
- [44] S. Minagar, Y. Li, C. C. Berndt, and C. Wen, "The influence of titania-zirconia-zirconium titanate nanotube characteristics on osteoblast cell adhesion," *Acta Biomaterialia*, vol. 12, pp. 281–289, 2015.
- [45] K. Gulati, S. Ramakrishnan, M. S. Aw, G. J. Atkins, D. M. Findlay, and D. Losic, "Biocompatible polymer coating of titania nanotube arrays for improved drug elution and osteoblast adhesion," *Acta Biomaterialia*, vol. 8, no. 1, pp. 449–456, 2012.
- [46] B. S. Smith, P. Capellato, S. Kelley, M. Gonzalez-Juarrero, and K. C. Popat, "Reduced in vitro immune response on titania nanotube arrays compared to titanium surface," *Biomaterials Science*, vol. 1, no. 3, pp. 322–332, 2013.
- [47] S. Oh, C. Daraio, L.-H. Chen, T. R. Pisanic, R. R. Fiñones, and S. Jin, "Significantly accelerated osteoblast cell growth on aligned TiO<sub>2</sub> nanotubes," *Journal of Biomedical Materials Research Part A*, vol. 78, no. 1, pp. 97–103, 2006.
- [48] M. S. Kim, Y.-M. Yang, A. Son et al., "RANKL-mediated reactive oxygen species pathway that induces long lasting Ca<sup>2+</sup> oscillations essential for osteoclastogenesis," *The Journal of Biological Chemistry*, vol. 285, no. 10, pp. 6913–6921, 2010.
- [49] S. Oh, K. S. Brammer, Y. S. J. Li et al., "Stem cell fate dictated solely by altered nanotube dimension," *Proceedings of the National Academy of Sciences of the United States of America*, vol. 106, no. 7, pp. 2130–2135, 2009.
- [50] C. Minkin and V. C. Marinho, "Role of the osteoclast at the bone-implant interface," *Advances in Dental Research*, vol. 13, pp. 49–56, 1999.
- [51] M. J. Berridge, P. Lipp, and M. D. Bootman, "The versatility and universality of calcium signalling," *Nature Reviews Molecular Cell Biology*, vol. 1, no. 1, pp. 11–21, 2000.
- [52] J. Zou, J. F. Ainscough, W. Yang et al., "A differential role of macrophage TRPM2 channels in Ca<sup>2+</sup> signaling and cell death in early responses to H<sub>2</sub>O<sub>2</sub>," *The American Journal of Physiology—Cell Physiology*, vol. 305, no. 1, pp. C61–C69, 2013.
- [53] N. Sakai, Y. Ebina, K. Takada, and T. Sasaki, "Electronic band structure of titania semiconductor nanosheets revealed by electrochemical and photoelectrochemical studies," *Journal of the American Chemical Society*, vol. 126, no. 18, pp. 5851–5858, 2004.
- [54] M. J. Berridge, M. D. Bootman, and H. L. Roderick, "Calcium signalling: dynamics, homeostasis and remodelling," *Nature Reviews Molecular Cell Biology*, vol. 4, no. 7, pp. 517–529, 2003.

## Research Article

# Contact with Fluoride-Releasing Restorative Materials Can Arrest Simulated Approximal Caries Lesion

**Camila de Almeida Brandão Guglielmi, Ana Flávia Bissoto Calvo, Tamara Kerber Tedesco, Fausto Medeiros Mendes, and Daniela Prócida Raggio**

*Department of Orthodontics and Pediatric Dentistry, University of São Paulo, Avenue Prof. Lineu Prestes, 2227 São Paulo, SP, Brazil*

Correspondence should be addressed to Daniela Prócida Raggio; danielar@usp.br

Received 15 June 2015; Revised 3 August 2015; Accepted 9 August 2015

Academic Editor: Tae-Yub Kwon

Copyright © 2015 Camila de Almeida Brandão Guglielmi et al. This is an open access article distributed under the Creative Commons Attribution License, which permits unrestricted use, distribution, and reproduction in any medium, provided the original work is properly cited.

Previous studies have suggested that the presence of white-spot lesion is very probable when adjacent surface is affected by cavitated lesions. This study evaluated the potential of different fluoride-releasing restorative materials in arresting enamel white-spot lesions in approximal surface in contact with them, *in vitro* (I) and *in situ* (II). White-spot lesions were formed in 240 primary enamel specimens via pH-cycling. They were put in contact with cylindrical blocks of 6 materials ( $n = 20$ ): composite resin, 2 high-viscous glass ionomer cements (HVGIC), resin-modified GIC, resin-modified nanoionomer, and polyacid-modified resin. In both studies I and II, these settings were designed to simulate the contact point between the restoration and simulated approximal lesion. For study I, they were subjected to a new pH-cycling cariogenic challenge for 7 or 14 days ( $n = 10$ ). For study II, a randomized double-blind *in situ* design was conducted in two phases (7/14 days) to promote cariogenic challenge. At the end of both studies, specimens were collected for mineral analysis by cross-sectional microhardness. Higher mineral loss was observed for lesions in contact with resin ( $p < 0.001$ ). HVGICs were the most efficient in preventing mineral loss, whereas other materials presented an intermediate behavior. It is concluded that fluoride-releasing materials can moderately reduce white-spot lesions progression, and HVGIC can arrest enamel lesion in approximal surface in contact with them.

## 1. Introduction

Particularly in pediatric dentistry, glass ionomer cements (GICs) have raised interest because of properties such as handling and fluoride release/uptake, conferring it an anticariogenic potential, in addition to its biocompatibility and thermal expansion coefficient similar to tooth [1]; however, poor mechanical properties of conventional GICs make them unsuitable for multiple-surfaces restorations [2].

Nowadays some variations have been proposed to overcome this issue. After observing that better performance might be achieved by enhancing the power/liquid ratio and consequently shortening the period of the acid-base setting reaction, high-viscous GICs (HVGICs) were developed and have become the material of choice to perform the Atraumatic Restorative Treatment (ART) [3]. Clinical studies demonstrated that the HVGIC is equally resistant when compared with amalgam for occlusal cavities in permanent

teeth [4, 5] and also for occlusoproximal cavities in primary teeth [6].

Resin-modified glass ionomer cements (RMGICs) and polyacid-modified resin composites (PMR) have also been developed in an attempt to improve the wear resistance, moisture sensitivity, and esthetic characteristic of GIC, maintaining their fluoride-releasing capacity. Recently, a new generation of RMGIC containing nanoparticles was launched with the aim of improving aesthetics properties, as lower surface wear and staining resistance [7]. However, there is a lack of studies concerning mechanical properties and the anticariogenic effects of this material, even though it seems to present lower surface wear when compared to conventional and resin-modified GIC [8].

The benefits of using fluoride-releasing restorative materials to protect the restoration-tooth interface during a cariogenic challenge have been widely studied and positive results are usually reported [9]. These findings, together with

those found in clinical studies [10–12], suggest that fluoride-releasing restorative materials could possibly extend their protective or therapeutic effect to the enamel of the tooth in approximal surface in contact with them. It would be interesting since approximal surface is considered an area of high plaque accumulation and the presence of white-spot lesion is very probable when the adjacent surface is affected by cavitated lesions [13]. Nevertheless, to the best of our knowledge, no previous studies have been conducted with these alternative restorative materials, especially RMGIC containing nanoparticles and encapsulated HVGIC. It seems that this last one presented an enhanced fluoride release due to a predetermined powder/liquid proportion [14], which can result in a greater benefit to arrest the initial caries lesion in approximal surface.

Thus, our purpose was to evaluate the potential of different fluoride-releasing restorative materials in arresting enamel white-spot lesions in approximal surface in contact with them, under *in vitro* and *in situ* cariogenic challenges.

## 2. Materials and Methods

**2.1. Specimen Preparation and Caries Induction.** This study was approved by the ethical board of the University of São Paulo (#186/2009) and teeth were obtained from the Human Tooth Bank of the University. Two hundred and forty blocks ( $5 \times 5 \times 3$  mm) were obtained from the buccal surface of primary canines. Teeth were free of apparent enamel defects, macroscopic cracks, abrasions, and staining, assessed at 2x magnification with a stereomicroscope (Stereo Discovery V20, Zeiss, Göttingen, NI, Germany). They were cut using a double-face diamond disc (KG Sorensen, São Paulo, SP, Brazil) in a slow-speed handpiece under water irrigation. After that, all slabs surfaces were cleaned with rotating brushes/abrasive paste, washed with deionized water, and maintained in relative humidity. To maintain the convexity of the surface, no other treatment was performed.

The specimens were made completely impermeable with two coats of acid-resistant nail varnish, except for an area of  $3 \times 2$  mm on the center of enamel surface. All of them were submitted to the pH-cycling procedure to create artificial incipient caries lesions. The demineralizing solution contained 2.2 mM CaCl<sub>2</sub>, 2.2 mM NaH<sub>2</sub>PO<sub>4</sub>, and 50 mM acetic acid adjusted to pH 4.6. The remineralizing solution contained 1.5 mM CaCl<sub>2</sub>, 0.9 mM NaH<sub>2</sub>PO<sub>4</sub>, and 0.15 M KCl adjusted to pH 7.0. Each specimen was cycled in 2 mL for 8 hours in the demineralizing solution and 16 hours in the remineralizing solution at room temperature and without agitation, during 10 days. A new solution was used every cycle [15, 16].

**2.2. Restorative Material Preparation.** Cylindrical samples (4 mm in diameter  $\times$  3 mm) were prepared using six restorative materials (composite resin, HVGIC, encapsulated HVGIC, RMGIC, nanoparticle RMGIC, and PMR) using a circular matrix according to manufacturers' instructions (Table 1). Photoactivated materials were accommodated into

the matrix in one increment and light-cured using a halogen-based light-curing unit. Self-cured materials were placed in a single bulk with an insertion spatula, except for encapsulated HVGIC and PMR because they are encapsulated materials and are delivered by syringe. After curing, they were removed from matrix by pressure.

All samples were stored in liquid petroleum jelly for a period of 24 hours [17]. After this period, they were cleaned with gauze and put in contact with the convex surface of enamel slab containing white-spot lesion and fixed with orthodontic band. This setting was designed to simulate the contact point between an occlusoproximal restoration and the adjacent tooth (Figure 1).

**2.3. In Vitro Cariogenic Challenge.** Half of the specimens ( $n = 120$ ) were submitted to an *in vitro* cariogenic challenge for 7 ( $n = 60$ ) or 14 ( $n = 60$ ) days, being immersed on demineralizing and remineralizing solutions with the same composition used for caries lesion induction. Each specimen (enamel + material block) was cycled in 3 mL for 8 hours in the demineralizing solution and 16 hours in the remineralizing solution, which had the pH adjusted for 4.5.

**2.4. In Situ Cariogenic Challenge.** The other half of the specimens ( $n = 120$ ) were submitted to an *in situ* cariogenic challenge conducted in two phases of 7 ( $n = 60$ ) or 14 ( $n = 60$ ) days, with a period of 7-day washout between them. For this purpose, specimens (enamel block + material block) were inserted in acrylic custom-made palatal devices containing 6 cavities ( $6 \times 5 \times 5$  mm), 3 on the left and 3 on the right side. To better fit the chambers, specimens' dimensions were reduced to  $4 \times 4 \times 2$  mm. The chambers were open both to the palatal and to the buccal surfaces and into each of them one slab was fixed with wax. A plastic mesh was fixed with acrylic resin over the chambers, leaving a 1 mm space from the specimen to allow biofilm accumulation and protect it from mechanical disturbance.

To avoid any possible benefit caused by its positions, distribution of specimen was randomly determined according to a computer-generated randomization list for the first appliance mounted. For the following appliances, the position of samples was evenly rotated so that each material occupied the 6 positions.

Ten volunteers from São Paulo (water fluoride level  $0.7 \text{ mg L}^{-1}$ ) were invited to take part in the study based on the following inclusion and exclusion criteria: age between 20 and 40 years; having at least 20 teeth; absence of active caries lesions; no use of fixed or removable orthodontic device; no use of any antibiotics within the 2 months prior to study beginning. They also had to agree with the study terms and be willing to abstain from oral hygiene products except those provided. The study was designed in two phases of 7 ( $n = 60$ ) and 14 ( $n = 60$ ) days, with a period of 7-day washout between them. Thus, half of the volunteers initiated by the 7-days period and the other half initiated by the 14-days period.

Volunteers were instructed to wear their appliance 24 hours per day and during all the experimental period they brushed their teeth with a fluoridated dentifrice (Colgate

TABLE 1: Description of materials tests in the study.

Restorative material	Name	Composition	Insertion and polymerization method
Nanocomposite composite resin	Z350 (3M ESPE, St. Paul, MN, USA)	Silane treated ceramic Silane treated silica Diurethane dimethacrylate (udma) Bisphenol a polyethylene glycol diether dimethacrylate Bisphenol a diglycidyl ether dimethacrylate (bisgma) Silane treated zirconia Polyethylene glycol dimethacrylate Triethylene glycol dimethacrylate (tegdma) 2,6-Di-tert-butyl-p-cresol	2 increments (2 mm)/40 s photoactivation
High-viscous CIV	Ketac Molar (3M ESPE, St. Paul, MN, USA)	Powder: Glass powder Polyacrylic acid Liquid: Water Copolymer of acrylic acid-maleic acid Tartaric acid	Insertion spatula; finger press technique with solid petroleum jelly
Encapsulated high-viscous GIC	Riva Self Cure (SDI, Bayswater, VIC, Australia)	Powder: polyacrylic acid, aluminosilicate glass Liquid: polyacrylic acid, tartaric acid	Delivery syringe; finger press technique with solid petroleum jelly
Resin-modified GIC	Vitremer (3M ESPE, St. Paul, MN, USA)	Powder: Silane treated glass Potassium persulfate Liquid: Copolymer of acrylic and itaconic acids Water 2-Hydroxyethyl methacrylate (hema) Diphenyliodonium hexafluorophosphate	Insertion spatula; finger press technique with solid petroleum jelly
Resin-modified GIC with nanoparticles	Ketac Nano (3M ESPE, St. Paul, MN, USA)	Silane treated glass Silane treated zirconia Polyethylene glycol dimethacrylate (pegdma) Silane treated silica 2-Hydroxyethyl methacrylate (hema) Glass powder Bisphenol a diglycidyl ether dimethacrylate (bisgma) Triethylene glycol dimethacrylate (tegdma)	2 increments (2 mm)/20 s photoactivation
Polyacid-modified resin	Dyract Extra (Dentsply, Konstanz BW, Germany)	Ethoxylated bisphenol-A-dimethacrylate, urethane resin, triethylene glycol dimethacrylate (TEGDMA), and trimethylolpropane trimethacrylate (TMPTMA) and strontium fluoride glass	2 increments (2 mm)/20 s photoactivation

Total 12—1450 mg F/g, Colgate-Palmolive, São Paulo, SP, Brazil). The cariogenic challenge was provided by dripping one drop of 20% sucrose solution over the mesh onto each specimen, 8 times per day at predetermined times. Before reinsertion in the mouth, the appliance was kept on their plastic recipient for 5 min to allow sucrose solution diffusion. The use of dentifrice was performed at least 3 times a day, after meal-times, and when volunteers were habituated to perform oral hygiene. The appliances were extraorally brushed only on the palatal contact surface. When not in the oral cavity (meals and oral hygiene), the appliances were kept moist in their plastic recipients.

After the intraoral experimental phase, the appliances were collected and specimens were removed. The enamel

blocks were separated from the cylindrical material blocks and then brushed gently with a very soft toothbrush to remove biofilm.

**2.5. Cross-Section Microhardness Analysis (CSMH).** Enamel blocks were longitudinally sectioned with double-face diamond discs (KG Sorensen, Cotia, SP, Brazil) through the center of window left for caries induction. One half of each sample was embedded in acrylic resin. The surfaces of the samples were planned with an automatic grinding/polishing machine and SiC discs of #400, #600, #1200, and #1400 grit under running water for 60 s and then polished with diamond paste (1 and 0.25  $\mu\text{m}$ ). Cross-section microhardness measurements of the adjacent enamel were taken using a Knoop

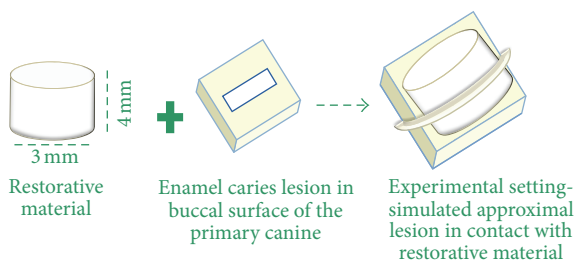


FIGURE 1: Experimental setting of the simulated approximal caries lesion in contact with restorative material.

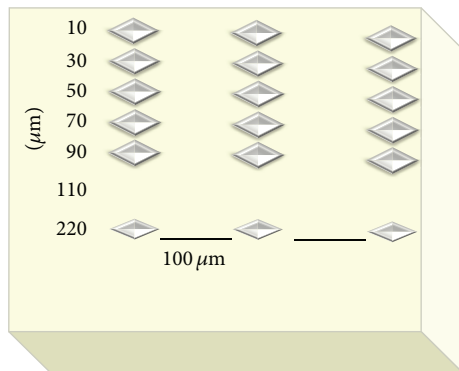


FIGURE 2: Diagram of microhardness measurements performed on each tooth specimen.

indenter attached to a microhardness tester (Shimadzu Micro Hardness Tester HMV-2; Shimadzu Corporation, Kyoto, KYO, Japan). Three rows of 7 indentations each were made, one in the central region of the dental enamel exposed and the other two at a 100  $\mu\text{m}$  distance to both sides of the central row using a 25-gram load for 15 seconds. The indentations were made at 10, 30, 50, 70, 90, 110, and 220  $\mu\text{m}$  from the outer enamel surface (Figure 2). The mean values of the 3 rows measuring points at each distance from the surface were averaged. To obtain values from sound enamel (baseline), 5 indentations were also performed over the area surrounding the window left for caries development and the average was used to represent this value.

**2.6. Statistical Analyses.** Values from CSMH at the different distances were used to construct a graphic (CSMH value versus distance from enamel surface) and the value corresponding to the area below the curve was considered. With regard to reference values from sound enamel (baseline), the average among the 5 indentations performed was used to construct the graph, using the same distances as those performed for the experimental part. Subtracting the experimental value from the baseline value, the surface microhardness value change was obtained and used to perform statically analysis.

Normal distribution of data and equality of variances were confirmed using Anderson–Darling and Levene tests, respectively. Subsequently, ANOVA and Tukey's test were carried out for statistical comparisons amongst restorative

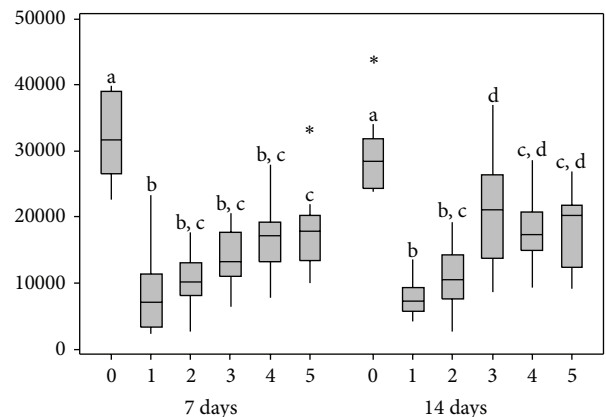


FIGURE 3: Cross-sectional microhardness results for *in vitro* study. Different letters show statistically significant differences ( $p \leq 0.05$ ). 0 = composite resin; 1 = HVGIC; 2 = encapsulated HVGIC; 3 = RMGIC; 4 = nanoparticle RMGIC; 5 = PMR.

materials after *in vitro* challenge ( $\alpha = 5\%$ ). For *in situ* study, multilevel analysis (volunteer and specimen) was performed also at a significance level of 5%. All analyses were conducted using MLwin 2.10 Software (Centro for Multilevel Modeling, University of Bristol, Bristol, UK).

### 3. Results

**3.1. In Vitro Study.** Considering both periods of cariogenic challenge, specimens in contact with composite resin presented the highest mineral loss when comparing to all other materials. For the 7-day period, the HVGIC demonstrated greater capacity for inhibiting artificial caries lesions adjacent to restorations when compared to PMR. For the 14-day period, the inhibitory capacity of the artificial caries lesion from HVGIC was also superior when compared to nanoparticle RMGIC and RMGIC. Results from the *in vitro* study are demonstrated in Figure 3.

**3.2. In Situ Study.** Within the 7-day period of cariogenic challenge, the HVGICs presented the best performance and the composite resin the worst performance in protecting the adjacent caries lesions, whereas the other materials presented an intermediate behavior. For the 14-day period of cariogenic challenge, materials presented a similar behavior, except that nanoparticle RMGIC was as inefficient as composite resin.

Furthermore, the behavior of composite resin was similar in both methods of cariogenic challenge. There was no statistically significant difference between the two HVGICs (HVGIC and encapsulated HVGIC). Results from the *in situ* study are shown in Figure 4.

### 4. Discussion

This study was designed to investigate the effects of different fluoride-releasing restorative materials in arresting initial enamel caries lesion in approximal surface in contact with them, under *in vitro* and *in situ* conditions. Thus, only

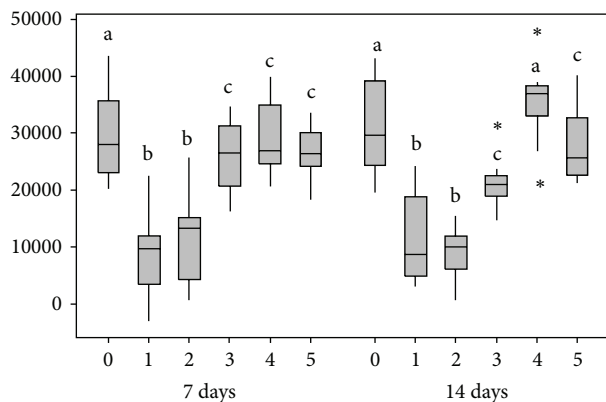


FIGURE 4: Cross-sectional microhardness results for *in situ* study. Different letters show statistically significant differences ( $p \leq 0.05$ ). 0 = composite resin; 1 = HVGIC; 2 = encapsulated HVGIC; 3 = RMGIC; 4 = nanoparticle RMGIC; 5 = PMR.

materials indicated to perform occlusoproximal restorations were used in the study.

In general, the results of the study show that all fluoride-releasing materials are capable of arresting, in a greater or lesser extent, the progression of approximal initial caries lesion in contact with them. HVGICs presented the best performance, whereas other materials presented an intermediate performance between the pure GICs and the composite resin.

According to Wiegand et al. [18], fluoride release characteristics depend on the matrices, fillers, and fluoride content as well as the setting mechanisms and environmental conditions of the restoratives. However, it is commonly assumed that materials presenting higher fluoride release levels are those with poor mechanical properties [19]. In our study, the best anticariogenic potential verified for HVGIC can be explained by its chemical nature. An initial high release from GIC over the first 24 h occurs due to the burst of fluoride resulting from the glass particles when reacting with the polyalkenoate acid during the setting reaction [20]. After that, fluoride is released by both a short-term reaction involving a rapid dissolution from the outer surface into solution and a gradual reaction resulting by the sustained diffusion of ions through the bulk cement.

This finding corroborates a previous study that HVGIC resulted in a superior capacity to protect incipient lesions in approximal surface in contact with them when compared to other materials [21], being that the reservoir property can turn this even more effective. The permeability of the materials is a major factor in the mechanism of fluoride uptake, once they could absorb the ions deep into its bulk. The more permeable the material, the more likely its ability to absorb and release fluoride and composites are known to have relatively low water permeability, whereas the HVGIC and RMGIC have been shown to have greater sorption values [22]. It is also suggested that, in general, materials with higher initial fluoride release have higher recharge capability, even though original values are hardly reached again [23].

Two HVGICs were included in the study, since one of them is presented in the conventional powder/liquid form and the other is disposed in capsules. It has been suggested

that encapsulated GICs can present an enhanced fluoride release once it has a predetermined powder/liquid proportion which facilitates handling and avoids operator and environmental induced variability [14], optimizing its performance. In our study, however, no difference was observed between the performances of these two types of HVGIC.

On the other hand, RMGIC usually demonstrates a comparable potential for releasing fluoride as conventional cements, but they may be affected not only by the formation of complex fluoride compounds and their interaction with polyacrylic acid, but also by the type and amount of resin used for the photochemical reaction [24]. Probably, it can be an explanation for the similar results verified for both RMGIC and RMGIC with nanoparticles in the present study, except for the 14-day period of *in situ* cariogenic challenge.

In fact, nanoparticle RMGIC seems to be less hydrophilic than conventional RMGIC [19]. Contrary to RMGIC, the first phase of setting for PMR is the light-activated polymerization, which means that it behaves initially as composites resins. In this way, after curing and before the contact with water, the fluoride is not free but bound in the filler particles, which are enclosed in the polymerized matrix. After the succeeding water sorption, the acid-base reaction takes place but the continuing fluoride release over time seems to be capable of protecting enamel in contact with these materials under cariogenic challenge [25].

This new generation of RMGIC, the so-called nanoionomers, presents as paste/paste system and is based on bonded nanofiller technology, aiming to promote an improved wear resistance. In fact, some studies have demonstrated lower roughness indices when compared to conventional GIC and RMGIC [8]; however, poor results have been achieved with regard to marginal adaptation and staining when compared to other materials such as conventional RMGIC and composite resin in a clinical trial [26]. Nevertheless, considering its anticariogenic effect, previous study observed better capacity to protect enamel around restorations under a cariogenic challenge than composite resin [27], as observed in this study.

The duration of cariogenic challenge, in general, exerted little influence over the performance of each material, mainly for pure GICs. Probably, the fluoride release for these materials drops moderately 7 days after manipulation. Only for nanoparticle RMGIC the results were similar to those for composite resin after 14 days of *in situ* cariogenic challenge, which is probably associated with its poor capacity to act as a fluoride reservoir [19].

Some studies had already investigated the potential of fluoride-releasing restorative materials to protect the adjacent enamel in approximal contact with them; however this effect is usually tested on sound surfaces [27–29]. We preferred to test the therapeutic effect of fluoride on incipient caries lesion once this condition is most likely to occur clinically, especially if a cavitated lesion is present on the adjacent tooth [13]. Also, unlikely to our study, most of them are not performed with primary teeth, the major indication for fluoride-releasing restorative material. In this way, the design of our study as well as the experimental setting seems to be effective and innovative to test our hypothesis. The enamel specimens were obtained from the buccal surface of deciduous canines

and its curved shape was purposely preserved to simulate adequately the contact point against the cylindrical material block. Conversely the method chosen to develop the enamel caries lesions in both studies (*in vitro* and *in situ*), pH-cycling, was previously demonstrated to be suitable when investigating the role of fluoride in the de-/remineralization process [30, 31].

Even though most studies have tested the fluoride release potential of the restorative materials in deionized water or artificial saliva, the aim of this study was to test it in similar conditions to those found during the cariogenic challenge in mouth. It is known that acidic conditions can potentiate both the fluoride release from restoratives and the hydroxyapatite incorporation by enamel [19, 32], which may have favored their performance. However, the pH drop is also the circumstance in which there is the greatest need of the protection promoted by fluoride. Studies also usually demonstrate that fluoride leached from different fluoridated restorative materials may last for a long period especially for pure GIC; however, after a higher initial release, it drops to lower levels. As the aim of this study was to investigate the therapeutic potential of those materials, the short-term results (7 or 14 days) are more important than long-term results. Moreover, the use of *in situ* design assesses some characteristics that can influence the benefit to use fluoride-releasing restorative materials. The absence of other sources of fluoride from *in vitro* studies, as fluoridate toothpaste, can overestimate the effect of fluoride-releasing restorative materials in arresting initial caries lesion, being the other sources of fluoride sometimes enough to prevent or to arrest caries lesions. Moreover, the presence of biofilm and saliva can also interfere in the effect of these restorative materials.

Many factors must be taken into consideration when selecting a restorative material for primary dentition, including the ease of handling, their physical, chemical, and biological properties, and the possible longevity of the restorations. Although RMGIC, PMR, and composites are generally found to have a superior longevity when comparing to conventional GIC, HVGICs have demonstrated similar longevity to amalgam when performing occlusal restorations permanently [4]. According to Qvist et al. [2], restorations involving the approximal surface are those with the lowest survival rates in deciduous teeth. It should be emphasized, however, that there is no evidence for indicating some restorative material instead of others when considering occlusoproximal restorations on primary teeth [6].

## 5. Conclusions

Fluoride-releasing materials can moderately reduce white-spot lesions progression in surface in contact with them when compared to composite resin. However, HVGIC represents the best choice to arrest initial enamel lesion in approximal adjacent surfaces.

## Conflict of Interests

The authors declare that there is no conflict of interests regarding the publication of this paper.

## Acknowledgments

The authors would like to thank FAPESP (no. 2010/16120-7) and CAPES for financial support. Daniela Prócida Raggio and Fausto Medeiros Mendes receive Research Productivity Scholarship, CNPq.

## References

- [1] G. J. Mount, "Glass ionomers: a review of their current status," *Operative Dentistry*, vol. 24, no. 2, pp. 115–124, 1999.
- [2] V. Qvist, A. Poulsen, P. T. Teglars, and I. A. Mjör, "The longevity of different restorations in primary teeth," *International Journal of Paediatric Dentistry*, vol. 20, no. 1, pp. 1–7, 2010.
- [3] M. A. van 't Hof, J. E. Frencken, W. H. van Palenstein Helderman, and C. J. Holmgren, "The atraumatic restorative treatment (ART) approach for managing dental caries: a meta-analysis," *International Dental Journal*, vol. 56, no. 6, pp. 345–351, 2006.
- [4] J. E. Frencken, M. A. Van 't Hof, W. E. Van Amerongen, and C. J. Holmgren, "Effectiveness of single-surface ART restorations in the permanent dentition: a meta-analysis," *Journal of Dental Research*, vol. 83, no. 2, pp. 120–123, 2004.
- [5] S. Micknautsch and V. Yengopal, "Failure rate of high-viscosity GIC based ART compared with that of conventional amalgam restorations—evidence from an update of a systematic review," *SADJ*, vol. 67, no. 7, pp. 329–331, 2012.
- [6] D. P. Raggio, D. Hesse, T. L. Lenzi, C. Guglielmi, and M. M. Braga, "Is Atraumatic restorative treatment an option for restoring occlusoproximal caries lesions in primary teeth? A systematic review and meta-analysis," *International Journal of Paediatric Dentistry*, vol. 23, no. 6, pp. 435–443, 2013.
- [7] S. B. Mitra, J. D. Oxman, A. Falsafi, and T. T. Ton, "Fluoride release and recharge behavior of a nano-filled resin-modified glass ionomer compared with that of other fluoride releasing materials," *American Journal of Dentistry*, vol. 24, no. 6, pp. 372–378, 2011.
- [8] S. B. P. de Fúcio, A. B. de Paula, F. G. de Carvalho, V. P. Feitosa, G. M. B. Ambrosano, and R. M. Puppin-Rontani, "Biomechanical degradation of the nano-filled resin-modified glass-ionomer surface," *The American Journal of Dentistry*, vol. 25, no. 6, pp. 315–320, 2012.
- [9] S. Micknautsch, V. Yengopal, and A. Banerjee, "Atraumatic restorative treatment versus amalgam restoration longevity: a systematic review," *Clinical Oral Investigations*, vol. 14, no. 3, pp. 233–240, 2010.
- [10] V. Qvist, L. Laurberg, A. Poulsen, and P. T. Teglars, "Eight-year study on conventional glass ionomer and amalgam restorations in primary teeth," *Acta Odontologica Scandinavica*, vol. 62, no. 1, pp. 37–45, 2004.
- [11] V. Qvist, L. Laurberg, A. Poulsen, and P. T. Teglars, "Class II restorations in primary teeth: 7-Year study on three resin-modified glass ionomer cements and a compomer," *European Journal of Oral Sciences*, vol. 112, no. 2, pp. 188–196, 2004.
- [12] V. Qvist, E. Manscher, and P. T. Teglars, "Resin-modified and conventional glass ionomer restorations in primary teeth: 8-year results," *Journal of Dentistry*, vol. 32, no. 4, pp. 285–294, 2004.
- [13] M. G. Cagetti, G. Campus, S. Sale, F. Cocco, L. Strohmenger, and P. Lingström, "Association between interdental plaque acidogenicity and caries risk at surface level: a cross sectional study in primary dentition," *International Journal of Paediatric Dentistry*, vol. 21, no. 2, pp. 119–125, 2011.

- [14] R. P. Sousa, I. C. J. Zanin, J. P. M. Lima et al., “In situ effects of restorative materials on dental biofilm and enamel demineralisation,” *Journal of Dentistry*, vol. 37, no. 1, pp. 44–51, 2009.
- [15] F. M. Mendes and J. Nicolau, “Utilization of laser fluorescence to monitor caries lesions development in primary teeth,” *Journal of Dentistry for Children*, vol. 71, no. 2, pp. 139–142, 2004.
- [16] J. M. ten Cate and P. P. E. Duijsters, “Alternating demineralization and remineralization of artificial enamel lesions,” *Caries Research*, vol. 16, no. 3, pp. 201–210, 1982.
- [17] D. P. Raggio, C. C. Bonifácio, M. Bönecker, J. C. P. Imparato, A. J. de Gee, and W. E. van Amerongen, “Effect of insertion method on knoop hardness of high viscous glass ionomer cements,” *Brazilian Dental Journal*, vol. 21, no. 5, pp. 439–445, 2010.
- [18] A. Wiegand, W. Buchalla, and T. Attin, “Review on fluoride-releasing restorative materials—fluoride release and uptake characteristics, antibacterial activity and influence on caries formation,” *Dental Materials*, vol. 23, no. 3, pp. 343–362, 2007.
- [19] J. L. Moreau and H. H. K. Xu, “Fluoride releasing restorative materials: effects of pH on mechanical properties and ion release,” *Dental Materials*, vol. 26, no. 11, pp. e227–e235, 2010.
- [20] J. W. Nicholson, “Chemistry of glass-ionomer cements: a review,” *Biomaterials*, vol. 19, no. 6, pp. 485–494, 1998.
- [21] C. B. Marinelli, K. J. Donly, J. S. Wefel, J. R. Jakobsen, and G. E. Denehy, “An in vitro comparison of three fluoride regimens on enamel remineralization,” *Caries Research*, vol. 31, no. 6, pp. 418–422, 1997.
- [22] N. Attar and A. Önen, “Fluoride release and uptake characteristics of aesthetic restorative materials,” *Journal of Oral Rehabilitation*, vol. 29, no. 8, pp. 791–798, 2002.
- [23] N. Attar and M. D. Turgut, “Fluoride release and uptake capacities of fluoride-releasing restorative materials,” *Operative Dentistry*, vol. 28, no. 4, pp. 395–402, 2003.
- [24] G. J. Mount, C. Patel, and O. F. Makinson, “Resin modified glass-ionomers: strength, cure depth and translucency,” *Australian Dental Journal*, vol. 47, no. 4, pp. 339–343, 2002.
- [25] Á. M. Lennon, A. Wiegand, W. Buchalla, and T. Attin, “Approximal caries development in surfaces in contact with fluoride-releasing and non-fluoride-releasing restorative materials: an in situ study,” *European Journal of Oral Sciences*, vol. 115, no. 6, pp. 497–501, 2007.
- [26] J. Perdigão, M. Dutra-Corrêa, S. H. C. Saraceni, M. T. Ciaramicoli, and V. H. Kiyan, “Randomized clinical trial of two resin-modified glass ionomer materials: 1-year results,” *Operative Dentistry*, vol. 37, no. 6, pp. 591–601, 2012.
- [27] C. F. C. Salas, C. A. B. Guglielmi, D. P. Raggio, and F. M. Mendes, “Mineral loss on adjacent enamel glass ionomer cements restorations after cariogenic and erosive challenges,” *Archives of Oral Biology*, vol. 56, no. 10, pp. 1014–1019, 2011.
- [28] K.-T. Jang, F. Garcia-Godoy, K. J. Donly, and A. Segura, “Remineralizing effects of glass ionomer restorations on adjacent interproximal caries,” *Journal of Dentistry for Children*, vol. 68, no. 2, pp. 125–128, 2001.
- [29] L. Papagiannoulis, A. Kakaboura, and G. Eliades, “In vivo vs in vitro anticariogenic behavior of glass-ionomer and resin composite restorative materials,” *Dental Materials*, vol. 18, no. 8, pp. 561–569, 2002.
- [30] A. C. Magalhães, B. M. Moron, L. P. Comar, A. Wiegand, W. Buchalla, and M. A. R. Buzalaf, “Comparison of cross-sectional hardness and transverse microradiography of artificial carious enamel lesions induced by different demineralising solutions and gels,” *Caries Research*, vol. 43, no. 6, pp. 474–483, 2009.
- [31] A. E. De Mello Vieira, A. C. Botazzo Delbem, K. T. Sasaki, E. Rodrigues, J. A. Cury, and R. F. Cunha, “Fluoride dose response in pH-cycling models using bovine enamel,” *Caries Research*, vol. 39, no. 6, pp. 514–520, 2005.
- [32] J. A. Cury and L. M. A. Tenuta, “Enamel remineralization: controlling the caries disease or treating early caries lesions?” *Brazilian Oral Research*, vol. 23, no. 1, pp. 23–30, 2009.

## Research Article

# A Novel Approach of Targeted Immunotherapy against Adenocarcinoma Cells with Nanoparticles Modified by CD16 and MUC1 Aptamers

Lianyuan Yu, Yan Hu, Jinhong Duan, and Xian-Da Yang

Institute of Basic Medical Sciences, Chinese Academy of Medical Sciences, School of Basic Medicine of Peking Union Medical College, Beijing 100005, China

Correspondence should be addressed to Xian-Da Yang; [ayangmd@gmail.com](mailto:ayangmd@gmail.com)

Received 14 April 2015; Accepted 4 June 2015

Academic Editor: Tae-Yub Kwon

Copyright © 2015 Lianyuan Yu et al. This is an open access article distributed under the Creative Commons Attribution License, which permits unrestricted use, distribution, and reproduction in any medium, provided the original work is properly cited.

Mucin 1 (MUC1) is a potentially important target of cancer therapy, being a glycoprotein that is overexpressed on cell surface of many types of adenocarcinomas, including breast, ovarian, colon, lung, and prostatic cancers. Several MUC1-targeted drug delivery systems have been developed and reported, but mobilizing natural killer cells (NK) to fight against MUC1-positive tumor has not been attempted. In this study, we introduced a novel amphipathic nanoparticle (NP) for enhancing the NK cytotoxicity to MUC1-positive cancer cells. The amphipathic NP had CD16 and MUC1 aptamers on its surface and was designed to bind with both the CD16-positive NK cells and the MUC1-positive tumor cells and pull the two types of cells close to each other. The fabricated amphipathic NP had an average size of 574 nm. The aptamers' conjugation with the NP was confirmed by DNA hybridization experiments. Dark-field microscopy revealed that the amphipathic NP could recruit more NK cells to the vicinity of MUC1-positive cancer cells. Additionally, the amphipathic NP significantly enhanced the NK cytotoxicity to MUC1-positive cancer cells ( $p < 0.01$ ), but not that to the MUC1-negative control cells. The results suggest that NK cells may potentially be mobilized to selectively fight against MUC1-positive cancer cells.

## 1. Introduction

Traditional cancer therapies include surgery, chemotherapy, and radiotherapy, but these therapies have their own limitation or drawbacks as in clinical application. Surgery is quite effective for early treatment of solid tumors, but it is useless for advanced tumor, nonsolid tumor, and leukemia. As in chemotherapy, long-term use of chemotherapy drugs will develop the drug resistance of tumor cells and reduce the efficacy of these drugs. Beyond that, as well as eliminating cancer cells, the chemotherapy drugs also attack the normal tissue and immune system of cancer patients, which will result in drug toxicity [1]. Additionally, general and local radiotherapy may cause seriously adverse effect, such as osteoradionecrosis, radiation pneumonitis, and systemic reactions [2]. Besides the above cancer therapies, immunotherapy is a type of tumor therapy built on the principle of stimulating the

patient's immune system to attack and eliminate tumor cells [3]. The currently existing immunotherapies mainly include cell-based therapies, antibody therapies, and cytokine therapies [4, 5]. Compared with chemotherapy and radiotherapy, immunotherapy has several advantages, including low toxicity and long-acting *in vivo* response against tumor cells [6, 7]. Because most grown tumors have immune escape mechanisms, the major challenge facing most immunotherapies is to induce an effective immune response that is strong and durable enough to fight against the cancer cells [8]. As a result, it is necessary to explore new approaches for promoting targeted immune response against cancer cells.

In this study, we developed a novel nanoparticle modified by CD16 and MUC1 aptamers [9, 10], in order to gather NK lymphocytes and adenocarcinoma cells together and enhance the NK reaction against these cancer cells. CD16, namely, Fc<sub>y</sub> receptor III, is mainly expressed on the surface of NK cells,

monocytes, macrophages, and polymorphonuclear cells. MUC1 mucin, a glycoprotein, is underexpressed on normal tissue but gets overexpressed on the cell surface of most adenomas, including colon, breast, ovarian, lung, and pancreatic cancers. Therefore, MUC1 protein is considered an ideal molecular target for immunotherapy [11]. Because the amphipathic NP has CD16 and MUC1 aptamers on its surface, theoretically it can bind with both NK and adenocarcinoma cells, pulling the two types of cells together. In this study, the targeting ligands employed are aptamers. As targeting ligands, aptamer has several advantages compared with antibody, including low immunogenicity, low preparation cost, and easy modification for various applications. Previously studies have reported aptamer as targeting agent to enhance drug delivery to MUC1-positive tumors [10] or probes for lymphoma cells [12]. Therefore, we chose aptamers as the targeting ligands to modify NP in this study. We now report that the aptamers modified amphipathic NP can pull together NK and MUC1-positive tumor cells and enhance NK cytotoxicity to these adenocarcinoma cells.

## 2. Methods

**2.1. Cell Lines and Cultures.** Cell lines of A549 (human lung cancer cell) and MD-MBA-231 (human breast cancer cell) were obtained from the Cell Resource Center of Chinese Academy of Medical Sciences (Beijing, China). Peripheral blood mononuclear cell (PBMC) used in our experiments was gathered through separation of venous blood from healthy human donors. The blood was firstly diluted with D-Hanks at equal volume. Lymphocyte separation medium (TBD, China) was decanted into the mixture and four layers appeared after centrifugation of 20 min. The second layer was extracted by pipette and washed two times with D-Hanks to obtain PBMC. A549 and MD-MBA-231 cells were incubated in DMEM medium, which was supplemented with 100 u/mL penicillin, 100 mg/mL streptomycin, and 10% fetal calf serum (Gibco). All cells were cultured in 5% CO<sub>2</sub> at 37°C.

**2.2. Construction and Characterization of Amphipathic NP.** A previously identified MUC1 aptamer with the sequence of 5'-biotin-AACGCCAAATCCCTAAGAGTCG-GACTGCAACCTATGCTATCGTTGATGTCTGTCC-AAGCAACACAGACACACTACACACGCACA-3' was synthesized (Sangon Biotech, Shanghai, China). A previously selected CD16 aptamer with the sequence of 5'-biotin-CCATTGCGGGGTCTATACGTGAG GAAGAAGTGG-3' was also synthesized (Sangon Biotech, Shanghai, China). Five pmol MUC1 aptamer and 5 pmol CD16 aptamer were added to 20 μL of streptavidin-coated magnetic beads (Promega, Germany) and fully mixed for 15 min. The beads were washed thrice with 200 μL PBS to remove unbound oligonucleotides. To measure the size distribution of the amphipathic NP, 10 μL suspended NP was diluted into 1 mL PBS and analyzed with a dynamic light scattering (DLS) instrument (Zetasizer Nano ZS90, Malvern Instruments, Malvern, UK). Amphipathic NP samples were also evaluated by confocal microscopy (FV1000MPE, Olympus, USA).

**2.3. Flow Cytometric Analysis.** The binding of the aptamers to the target cells was evaluated by flow cytometry. FAM-labeled MUC1 and CD16 aptamers were synthesized (Sangon Biotech, Shanghai, China). Another aptamer that specifically binds with human epidermal growth factor receptor-2 (HER2) was also synthesized to serve as a control. FAM-labeled MUC1 aptamer was incubated with A549 and MD-MBA-231 cells for 30 min. FAM-labeled HER2 aptamer was incubated with A549 cells. FAM-labeled CD16 aptamer was incubated with PBMCs. All the above cells were washed with 200 μL PBS for three times and subjected to flow cytometry analysis (Accuri C6, USA).

To study whether the MUC1 and the CD16 aptamers were conjugated to the NP via the biotin-streptavidin reaction, DNA hybridization experiments were performed. MUC1 aptamer-modified NP, CD16 aptamer-modified NP, and MUC1-CD16 aptamers-modified NP were constructed by mixing streptavidin-coated NPs (Promega, Germany) with MUC1 aptamer, CD16 aptamer, and a mixture of both aptamers (at 1:1 molar ratio) for 15 min, respectively. Hybridizing DNA probes complementary to MUC1 or CD16 aptamers were incubated with the three types of particles for 30 min. After washing for three times with 200 μL PBS, the beads were subjected to flow cytometry analysis. All aptamers were biotinylated and all DNA probes were FAM-labeled.

For assessing the influence of aptamer-modification on the affinity of NP to target cells, competition blocking assays were conducted. Twenty thousand A549 cells were incubated with 40 pmol FAM-labeled MUC1 aptamer. Several items, including blank NP, MUC1 aptamer-modified NP, and unlabeled MUC1 aptamer, were separately added to the cells to compete with the FAM-labeled MUC1 aptamer. The mixtures were incubated for 30 min, washed for three times with 200 μL PBS, and subjected to flow cytometry analysis. Similar experiments were also conducted for CD16 and HER aptamers. Briefly, PBMC was incubated with FAM-labeled CD16 aptamer, while blank NP, CD16 aptamer-modified NP, and unlabeled CD16 aptamer were separately added to serve as competitive items. Moreover, HER2 aptamer-modified NP was also evaluated as a competitor of FAM-labeled MUC1 aptamer for binding with A549 cells.

**2.4. Phase-Contrast Microscopy.** The spatial relationship between live NK and A549 cells was studied with dark-field phase-contrast microscopy. Two groups of A549 cells were cultured in 6-well plate overnight and then cocultured with PBMC for 30 min. Amphipathic NP or blank NP were added to the two groups of cells. After washing with 1 mL PBS thrice, the cells were evaluated by phase-contrast microscopy.

**2.5. In Vitro Cytotoxicity Assays.** To evaluate whether the amphipathic NP would affect the NK reaction against A549 and MD-MBA-231 cells, NK cytotoxicity study was conducted. PBMC and A549 cells were cocultured in 96-well plates at effector : target ratio (*E* : *T*) of 100 : 1. Cellular mixtures were treated separately with various items, including the amphipathic NP (MUC1-NP-CD16), unmodified NP, a mixture of free CD16 and MUC1 aptamers, and the NP modified

by HER2 and CD16 aptamers (HER2-NP-CD16) for 10 hours at 37°C. The nonadherent lymphocytes were washed off with 200 μL PBS for three times. MTS assay was applied to evaluate the viability of the A549 cells, according to the standard protocol as outlined by the manufacturer (Promega, Germany). Similar experiments were also conducted on MD-MBA-231 cells. The PBMCs and MD-MBA-231 cells were cocultured at an *E:T* ratio of 100:1 for 10 h at 37°C with the amphipathic NP. After washing the cells with 200 μL PBS for three times, MTS assay was performed to assess the viability of the MD-MBA-231 cells.

### 3. Results

**3.1. Design of the Amphipathic NP.** The primary function of the amphipathic NP designed in this study was to bring together the NK and the MUC1-positive tumor cells. To implement this goal, we fabricated an NP that was modified with both the CD16 and the MUC1 aptamers. The aptamers were connected with streptavidin-covered nanoparticle via the biotin-streptavidin reaction. Because the amphipathic NP had both CD16 and MUC1 aptamers on its surface, it theoretically should combine with both the NK and the MUC1-positive cancer cells and bring them together. The overall design of the amphipathic NP was illustrated in Figure 1.

**3.2. Verification of the Binding Property of the Aptamers.** The capability of the aptamers to bind with their target cells was critical for the function of the amphipathic NP. Hence, we verified the binding properties of the aptamers against the target cells here in this study. FAM-labeled MUC1-aptamer was separately incubated with MUC1-positive A549 and MUC1-negative MD-MBA-231 cells, which were analyzed by flow cytometry. As shown in Figures 2(a) and 2(b), the MUC1 aptamer bound with the A549 but not the MD-MBA-231 cells, suggesting that the aptamer could recognize the MUC1-positive A549 cells. This study also required a control aptamer that did not bind with MUC1-positive cells, for which we employed an aptamer that was originally designed to recognize the HER2 protein. FAM-labeled HER2 aptamer was incubated with MUC1-positive A549 cells, which was analyzed by flow cytometry. The results showed that the HER2 aptamer did not bind with the A549 cells (Figure 2(c)), indicating that it might serve as a control aptamer for this study.

The capability of the CD16 aptamer for binding with immune cells was also evaluated in this study. Because PBMC was rich in CD16-positive immune cells, here we assessed the affinity of CD16 aptamer to PBMC, which was commonly used as the experiment model in NK-related studies [9]. FAM-labeled CD16 aptamer was incubated with PBMC, which was subsequently analyzed by flow cytometry. As illustrated in Figure 2(d), CD16 aptamer generated a strong binding to PBMC, suggesting that the aptamer could recognize the CD16-positive immune cells.

**3.3. Conjugation of Aptamers with Nanoparticles.** In order for the amphipathic NP to bring together the NK and the MUC1-positive cells, both the CD16 and the MUC1 aptamers must

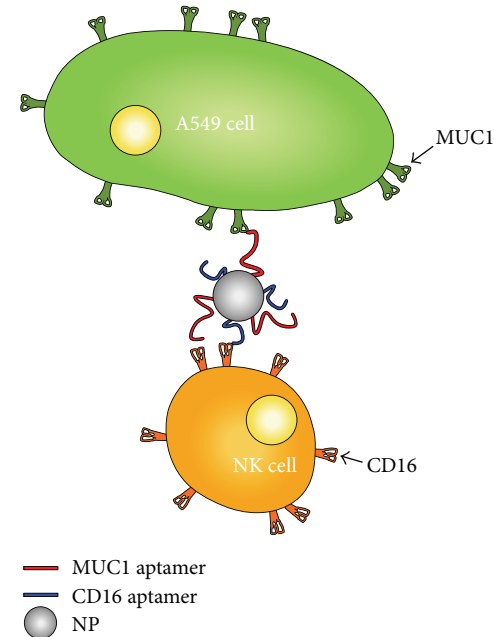


FIGURE 1: Illustration of the general design of the amphipathic NP. Biotinylated CD16 and MUC1 aptamers were connected with streptavidin-coated NP via biotin-streptavidin reaction. The proposed function of the amphipathic NP is to bring the NK to the vicinity of MUC1-positive cancer cell and induce an anticancer reaction.

be connected to the nanoparticle. To investigate whether the aptamers were indeed connected to the particle, DNA hybridization experiments were conducted. Two types of DNA probes (CD16 probe and MUC1 probe) were designed to complementarily recognize the CD16 and the MUC1 aptamers, respectively. The probes were separately incubated with NP, CD16 aptamer-modified NP (CD16-NP), MUC1 aptamer-modified NP (MUC1-NP), and the amphipathic NP (CD16-NP-MUC1), which were subjected to flow cytometry. As presented in Figure 3, CD16 aptamer-modified particles were positively stained by the CD16 probe, and MUC1-aptamer modified particles were stained by the MUC1 probe, while the amphipathic particles were positively stained by both probes. The results suggested that CD16 and MUC1 aptamers were indeed functionalized onto the surface of the amphipathic nanoparticles.

**3.4. Morphological Characterization of the Amphipathic NPs.** To investigate whether aptamer modification would affect the morphology and size of the iron NPs, blank NPs and aptamer-modified NPs were analyzed by confocal microscopy and dynamic light scattering (DLS) assay. As shown in Figure 4, confocal microscopy revealed that aptamer-modified NPs had similar morphology as unmodified NPs. DLS assay revealed that both the unmodified and the aptamer-modified NPs had single-peak size distribution. The average size of the unmodified NPs was 491 nm, whereas that of the aptamer-modified NPs was 574 nm, presumably because aptamer-modification increased the nanoparticles' average diameter as measured by DLS.

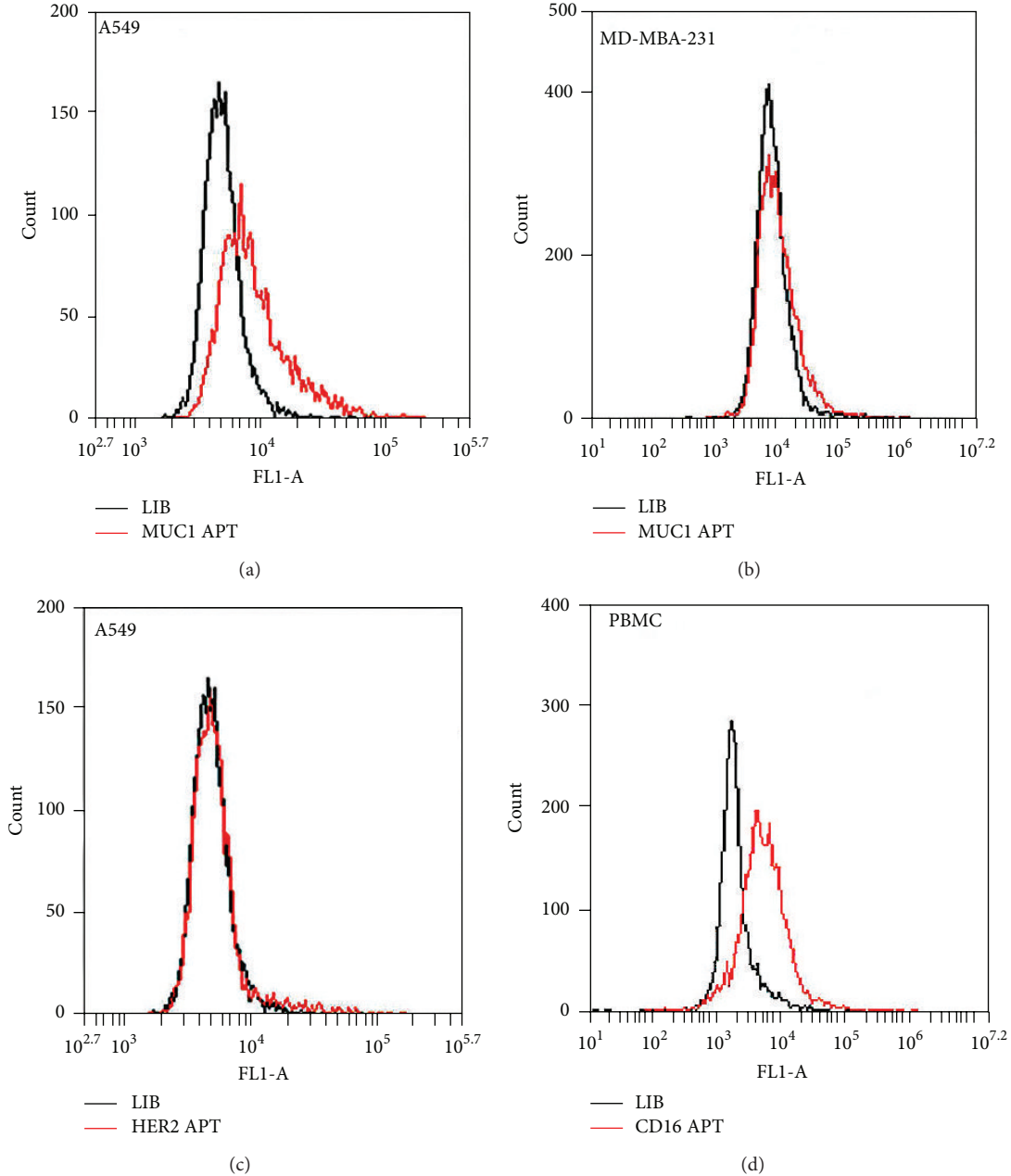


FIGURE 2: Evaluation of the binding affinity and specificity of the aptamers. FAM-labeled aptamers were incubated with cells and analyzed by flow cytometry (red lines). FAM-labeled random DNA (lib) was also incubated with the cells and served as the control (black lines). (a and b) Binding of MUC1 aptamer with the MUC1-positive A549 lung cancer cells and the MUC1-negative MDA-MB-231 cells, respectively. (c) Binding of the control HER2 aptamer with A549 cells. (d) Binding of the CD16 aptamer with PBMC.

**3.5. Binding of Aptamer-Modified NPs to Target Cells.** To evaluate whether MUC1 aptamer-modified NPs would attach to MUC1-positive cancer cells, these NPs were used to compete with free MUC1 aptamers for binding with A549 cells. Specifically, A549 cells were incubated with FAM-labeled MUC1 aptamers, in the presence or absence of the aptamer-modified NPs, and subjected to flow cytometry. The results showed that free aptamer's binding to target cells significantly decreased in the presence of aptamer-modified NPs (Figure 5(a)), indicating that these NPs also bound to A549 cells and competed

with free aptamer for the binding sites. Notably, unmodified NPs failed to generate a competition effect.

To investigate whether CD16 aptamer-modified NPs would attach to PBMCs, similar competition experiments were conducted. Specifically, PBMC was incubated with FAM-labeled CD16 aptamers, in the presence or absence of the NPs functionalized with CD16 aptamers, and analyzed by flow cytometry. As shown in Figure 5(b), the binding of CD16 aptamer to PBMC was dramatically reduced in the presence of the aptamer-modified NPs, suggesting that these NPs

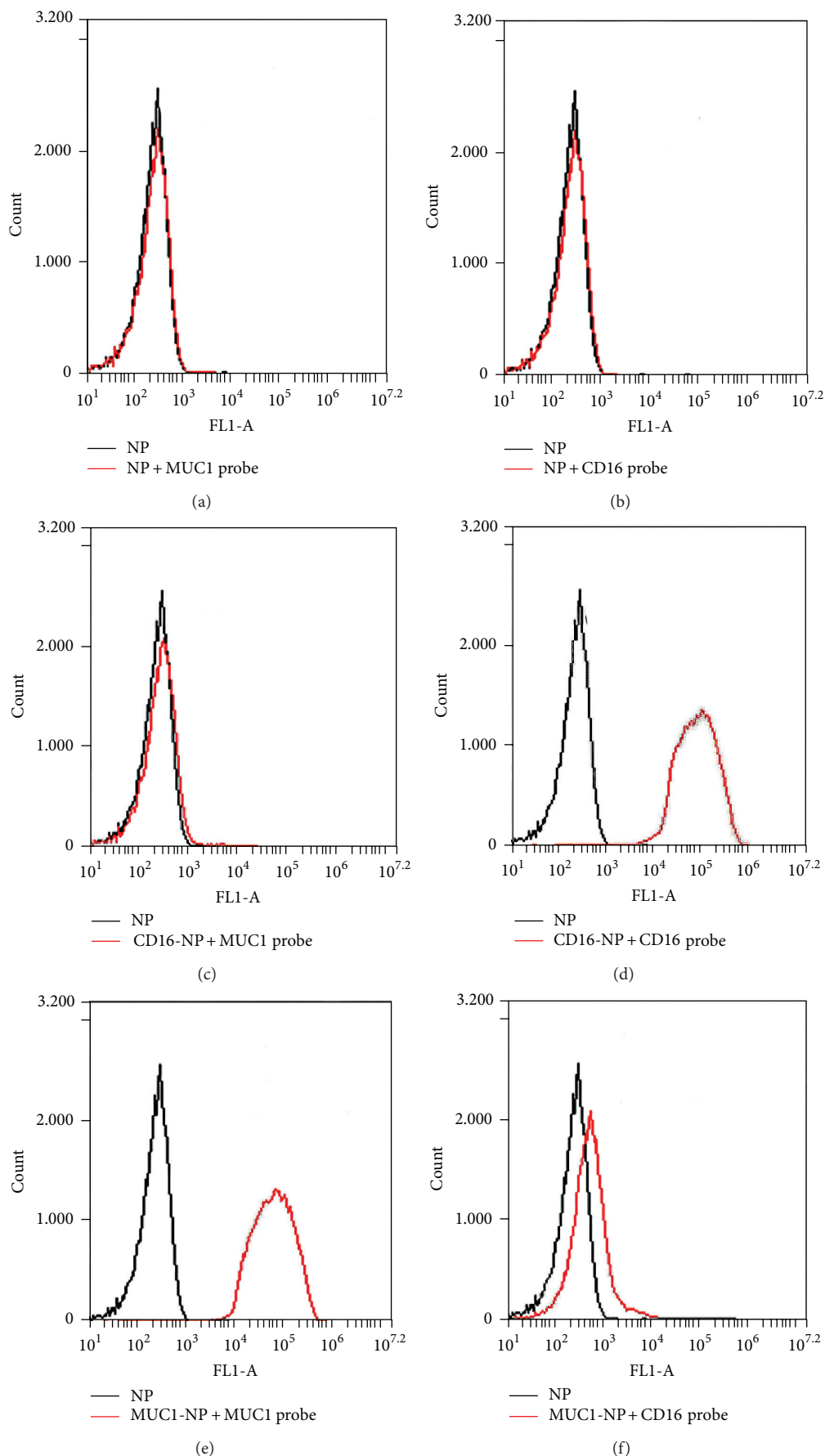


FIGURE 3: Continued.

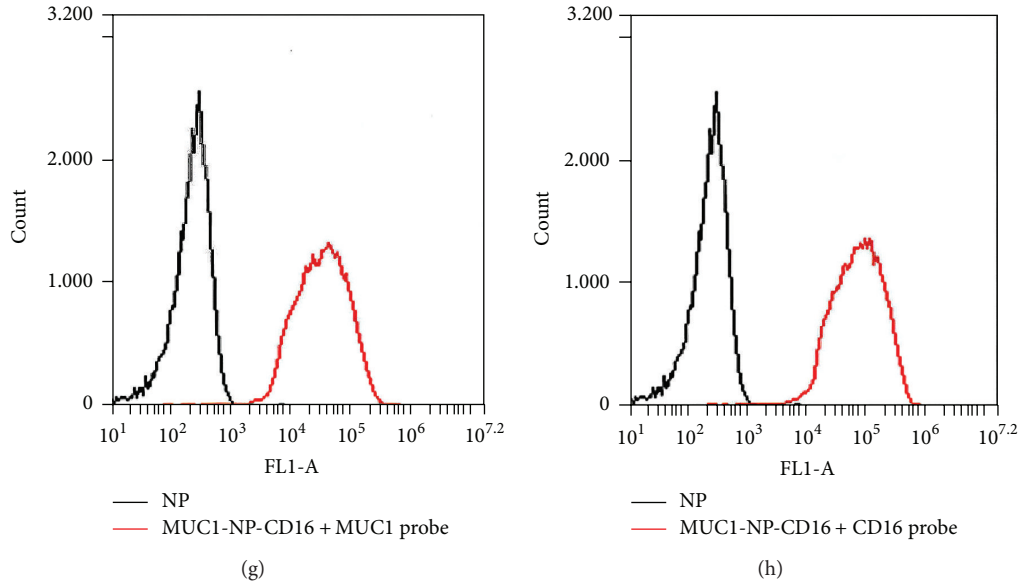


FIGURE 3: Evaluation of the conjugation of the aptamers with NP. MUC1 probe and CD16 probe were FAM-labeled DNA segments designed to hybridize with the MUC1 and the CD16 aptamers, respectively. Unmodified or aptamer-modified NPs were incubated with the probes and subjected to flow cytometry. Red lines represent signals from the beads treated with FAM-labeled DNA probe. Black lines represent the background signals from the untreated beads. (a) NP treated with MUC1 probe. (b) NP treated with CD16 probe. (c) CD16-NP treated with MUC1 probe. (d) CD16-NP treated with CD16 probe. (e) MUC1-NP treated with MUC1 probe. (f) MUC1-NP treated with CD16 probe. (g) CD16-NP-MUC1 treated with MUC1 probe. (h) CD16-NP-MUC1 treated with CD16 probe.

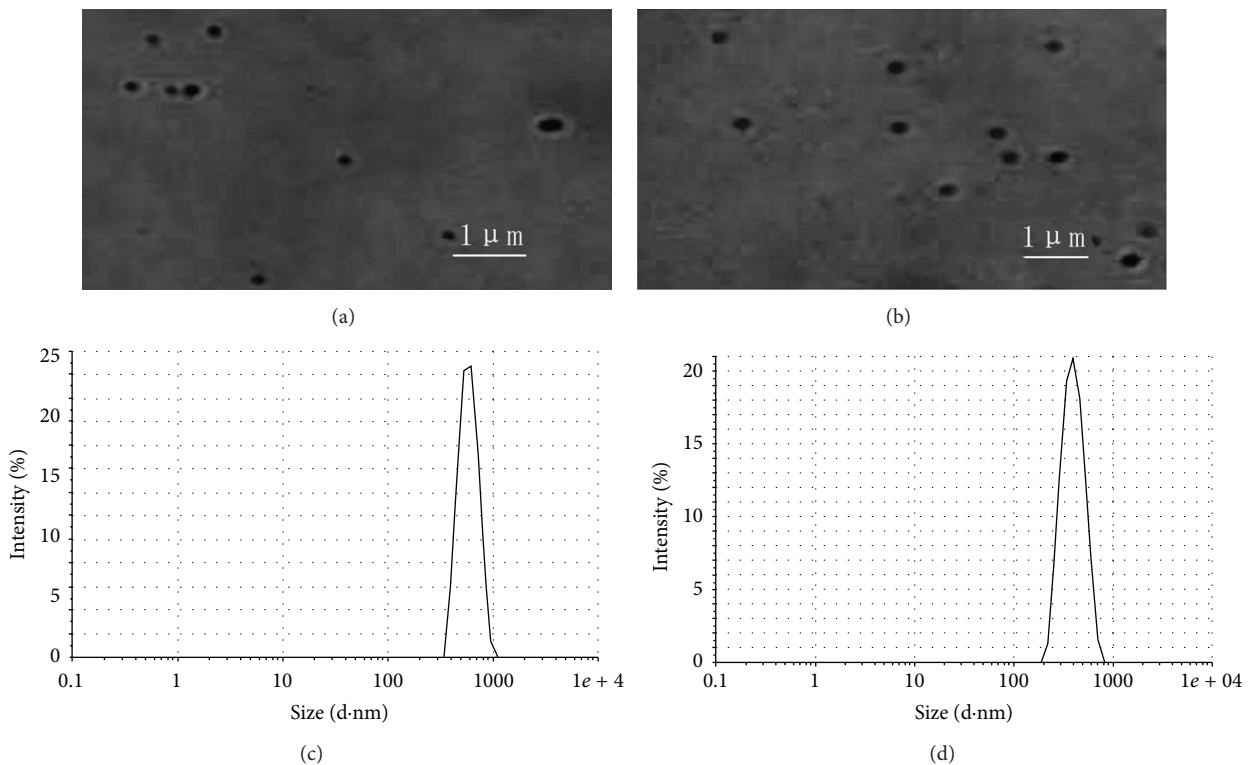


FIGURE 4: Morphological characterization of the amphipathic NP. (a and b) Confocal microscopic images showing the morphology of the amphipathic NP (a) and the unmodified NP (b). (c and d) DLS assay showing the size distributions of the amphipathic NP (c) and the unmodified NP (d).

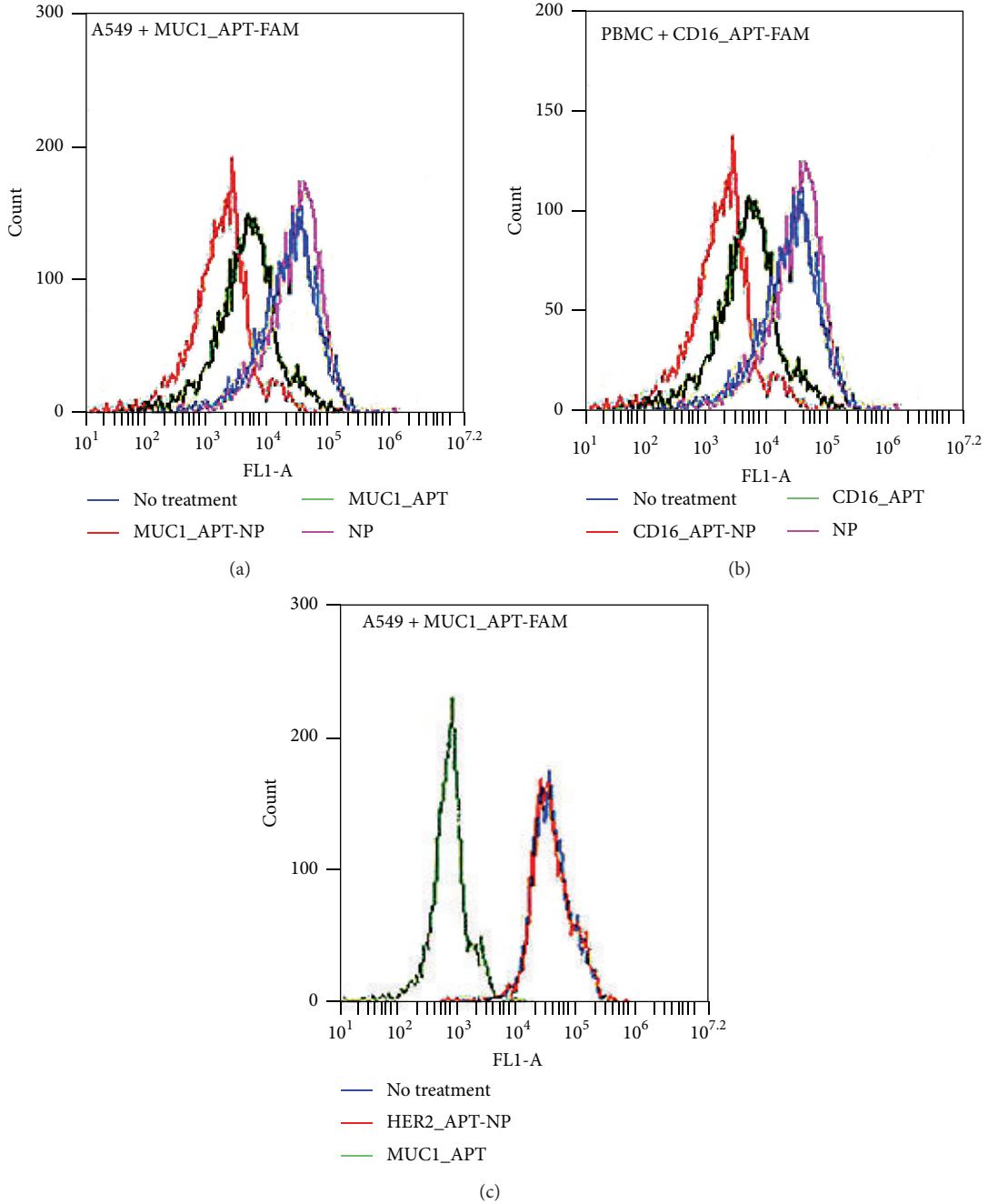


FIGURE 5: Evaluation of the binding of aptamer-modified NP to target cells by competition study. Cells were incubated with FAM-labeled aptamer. Free aptamer, aptamer-modified NP, or blank NP was added to compete for the binding sites on these cells, which were analyzed by flow cytometry. (a) A549 cells incubated with FAM-labeled MUC1 aptamer (blue line) and competed with MUC1-NP (red line), MUC1 aptamer (green line), or blank NP (purple line). (b) PBMC incubated with FAM-labeled CD16 aptamer (blue line) and competed with CD16-NP (red line), CD16 aptamer (green line), and blank NP (purple line). (c) A549 cells incubated with FAM-labeled MUC1 aptamer (blue line) and competed with HER2-NP (red line) and MUC1 aptamer (green line).

bound to PBMC and competed with CD16 aptamers for the binding sites. Unmodified NPs produced no competition effect.

The above results showed that NPs modified with MUC1 aptamer could attach to A549 cells. We wondered whether

NPs modified with any DNA (such as a HER2 aptamer) could also attach to MUC1-positive tumor cells. To address this issue, NPs modified with a HER2 aptamer were used to compete with FAM-labeled MUC1 aptamer for binding with A549 cells (Figure 5(c)). The results showed that HER2

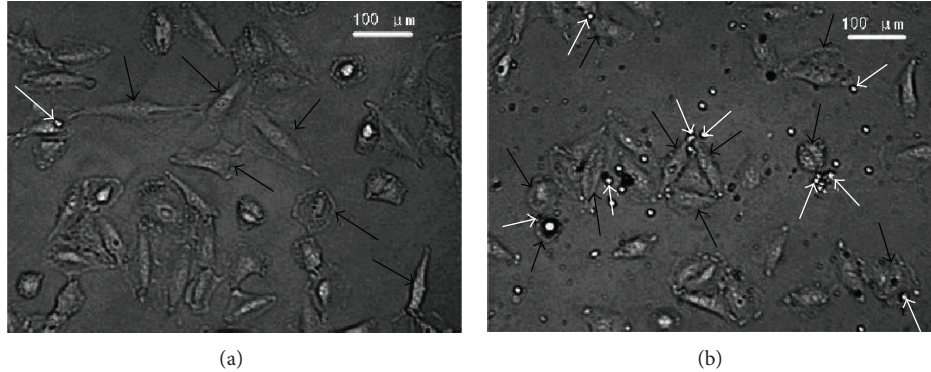


FIGURE 6: Effects of amphipathic NP on spatial relationship between NK and A549 cells. Live A549 cells were cocultured with fresh PBMC, treated with either the unmodified NP (a) or the amphipathic NP (b), washed, and evaluated by dark-field microscopy. Black arrows pointed to A549 cells, while white arrows pointed to PBMC.

aptamer-modified NPs did not reduce MUC1 aptamer's binding to A549 cells, indicating that these NPs did not bind with A549 cells.

**3.6. Amphipathic NPs Recruited NK to A549 Cells.** The above results showed that aptamer-modification facilitated the binding of NPs to A549 and NK cells, respectively. However, it was still unknown whether NP modified with both CD16 and MUC1 aptamers (the amphipathic NP) could attach to both kinds of cells and bring them close to each other. To answer this question, blank NP or the amphipathic NP was separately added to a mixture of NK and A549 cells. After unattached NK cells were removed by wash, the remaining cells were analyzed by dark-field microscopy. As shown in Figure 6, after treatment with blank NP, few NK cells remained in the culture dish, whereas after treatment with amphipathic NP, much more NK cells were still attached to A549 cells. The results indicated that the amphipathic NP could recruit more NK to the vicinity of A549 cells.

**3.7. NK Cytotoxicity to MUC1-Positive Cancer Cells Was Enhanced by Amphipathic NP.** The above study indicated that the amphipathic NP could recruit more NK to MUC1-positive A549 tumor cells. However, it was unknown whether the NK reaction to these tumor cells would also be enhanced. To address this issue, NK cytotoxicity studies were conducted. A549 cells were cocultured with PBMCs and treated separately with blank NP, amphipathic NP (MUC1-NP-CD16), a mixture of free CD16 and MUC1 aptamers (MUC1 APT + CD16 APT), and NP modified with CD16 and HER2 aptamers (HER2-NP-CD16). The NK cytotoxicity to A549 cells for each study group was analyzed by MTS assay. As illustrated in Figure 7(a), the amphipathic NP significantly enhanced NK cytotoxicity against A549 cancer cells, while blank NP, free aptamers, or HER2-CD16-NP failed to generate an obvious effect. The results indicated that pulling together NK and A549 cells by the amphipathic NP could activate NK to react against the MUC1-positive cancer cells.

To further investigate whether the NK antitumor reaction induced by the amphipathic NP was targeted towards

the MUC1-positive cancer cells, similar cytotoxicity study was also conducted with the MUC1-negative MD-MBA-231 cells. Specifically, MD-MBA-231 cells were cocultured with PBMC, treated with amphipathic NP, washed, and analyzed by MTS assay for viability. As shown in Figure 7(b), the amphipathic NP failed to enhance the NK reaction against these MUC1-negative cells. Taken together, the above data indicated that the NK cytotoxicity enhanced by the amphipathic NP was targeted towards the MUC1-positive cancer cells, but not the MUC1-negative control cells.

#### 4. Discussion

The primary purpose of this study was to construct an amphipathic nanoparticle that was modified with CD16 and MUC1 aptamers, which were implanted onto the particle via biotin-streptavidine reaction (Figure 1). The MUC1 aptamer was verified to bind with the MUC1-positive A549 lung cancer cells, but not the MUC1-negative MDA-MB-231 cells (Figures 2(a) and 2(b)). Similarly, the CD16 aptamer was also confirmed to bind with the PBMC that was rich in CD16-positive NK cells (Figure 2(d)). DNA hybridization experiments showed that the aptamers were indeed connected to the nanoparticles (Figure 3). The average size of the aptamer-modified NPs was about 574 nm, with a single-peak size distribution (Figure 4). Competition assays indicated that aptamer-modified NPs could bind with both the MUC1-positive cancer cells and CD16-positive immune cells (Figure 5). Moreover, a significantly increased number of NKs were observed to attach to the MUC1-positive cancer cells in the presence of amphipathic NPs (Figure 6), suggesting that the nanostructure could pull the NK close to the target cancer cells. In addition, this nanoparticle significantly enhanced the NK's antitumor immune cytotoxicity to the MUC1-positive A549 cancer cells (Figure 7(a)), but not that to the MUC1-negative MD-MBA-231 control cells (Figure 7(b)), indicating that a targeted NK reaction against the MUC1-positive tumor cells was promoted by the amphipathic NPs.

MUC1 is an important molecular target for cancer treatment. It is underexpressed in normal tissue [13] but overexpressed in majority of adenocarcinomas, including lung,

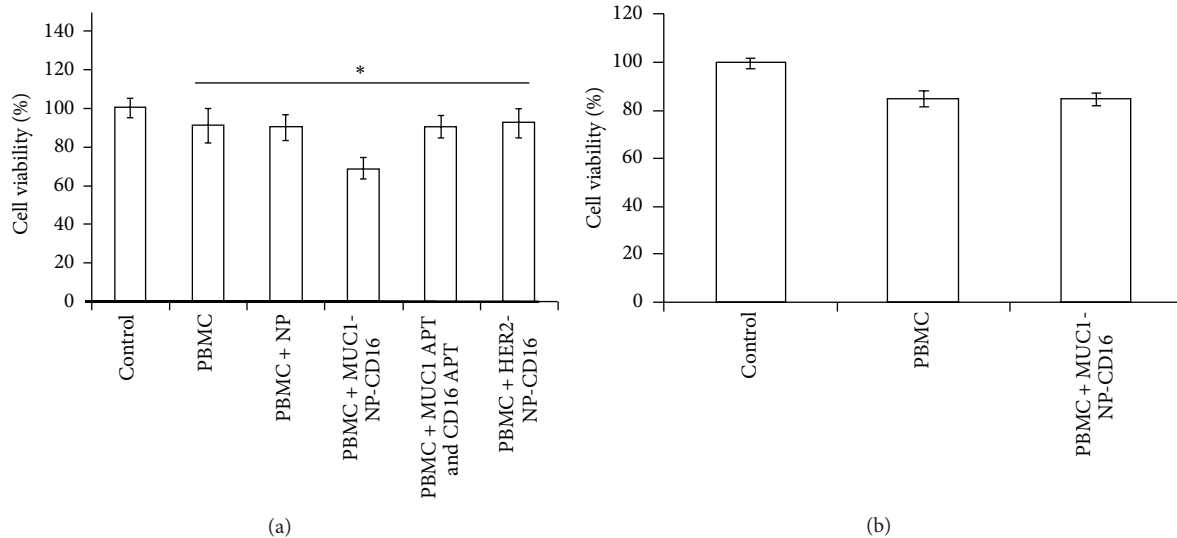


FIGURE 7: Modulation of the NK cytotoxicity to cancer cells by amphipathic NP. The cancer cells were cocultured with PBMC in the presence of various treatments and analyzed for viability. (a) MUC1-positive A549 cells treated with blank NP, the amphipathic NP (MUC1-NP-CD16), a mixture of free CD16 and MUC1 aptamers, and NP modified with HER2 and CD16 aptamers (HER2-NP-CD16). (b) MUC1-negative MD-MBA-231 cells treated with the amphipathic NP. The NK cytotoxicity was evaluated by a standard MTS assay per manufacturer's protocol (mean  $\pm$  SD,  $n = 8$ ). The star indicates a statistically significant difference ( $p < 0.01$ ).

liver, breast [14], ovarian, colon, pancreatic, prostate cancers, and multiple myeloma [15–17]. The overexpression of MUC1 mucin may be associated with cancer progression and metastasis of many malignancies [18–20]. Because MUC1 is overexpressed in many types of adenocarcinoma and under-expressed in normal cells, it is considered as an ideal molecular target for cancer therapy. As a result, several attempts for development of MUC1-targeted cancer therapy have been reported, including targeted drug delivery to MUC1-positive tumor cells with aptamer-guided vehicles [21], tumor vaccine based on MUC1 protein for inducing anticancer T cell response [5], and MUC1-targeted photodynamic cancer therapy with photosensitizer carried by MUC1 aptamers [22]. So far, however, there is no report in the literature on directing NK cells to MUC1-positive tumor cells for enhancement of the NK reaction against these cancer cells. In this study, we built an aptamer-based amphipathic nanoparticle that could recruit NK cells to MUC1-positive cancer cells. We found that the nanoparticle could induce a targeted NK cytotoxicity to MUC1-positive tumor cells. The results suggested that, in addition to anticancer drugs, T lymphocytes, or photodynamic energy, NK cells might also be recruited to develop a novel targeted therapy against MUC1-positive tumors.

The mechanism by which the amphipathic NP promotes the NK reaction to MUC1-positive cancer cells is unclear at present. We suspect that the enhanced NK cytotoxicity to tumor cells may be related to increased interaction between the two types of cells. Our data indicate that the amphipathic NP can recruit NK to the vicinity of MUC1-positive tumor cells (Figure 6). This will probably increase the chance of interaction between the NK and the target cancer cells, and, through some unknown molecular mechanisms, activate the NK to initiate an anticancer reaction. Similarly, a previously

study also reported that recruiting NK cells to the neighborhood of HGF-R positive tumor cells could enhance the NK reaction against these cancer cells [9]. However, the detailed molecular mechanisms of the NK activation for increased anticancer response remain to be unveiled. In any case, this study found that pulling together NK and MUC1-positive tumor cells could enhance the NK reaction against the A549 adenocarcinoma cells. This finding may lead to the development of novel targeted therapy against MUC1-positive tumors through recruitment of NK cells for anticancer reaction. Nevertheless, it should be noted that the current study is just an early exploration of recruiting NK to fight against MUC1-expressing cancer cells. In order to further develop and implement the strategy, extensive future research is still warranted, including studies on development of nuclease-resistant aptamers, selection of optimal nanoparticles, exploration of proper methods to connect the aptamers with the nanosstructure, and evaluation of *in vivo* therapeutic efficacy with animal studies.

In summary, a novel amphipathic nanoparticle was constructed by implanting CD16 and MUC1 aptamers onto its surface. This nanoparticle pulled NK (or other CD16-positive immune cells) and MUC1-positive cancer cells together *in vitro* and significantly enhanced the NK cytotoxicity to MUC1-positive cancer cells. The results suggest that NK cells may be mobilized to target against MUC1-positive tumor cells.

## Conflict of Interests

The authors declare that there is no conflict of interests regarding the publication of this paper.

## Acknowledgments

The authors acknowledge the funding support from the Chinese Ministry of Science and Technology (2011CB933504) and the 111 Project from the Chinese Ministry of Education.

## References

- [1] A. Vermes, H.-J. Guchelaar, and J. Dankert, "Flucytosine: a review of its pharmacology, clinical indications, pharmacokinetics, toxicity and drug interactions," *Journal of Antimicrobial Chemotherapy*, vol. 46, no. 2, pp. 171–179, 2000.
- [2] T. Reuther, T. Schuster, U. Mende, and A. C. Kübler, "Osteoradionecrosis of the jaws as a side effect of radiotherapy of head and neck tumour patients—a report of a thirty year retrospective review," *International Journal of Oral and Maxillofacial Surgery*, vol. 32, no. 3, pp. 289–295, 2003.
- [3] S. A. Rosenberg, "Progress in human tumour immunology and immunotherapy," *Nature*, vol. 411, no. 6835, pp. 380–384, 2001.
- [4] K. Tarte and B. Klein, "Dendritic cell-based vaccine: a promising approach for cancer immunotherapy," *Leukemia*, vol. 13, no. 5, pp. 653–663, 1999.
- [5] R. Kovjazin, I. Volovitz, Y. Kundel et al., "ImMucin: a novel therapeutic vaccine with promiscuous MHC binding for the treatment of MUC1-expressing tumors," *Vaccine*, vol. 29, no. 29–30, pp. 4676–4686, 2011.
- [6] D. Berd, T. Sato, H. C. Maguire Jr., J. Kairys, and M. J. Mastangelo, "Immunopharmacologic analysis of an autologous, hapten-modified human melanoma vaccine," *Journal of Clinical Oncology*, vol. 22, no. 3, pp. 403–415, 2004.
- [7] J. S. Yu, G. T. Liu, H. Ying, W. H. Yong, K. L. Black, and C. J. Wheeler, "Vaccination with tumor lysate-pulsed dendritic cells elicits antigen-specific, cytotoxic T-cells in patients with malignant glioma," *Cancer Research*, vol. 64, no. 14, pp. 4973–4979, 2004.
- [8] C. Mesa and L. E. Fernández, "Challenges facing adjuvants for cancer immunotherapy," *Immunology and Cell Biology*, vol. 82, no. 6, pp. 644–650, 2004.
- [9] A. Boltz, B. Piater, L. Toleikis, R. Guenther, H. Kolmar, and B. Hock, "Bi-specific aptamers mediating tumor cell lysis," *The Journal of Biological Chemistry*, vol. 286, no. 24, pp. 21896–21905, 2011.
- [10] Y. Hu, J. Duan, Q. Zhan, F. Wang, X. Lu, and X.-D. Yang, "Novel MUC1 aptamer selectively delivers cytotoxic agent to cancer cells in vitro," *PLoS ONE*, vol. 7, no. 2, Article ID e31970, 2012.
- [11] J. Taylor-Papadimitriou, J. Burchell, D. W. Miles, and M. Dalziel, "MUC1 and cancer," *Biochimica et Biophysica Acta—Molecular Basis of Disease*, vol. 1455, no. 2–3, pp. 301–313, 1999.
- [12] P. Zhang, N. X. Zhao, Z. H. Zeng et al., "Using an RNA aptamer probe for flow cytometry detection of CD30-expressing lymphoma cells," *Laboratory Investigation*, vol. 89, no. 12, pp. 1423–1432, 2009.
- [13] P. Chaturvedi, A. P. Singh, and S. K. Batra, "Structure, evolution, and biology of the MUC4 mucin," *The FASEB Journal*, vol. 22, no. 4, pp. 966–981, 2008.
- [14] E. A. Rakha, R. W. G. Boyce, D. A. El-Rehim et al., "Expression of mucins (MUC1, MUC2, MUC3, MUC4, MUC5AC and MUC6) and their prognostic significance in human breast cancer," *Modern Pathology*, vol. 18, no. 10, pp. 1295–1304, 2005.
- [15] K. Ohuchida, K. Mizumoto, D. Yamada et al., "Quantitative analysis of MUC1 and MUC5AC mRNA in pancreatic juice for preoperative diagnosis of pancreatic cancer," *International Journal of Cancer*, vol. 118, no. 2, pp. 405–411, 2006.
- [16] S. C. Chauhan, N. Vinayek, D. M. Maher et al., "Combined staining of TAG-72, MUC1, and CA125 improves labeling sensitivity in ovarian cancer: antigens for multi-targeted antibody-guided therapy," *Journal of Histochemistry & Cytochemistry*, vol. 55, no. 8, pp. 867–875, 2007.
- [17] J. C. O'Connor, J. Julian, S. D. Lim, and D. D. Carson, "MUC1 expression in human prostate cancer cell lines and primary tumors," *Prostate Cancer and Prostatic Diseases*, vol. 8, no. 1, pp. 36–44, 2005.
- [18] Y. S. Kim, J. Gum Jr., and I. Brockhausen, "Mucin glycoproteins in neoplasia," *Glycoconjugate Journal*, vol. 13, no. 5, pp. 693–707, 1996.
- [19] M. Sachdeva and Y.-Y. Mo, "MicroRNA-145 suppresses cell invasion and metastasis by directly targeting mucin 1," *Cancer Research*, vol. 70, no. 1, pp. 378–387, 2010.
- [20] S. Satoh, Y. Hinoda, T. Hayashi, M. D. Burdick, K. Imai, and M. A. Hollingsworth, "Enhancement of metastatic properties of pancreatic cancer cells by MUC1 gene encoding an anti-adhesion molecule," *International Journal of Cancer*, vol. 88, no. 4, pp. 507–518, 2000.
- [21] C. Yu, Y. Hu, J. Duan et al., "Novel aptamer-nanoparticle bioconjugates enhances delivery of anticancer drug to MUC1-positive cancer cells in vitro," *PLoS ONE*, vol. 6, no. 9, Article ID e24077, 2011.
- [22] C. S. M. Ferreira, M. C. Cheung, S. Missailidis, S. Bisland, and J. Gariépy, "Phototoxic aptamers selectively enter and kill epithelial cancer cells," *Nucleic Acids Research*, vol. 37, no. 3, pp. 866–876, 2009.